STRUCTURE AND ATOMIC DYNAMICS IN CONDENSED MATTER UNDER PRESSURE AND LI-ION BATTERY MATERIALS

A Thesis Submitted to the College of

Graduate Studies and Research

In Partial Fulfillment of the Requirements

For the Degree of Doctor of Philosophy

In the Department of Physics and Engineering Physics

University of Saskatchewan

Saskatoon

By

Jianjun Yang

PERMISSION TO USE

In presenting this thesis in partial fulfilment of the requirements for a Postgraduate degree from the University of Saskatchewan, I agree that the Libraries of this University may make it freely available for inspection. I further agree that permission for copying of this thesis in any manner, in whole or in part, for scholarly purposes may be granted by the professor or professors who supervised my thesis work or, in their absence, by the Head of the Department or the Dean of the College in which my thesis work was done. It is understood that any copying or publication or use of this thesis or parts thereof for financial gain shall not be allowed without my written permission. It is also understood that due recognition shall be given to me and to the University of Saskatchewan in any scholarly use which may be made of any material in my thesis.

Requests for permission to copy or to make other use of material in this thesis in whole or part should be addressed to:

Head of the Department of Physics and Engineering Physics
116 Science Place
University of Saskatchewan
Saskatoon, Saskatchewan
Canada
S7N 5E2

ABSTRACT

The main goal of this research was to apply first-principles electronic structure calculations to investigate atomic motions in several condensed materials. This thesis consists of five separate but related topics that are classified into two main categories: structure of materials under pressure and Li ion dynamics in lithium battery materials.

The atomic structure of liquid gallium was investigated in order to resolve a controversy about an anomalous structural feature observed in the x-ray and neutron scattering patterns. We explored the pressure effect when modifying the liquid structure close to the solid-liquid melting line. The atomic trajectories obtained from first-principles molecular dynamics (FPMD) calculations were examined. The results clarified the local structure of liquid gallium and explained the origin of a peculiar feature observed in the measured static structure factor. We also studied the structure of a recently discovered phase-IV of solid hydrogen over a broad pressure range near room temperature. The results revealed novel structural dynamics of hydrogen under extreme pressure. Unprecedented large amplitude fluxional atomic dynamics were observed. The results helped to elucidate the complex vibrational spectra of this highly-compressed solid.

The atomic dynamics of Li ions in cathode, anode, and electrolyte materials - the three main components of a lithium ion battery - were also studied. On $LiFePO_4$, a promising cathode material, we found that in addition to the commonly accepted one-dimensional diffusion along the Li channels in the crystal structure, a second but less obvious multi-step Li migration through the formation of Li-Fe antisites was identified. This discovery confirms the two-dimensional Li diffusion model reported in several Li conductivity measurements and illustrates the importance of the distribution of intrinsic defects in the enhancement of Li transport ability. The possibility of using type-II clathrate Si_{136} as an anode material was investigated. It was found that lithiated Si-clathrates are intrinsic metals and their crystal structures are very stable. Calculations revealed the charge and discharge voltages are very low and almost independent of the Li concentrations, an ideal property for an anode material. Significantly, migration pathways for Li ions diffusing through the cavities of the clathrate structures were found to be rather complex. Finally, the feasibility of a family of Li_3PS_4 crystalline and nanoporous cluster phases were studied for application as solid electrolytes. It was found that the ionic conductivity in the nanocluster is much higher than in crystalline phases. It is anticipated that the knowledge gained in the study of battery materials will assist in future design of new materials with improved battery charge and discharge performance.

ACKNOWLEDGMENTS

There are many wonderful colleagues and friends surrounded me during my PhD study at the University of Saskatchewan. I would have never been able to complete my thesis without their contributions and support and I would like to acknowledge their importance to my thesis journey.

Firstly, I would like to express my deepest gratitude to my supervisor, Professor John Tse, who offered me the opportunity to pursue the PhD study with him four years ago and has provided help at all stages of this thesis. He deserves thanks for the continuous support in many aspects, whether it was providing excellent academic guidance, exposure to wide scientific interests, financial contributions, great patience, friendly care, or thoughtful career advice. His vision and ability to grasp the essence of physics in a complicated problem; his deep and vast knowledge of condensed matter physics; and his enthusiasm for science have greatly influenced me and my future professional development.

I appreciate all of my thesis committee members: Professor Andrei Smolyakov, Professor Masoud Ghezelbash, and Professor Burgess Ian for their time, encouragement and insightful comments.

I would like to thank all fellow students and postdocs from Professor Tse's group for the collaborations, fruitful discussions and willingness to share their skills and interests. I enjoyed the collaboration with Hui Wang on the hydrogen project. Although I spent a shorter amount of time with Hanyu Liu, we had a lot of fruitful and interesting scientific discussions. Xue Yong generously shared her skills with much scientific software. The names of all other group members also deserve a mention: Niloofar Zarifi, Jianbao Zhao, Garimella Subrahmanyam, Jun

Yang, Jianjun Yang (male), and Min Wu. I enjoyed and benefited a lot from many scientific and non-scientific conversations with them.

A special thanks to Professor Gapsoo Chang for his support and guidance throughout my teaching experience. Additionally, I wish to thank Professor Yansun Yao for his help and instructive suggestions on potential career paths. My appreciation goes to Paul Bazylewski for his willingness to correct my written English and share his ideas over the lab demonstrations. I would also like to thank the secretaries of my department, Ms. Debbie Parker and Marj Granrude, for taking care of administrative matters.

I owe big thanks to my husband Donghui Wu for his deep love and unhesitating support of the time commitment required for this thesis work. I am also indebted to my two sons, Jackson and Alan, for their love and patience. This thesis work demanded a lot of my time that they deserved to have and enjoy. My sincere thanks also go to all my family members from China for their eternal love and care.

Finally, I am very grateful to the AUTO21 for financial support on the study of Li-ion batteries.

TABLE OF CONTENTS

LIST OF TABLES

Table page

LIST OF FIGURES

LIST OF ABBREVIATIONS

1D	One-dimensional
2D	Two-dimensional
3D	Three-dimensional
BZ	Brillouin zone
CN	Coordination number
cNEB	Climbing nudged elastic band
D	Diffusion coefficient
DFT	Density functional theories
DOS	Electronic density of states
EV	All-electric vehicles
EXAFS	Extended X-Ray Absorption Fine Structure
fcc	Face-centered cubic
FPMD	First-principles molecular dynamics
GGA	Generalized Gradient Approximation
hcp	Hexagonal close pack
HEV	Hybrid electric vehicles
HOMO	The highest occupied molecular orbital
INS	Inelastic neutron scattering
IR	Infrared
IXS	Inelastic X-ray scattering
KS	Kohn-Sham
LDA	Local Density Approximation
LIBs	Li-ion batteries
LSDA	Local spin density approximation
LUMO	The lowest unoccupied molecular orbital
MD	Molecular dynamics
MEP	Minimum energy path
MSD	Mean square displacement
NEB	Nudged elastic band
NPT	Constant-pressure and constant-temperature
NVT	Constant-volume and constant-temperature
PAW	Projector Augmented Waves
PBC	Periodic boundary conditions
PBE	Perdew-Burke-Ernzerhof
PW	Plane-wave
PW91	Perdew-Wang 91

Quantum-ESPRESSO	Open Source Package for Research in Electronic Structure, Simulation, and Optimization
RDF	Radial distribution function
S(q)	Static structure factor
SEI	Solid-electrolyte-interface
VACF	Velocity autocorrelation function
VASP	Vienna Ab-initio Simulation Package
VDOS	Vibrational density of states
XAS	X-ray absorption
ZPE	Zero-point energy

CHAPTER 1

INTRODUCTION

Atomic dynamics always plays an important role in the properties of condensed systems. Atomic diffusion can occur in both ordered and disordered systems [1], with the most obvious example being a molten liquid lacking long-range order. It is generally assumed that local structures in liquids tend to show short-range ordering within a few tenths of a nanometer, resembling the atomic arrangements in their solid counterparts [2]. While it is intuitively obvious that the structure of a molten system is disordered and thus exhibits atomic motions, atomic diffusion in solids that are ordered or partially-disordered is also of practical interest. Furthermore, crystals containing molecules or complex ions have additional complexity in comparison with a usual liquid because they possess orientational as well as translational degrees of freedom. They can therefore exhibit a variety of orientational and translational disorders. A large number of crystals composed of diatomic, high-symmetry (*i.e.*, tetrahedral), and more complex organic molecules [3, 4] are known to exhibit a rotor phase. One example of a solid with rotational disorder is the simplest diatomic system formed by isotopes of hydrogen [1, 5]; a class of solids exhibiting significant atomic motion is represented by superionic materials. These solids exhibit characteristics of both a solid and a liquid simultaneously. Above a critical temperature, one atomic species in the material may exhibit liquid-like ionic conductivities and dynamic disorder within the rigid crystalline structure of the others (partial lattice melting). The abrupt change in ionic mobility during this phase transition has be explored for practical applications such as solid-state electrolytes and resistance switching devices [6, 7].

In spite of extensive interest and repeated applications of these disordered condensed systems, fundamental questions concerning the microscopic origin and mechanisms of atomic dynamical behaviour associated with the structural properties for a number of systems have not yet been fully clarified. Atomistic numerical simulations with well-established first-principles methods have proven to be indispensable complements to experimental measurements. By analyzing the trajectory, mechanisms of the transport process can be elucidated at the atomic level. With the rapid increase in computational power and development of advanced electronic structure algorithms of high numerical accuracy, the variety and complexity of materials susceptible to modelling has increased dramatically over recent years. The objective of this thesis is to apply first-principles computational simulations to explore the structural and dynamical properties of selected condensed systems at both ambient and high-pressure conditions. The topics studied can be classified into two categories: atomic dynamics in condensed matter under pressure, and Li ion transports in the cathode, anode, and solid electrolyte materials of rechargeable Li-ion batteries (LIBs) at ambient pressure.

1.1 Condensed matter under pressure

Significant questions in geophysics, planetary physics, and applied materials science address the concern with the physical and electronic properties of solids under high pressure. At high pressure, ambient structures of most condensed systems can be modified dramatically. As a result, novel electronic properties and atomic dynamics may emerge in the new phases. In this thesis, the structure and dynamics of two condensed systems, liquid gallium (*l*-Ga) and solid hydrogen, will be studied.

1.1.1 Structure of liquid gallium

Inelastic neutron scattering (INS) and X-ray scattering (IXS) are the two most common techniques for studying structure and atomic dynamics in condensed matter [8]. Generally, for simple liquid metal the measured static structure factor, $S(q)$, shows a symmetrical first sharp peak. In comparison, liquids from covalently bonded solids, such as those of group IV elements (Si, Ge, *etc*.), often exhibit a distinct shoulder at the high q ($q = 4\pi/\lambda\sin\theta$, where λ is the wavelength and θ is the scattering angle) side of the first peak in the $S(q)$ [9]. Furthermore, high pressure measurements have revealed that the contraction of liquid alkali metals is almost uniform [8], whereas those of group IV elemental liquids are anisotropic [9].

Recently, INS and IXS experiments on *l*-Ga over a broad temperature range have been performed [10-14]. Similar to group-IV elemental liquid like Si or Ge, researchers found that the structure factor $S(q)$ in liquid Ga also displays a distinct shoulder at the high q side of the first peak, which is indicative of a covalent behaviour. In contrast, the coordination number was found to range from 10 to 12 when the *l*-Ga is close to the melting point, showing a property similar to typical densely-packed simple liquid metals instead. The unique feature in *l*-Ga has motivated many investigations to explain the origin of the characteristic shoulder in the first peak of $S(q)$; of a particular note is that the pressure effect on the liquid structure have been conducted by a series of experiments using INS, IXS and extended x-ray absorption (XAS) [15, 16]. For this purpose, first-principles molecular dynamics (FPMD) simulations were performed on *l*-Ga at a number of temperature and pressure (P,T) points. From the obtained trajectories, the structure factors and the XAS spectra were computed and compared with available experimental results

[15, 16]. The validity of previously proposed local structures was carefully examined with the help of vibrational density of states. Finally, the electronic structure of the *l*-Ga was compared with that of the underlying solid phases existing in the similar *P*-*T* range.

1.1.2 Atomic dynamics in phase-IV solid hydrogen

Being the lightest and the most abundant element in the universe, hydrogen is a fascinating substance and is of special interest to the high-pressure and astrophysics scientific communities [5, 17, 18]. Phase-I solid H_2 is formed by freezing the liquid at ambient pressure. The phase has a hexagonal close pack (*hcp*) lattice, but the hydrogen molecules rotate randomly about their center of mass [19]. Upon compression, solid hydrogen undergoes a series of phase transitions where the orientational and translational orders are modified. At low temperatures, it transforms into a quantum broken symmetry phase (phase-II) at pressures of 10 (50) GPa for H_2 (D_2) and phase-III at 150 (165) GPa [20]. However, because of the limited information, such molecular orientations in phases II and III have not been fully determined. Partially-orientational ordering was suggested through the experimental observation that the center of mass of the H_2 molecule still remains close to the *hcp* lattice sites of phase-I up to 183 GPa [21]. The transformation into phase-III is evidenced with distinctive enhancement in the infrared absorptivity [22]. Recent theoretical calculations have predicted a fully ordered structure with the space group symmetry of $C2/c$ to be the best candidate [23]. More recently, a new phase was discovered when phase-III was compressed to nearly 220 GPa at room temperature [24]. Experimental results on this newly discovered phase (phase-IV) [24, 25] are still sparse, but a dramatic change of the Raman spectra indicates a substantial change in the crystal structure.

Based on the Raman results, this new phase was suggested to have a layered structure with alternating molecular Br_2-like and atomic graphene-like planes [25].

Perhaps the most investigated topic regarding solid hydrogen is the possible insulator-to-metal transition. Early theoretical predictions suggested that hydrogen would become atomic and metallic at high pressure [26], and the atomic metallic phase (>500 GPa) was predicted to be a high temperature superconductor [27]. So far, the metallic phase has not been detected experimentally although the transition is anticipated. Theoretical studies generally agree that the transition pressure to atomic and metallic phase exists above 300 GPa and has an orthorhombic *Cmca*-4 space group [5, 17, 28]. Therefore, the orientational dynamics of the H_2 molecules must experience a series of continual changes with compression starting from the low pressure molecular phase-I to the atomic phase at high pressure. Since there are difficulties in determining the crystal structure of hydrogen at high pressure, first-principles calculations have been an invaluable tool to gain insight into this yet unidentified phase. In the present study, the FPMD simulation method is shown to be a very powerful tool in examining the evolution of orientational dynamics as well as the structural transformations of dense solid hydrogen, particularly of phase-IV.

1.2 Lithium-ion battery materials

Rechargeable lithium-ion batteries (LIBs) are one of the key components in the portable entertainment, computing and telecommunication equipment in today’s information-rich and mobile society. Despite impressive growth in worldwide sales of batteries, battery technology advancement has generally lagged behind other technology sectors such as semiconductors.

While it is true that energy storage capacity may not keep pace with the rate of progress in the computer industry, recent advances in lithium batteries, particularly at the material level, give hope that the performance will soon be dramatically improved. If this expectation materializes, it will signify a tremendous shift in the battery industry, offering promise for many applications that require better batteries; for example, the expansion of hybrid electric vehicles (HEV) into plug-in HEV and all-electric vehicles (EV) may benefit from such improvements.

Despite the advantages of their high energy density and design flexibility, LIBs still have several shortcomings. For example, some component materials cost too much and for some systems they may be unsafe or unreliable, and the energy density is not sufficiently high to be useful in large scale applications. Therefore, a breakthrough in the design technology of the LIBs is urgently needed to meet rapidly increasing demands.

The performance of a battery is determined by the intrinsic properties of its component materials. A rechargeable LIB consists of three main components: a positive electrode (cathode), a negative electrode (anode), and an electrolyte (Li ionic conduction medium). On discharge, electrons flow from the anode through an external circuit to the cathode and Li ions migrate from the anode to the cathode through the electrolyte to retain charge neutrality. The reverse happens in the charging process. The anode is the reductant and the cathode is the oxidant. During discharge, the chemical reaction is used to produce electricity. Figure 1. 1 shows a schematic energy level diagram of the three principal components of a typical battery [29].

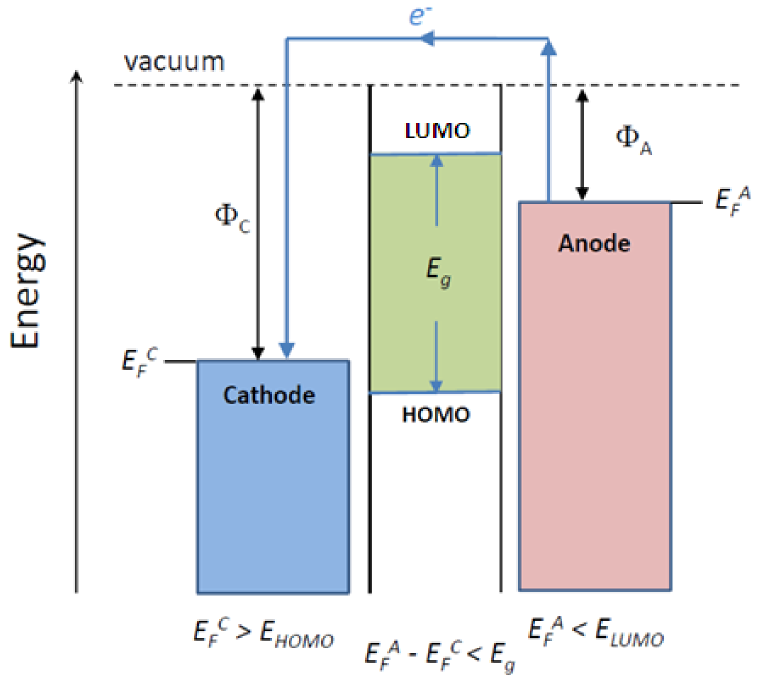

Figure 1. 1 Schematic energy diagram of a battery cell including the three major components: the cathode, anode, and electrolyte. Φ_A and Φ_C are the anode and cathode work functions, respectively. E_g is the window of the electrolyte for the thermodynamic stability. (Reproduced with permission from Ref. [29])

Theoretical calculations can contribute to understanding and improving the design of the electrochemical processes. The energy separation E_g between the lowest unoccupied molecular orbital (LUMO) and the highest occupied molecular orbital (HOMO) of the electrolyte is the window of the electrolyte. The two electrodes are conductors with the Fermi levels (or electrochemical potentials) of $E_F{}^A$ and $E_F{}^C$ for anode and cathode, respectively, which have to be located within the window of the electrolyte to ensure thermodynamic stability of the battery. Therefore, the open-circuit voltage V_{oc} of a battery cell is constrained to the difference between the chemical potentials of the two electrodes,

$$eV_{oc} = E_F^A - E_F^C \le E_g \ , \tag{1.1}$$

where e is the magnitude of the electron charge. The chemical reactions at the electrodes determine the battery voltage. The specific capacity is the reversible charge transfer per unit weight (Ah/g) between the electrodes. The energy density (Wh/g) of a battery cell is expressed as the product of the capacity and the voltage, determined by the chemistry of the two electrodes.

A major challenge in battery development is to maximize the energy density, both gravimetric and volumetric, as many applications constrain the size and/or weight of the battery. For automotive applications, both volume and weight of a battery are important. Currently, the best LIBs for HEVs have energy densities of about 75 Wh/kg and 100 Wh/L, while the best LIBs for battery EVs have energy densities of about 160 Wh/kg and 320 Wh/L [30]. Batteries with high voltages can be constructed by selecting appropriate cathode and anode materials. Graphite is the most commonly used anode material for LIBs, and it operates at a voltage potential close to lithium metal, the low-voltage limit of electrochemical reactions. Therefore, there is little opportunity to increase cell voltage by lowering the voltage of the anode. The recent focus thus turns to the search for high voltage cathode materials [31]. It is important to note, however, that any potential electrode material is not expected to provide the desired performance in all possible aspects. Rather, it has to be chosen according to its practical application. For example, if a fast charging/discharging rate is required, as is the case with HEV or EV industries, rapid Li transport in all component materials is critical to fulfill that purpose.

In addition to the high energy density, the safety issue of LIBs is also crucial in large scale energy storage systems. Currently, most LIBs employ organic liquids as the electrolyte. This choice has created safety problems (*e.g.*, explosion and fire) and has posed a limit for achieving high energy density. For example, liquid electrolytes are expected to react with graphite anode to form a solid-electrolyte-interface (SEI) layer that can significantly decrease battery performance and contribute to the aforementioned safety problems. To address those issues, efforts have been made to replace traditional liquid electrolytes with solid electrolytes [7]. However, the major challenge in practical applications of these solid electrolytes is the relatively low ionic conductivity that is insufficient to meet the LIB's requirements. To search for better solid Li electrolyte materials, further understanding of the Li transport mechanisms will help to improve the ionic conductivity.

From a theoretical perspective, developing rechargeable batteries for use in EVs and other large-scale applications poses two main challenges: the choice of proper electrode materials with the Fermi levels matched well to the window of the electrolyte and the choice of proper electrolyte materials with a larger energy window, allowing a thermodynamically stable voltage higher than 4V (the current electrolyte energy window).

Generally, cathodes and anodes differ mainly in their half-cell voltages (related to their Fermi levels, E_F^C and E_F^A, respectively). In addition to the tailoring of the E_F^C/ E_F^A to the HOMO/LUMO of the electrolyte to be employed, a useful electrode material must meet the following requirements:

- is able to intercalate lithium in a reversible manner;
- has high/low voltage for cathode/anode;
- transports Li quickly during the insertion and removal processes;
- serves as a good electron conductor, preferably a metal;
- is both chemically and structurally stable;
- is cost-efficient;
- and is environmentally benign.

For solid electrolytes, being used to replace aqueous solvents, the most important elements to consider are the following:

- large electrolyte window E_g;
- low electronic conductivity (< 10^{-10} S/cm);
- high Li ionic conductivity (>10^{-4} S/cm over the temperature range of battery operation);
- and good chemical stability.

First-principles molecular dynamics were performed on selected cathodes, anodes, and solid electrolytes of interest. The thesis focuses on the energetics for the migration pathways of Li ions in the electrodes and electrolytes to characterize the transport mechanisms in the three main components of a LIB.

1.3 Thesis outline

The focus of this thesis is on the study of structural and dynamical properties of condensed systems at both ambient and high-pressure conditions through first-principles computational methods. There are two separate objectives: to characterize the structure and atomic dynamics for materials under compression and to investigate Li transport mechanisms in the battery materials at the atomic level. The latter will help with the design of rechargeable LIBs with improved charge and discharge rate.

This thesis is composed of five chapters. The general introduction and the overview of the research is presented in Chapter 1. The essential background of the computational methodologies is described in Chapter 2. Chapter 3 presents results from the study of the atomic dynamics under pressure. The first subject to be investigated is the elucidation of the structure of molten gallium, followed by an examination of hydrogen dynamics in highly compressed solid hydrogen. In Chapter 4, results on the studies of Li transport properties in the cathode, anode, and electrolyte – the three major components of a LIB – are presented. The thesis concludes with a summary of the research and a presentation of future perspectives in Chapter 5.

1.4 Research contributions

A large portion of the research described in this thesis, namely studies of, liquid Ga, solid hydrogen, Li cathode and anode, has been published in four scientific papers. The remaining work in the last section (Sec. 3.2.5) of Chapter 3 as well as Li transport in Li_3PS_4 solid electrolytes is under preparation. In addition, during the course of study, I have contributed one review article that was published as one chapter in a book on Li ion batteries. The references are listed as follows:

<u>Published:</u>

1. Alexander F. Goncharov, John S. Tse, Hui Wang, <u>Jianjun Yang</u>, Viktor Struzhkin, Ross T. Howie, and Eugene Gregoryanz, *Bonding, structures, and bandgap closure of hydrogen at high pressures*. **Phys. Rev. B** 87, 024101 (2013).
2. <u>Jianjun Yang</u> and John S. Tse, *Si Clathrates as Anode Materials for Lithium Ion Batteries?* **J. Mater. Chem. A** 1, 7782 (2013).
3. <u>Jianjun Yang</u> and John S. Tse, Li Ion Diffusion Mechanisms in $LiFePO_4$ – an Ab Initio Molecular Dynamics Study, **J. Phys. Chem. A** 115, 13045 (2011).

4. Jianjun Yang, John S. Tse, and Toshi Iitaka, *First-principles Study of Liquid Gallium at Ambient and High Pressure*, **J. Chem. Phys**., 135, 044507 (2011).

5. John S. Tse, and Jianjun Yang, First-principles methods in the modeling of Li-ion battery materials, in "Lithium-Ion Batteries: Advanced Materials and Technologies" X. Yuan, H. Liu and J. Zhang (Eds), the CRC Press 253-302 (2011).

In preparation:

1. Jianjun Yang and John S. Tse, Near room temperature phase transition of hydrogen at low pressure – an Ab Initio Molecular Dynamics Study, 2014.

2. Jianjun Yang and John S. Tse, First-principles Molecular Dynamics Study on the Li transport mechanisms in the solid electrolyte Li_3PS_4, 2014.

CHAPTER 2

COMPUTATIONAL METHODOLOGY

Even in classical mechanics, the dynamics of a system consisting of more than two bodies has no general analytical solution. To bypass this problem, a method that has proven useful in many cases is numerical simulation. Within the realm of numerical methods, one way to simulate the dynamical properties of a material at the atomic scale is to use molecular dynamics (MD) calculations. In a condensed system, the collective behaviours of the atomic nuclei and electrons can be simulated by first-principles or *ab initio* methods.

First-principles methods, where properties of materials are predicted from the principles of quantum mechanics, are the most powerful tools in physics and chemistry. These methods are based on the basic laws of physics and do not require any experimental input beyond information on the constituent elements and sometimes the crystal structure. While the static ground state of a condensed system at zero temperature can be calculated through electronic structure theory, temperature effects can be simulated using MD methods. The macroscopic temperature is equated to the average kinetic energy *via* the equipartition theorem. MD calculations can also provide information on the temporal evolution of the atomic positions and velocities. Therefore, it is a method that helps to bridge the microscopic structures and macroscopic properties observed experimentally.

First-principles molecular dynamics (FPMD) technique is a unification of classical molecular dynamics and electronic structure methods to “realistically” simulate complex many-body systems. This method has been employed in the investigation of a large number of physical, chemical and biological phenomena. It is an indispensable tool in the study of the dynamics of crystalline and disordered condensed systems. In this thesis, all calculations were performed with first-principles methods, including electronic structure calculations, geometry optimization, and MD simulations. In this chapter, the theoretical background of these methods will be introduced briefly. We start with the density functional theories (DFT) in which all calculations were based. DFT is an exact quantum mechanical theory of correlated many-body systems and has tremendous impact on the calculation of the electronic structure of solids. Next, the FPMD method employed in the thesis work is introduced. Finally, the major methods to analyze the theoretical results are presented.

2.1 Electronic structure theory and the density functional theory

The microscopic description of a condensed matter is a system constructed from nuclei and electrons that interact with each other through Coulomb interactions. According to quantum mechanics, in principle any observable can be calculated from the appropriate operator in the integral of the wave function over space, where the wave function of the system is determined by solving the many-body Schrödinger equation

$$H\Psi(\{\mathbf{r}_i,\mathbf{R}_I\}) = E\Psi(\{\mathbf{r}_i,\mathbf{R}_I\}), \tag{2.1}$$

where *H* is the Hamiltonian for the system of electrons and nuclei (in CGS units), and

$$\begin{aligned} H &= H_{ee} + H_{eN} + H_{NN} \\ &= -\sum_i \frac{\hbar^2}{2m_e}\nabla_i^2 + \frac{1}{2}\sum_{i,j(i\neq j)} \frac{e^2}{\left|\mathbf{r}_i - \mathbf{r}_j\right|} - \sum_{i,I} \frac{Z_I e^2}{\left|\mathbf{r}_i - \mathbf{R}_I\right|} \\ &\quad -\sum_I \frac{\hbar^2}{2M_I}\nabla_I^2 + \frac{1}{2}\sum_{I,J(I\neq J)} \frac{Z_I Z_J e^2}{\left|\mathbf{R}_I - \mathbf{R}_J\right|}. \end{aligned} \tag{2.2}$$

Here, the upper and lower case indices represent nuclei and electrons, respectively. $\mathbf{R}_I$ ($\mathbf{r}_i$) and M_I (m_e) represent the corresponding positions and masses of the nucleus (electron), respectively. Z_I is the atomic number and $-e$ is the electron charge. As per the equations above, the Hamiltonian consists of kinetic energy and potential energy due to interactions between the nuclei and electrons.

An approximation to decouple the electronic degrees of freedom from the nuclei is the Born-Oppenheimer approximation [32]. This is motivated mainly by the fact that electrons are much lighter and therefore move about three orders of magnitude faster than the nuclei. In this approximation, the nuclei are regarded as fixed ions acting as an external potential. This approximation has proved to be sufficiently accurate for a large number of interesting systems. All first-principles calculations performed in this thesis have been done using the Born-Oppenheimer approximation. The behaviour of interacting electrons in the external potential created by the nuclei is described by the following Hamiltonian, from Eq.(2.2):

$$H = -\sum_i \frac{\hbar^2}{2m_e}\nabla_i^2 + \frac{1}{2}\sum_{i,j(i\neq j)} \frac{e^2}{\left|\mathbf{r}_i - \mathbf{r}_j\right|} - \sum_{i\,I} \frac{Z_I e^2}{\left|\mathbf{r}_i - \mathbf{R}_I\right|} \quad . \tag{2.3}$$

In this equation, the last term is the external potential describing the Coulomb interaction between the electrons and a given configuration of the nuclei. The periodic boundary condition (PBC) is imposed for solids such that external potential is determined explicitly by the Bravais lattice vectors and internal atomic coordinates. The second term in Eq.(2.3) describes the electron-electron Coulomb interactions. This term involves all electronic degrees of freedom, which makes it intractable to solve the equation. A remedy is the independent one-electron wave function which is a very good approximation. This is known as the Hartree approximation, where the many-body wave function is represented by a product of the wave functions of individual electrons. Taking the fermionic exchange of electrons into account, a Slater-determinant [33] of independent one-electron wave functions often gives a good approximation.

2.1.1 Hohenberg-Kohn theorems

The basic idea of DFT is to show the electronic density as the basic variable in the description of a many-body system. This theory dramatically simplifies the many–body Schrödinger equation (2.3). It is based on two theorems proposed by Hohenberg and Kohn [34] (H-K) in 1964 wherein the total energy of a system is dependent only upon density.

Theorem 1 For any system of interacting particles in an external $V_{ext}(\mathbf{r})$ potential,, the external potential and hence the total energy is determined uniquely - except for a constant - by the ground state particle $n_0(\mathbf{r})$ density .

Theorem 2 A universal functional for $E[n]$ energy in terms of density $n(\mathbf{r})$ can be defined and is valid for any external potential $V_{ext}(\mathbf{r})$. For any particular $V_{ext}(\mathbf{r})$, the exact ground state energy of the system is the global minimum value of this functional, and the density $n(\mathbf{r})$ that minimizes the functional is the exact ground state density $n_0(\mathbf{r})$.

The first H-K theorem implies that if the density of the system is known, everything about the system can be determined since the density of a system corresponds uniquely to the external potential. Therefore, in order to solve the problem, we only need to find the ground state density. The second H-K theorem provides a way to do this by finding the ground state energy functional. However, so far the exact energy functional of an interacting many-body system is not known. Kohn and Sham [35] have proposed a practical scheme for DFT as will be described in detail below.

2.1.2 Kohn-Sham equations

The Kohn-Sham (KS) approach states that there is a system of *non-interacting* particles corresponding to a system of *interacting* particles with the same ground state density. This means that instead of solving a system of interacting particles in a "simple" external potential, we can try to solve a system of independent particles in a "complex" effective potential with the same electron density, thereby reducing all the many-body interactions in the system to an effective potential. Therefore, the electrons will only interact through the effective potential.

Following the KS approach [35], a set of single-particle Schrödinger-like equations for the interacting electron system – known as the Kohn-Sham equations – was derived:

$$\left(-\frac{\hbar^2}{2m_e}\nabla^2 + V_{\text{eff}}\left(\mathbf{r}\right)\right)\varphi_i\left(\mathbf{r}\right) = \epsilon_i\varphi_i\left(\mathbf{r}\right) \tag{2.4}$$

with the effective potential defined as,

$$V_{\text{eff}}\left(\mathbf{r}\right) = V_{ext}\left(\mathbf{r}\right) + \int \frac{n\left(\mathbf{r}'\right)}{\left|\mathbf{r}-\mathbf{r}'\right|}d\mathbf{r}' + \frac{\delta E_{xc}\left[n\left(\mathbf{r}\right)\right]}{\delta n\left(\mathbf{r}\right)} \ . \tag{2.5}$$

The righthand side of Eq. **(2.5)** contains the external potential, the electron-density interaction and the exchange-correlation as represented by the last term. Note that $\varphi_i\left(\mathbf{r}\right)$ is the single-particle wave function in the interacting electrons system often referred to as the KS orbital. The electron density is simply a sum over squares of the KS orbitals:

$$n(\mathbf{r}) = \sum_i \left|\varphi_i(\mathbf{r})\right|^2 \ . \tag{2.6}$$

As a result, the ground state total energy of a quantum matter, including both electrons and nuclei, can be expressed by a functional of the electron density $n(\mathbf{r})$:

$$E_{total}[n] = E_{electron}[n] + E_{ion} \quad . \tag{2.7}$$

Here, E_{ion} is the Coulomb energy between nuclei determined explicitly by the atomic configurations. The electronic contribution $E_{electron}[n]$ functional is written as,

$$E_{electron}[n(\mathbf{r})] = T_0[n(\mathbf{r})] + \frac{1}{2}\iint d\mathbf{r}d\mathbf{r}'\frac{n(\mathbf{r})n(\mathbf{r}')}{|\mathbf{r}-\mathbf{r}'|} + E_{xc}[n(\mathbf{r})] + \int d\mathbf{r}V_{ext}(\mathbf{r})n(\mathbf{r}) \quad , \tag{2.8}$$

$$T_0[n(\mathbf{r})] = \sum_i \int d\mathbf{r}\varphi_i^*(\mathbf{r})(-\frac{\hbar^2}{2m_e}\nabla^2)\varphi_i(\mathbf{r}) \quad . \tag{2.9}$$

As seen in Eq.**(2.8)**, the electron energy consists of the kinetic energy $T_0(n)$ of independent electrons, the Hartree Coulomb energy, the exchange-correlation energy functional $E_{xc}[n]$ and the external potential energy.

The correct ground-state total energy can be obtained by minimizing the electronic energy functional in terms of ground-state electron density $n(\mathbf{r})$, subject to constraint on the conserved electron number N:

$$\int_V d\mathbf{r}n(\mathbf{r}) = N \quad . \tag{2.10}$$

It is important to note in Eq.(2.8) that kinetic energy is calculated from non-interacting particles and the Hartree term can also be calculated explicitly. However, the exact functional for the exchange-correlation term $E_{xc}[n]$ is unknown, and thus the problem is still intractable. To address this issue, an approximation to exchange-correlation energy is needed.

2.1.3 Exchange-correlation functionals

Up to this point, the DFT approach has provided a practical procedure to solve the many-body problem by transforming the many-body *wave function* into a set of single-particle problems. However, due to the unknown exact form of the exchange-correlation term $E_{xc}[n]$, we are forced to find approximations for this term to make the formalism useful.

The most common and straightforward approximation to $E_{xc}[n]$ is the Local Density Approximation (LDA) [35]. The intent of the LDA is to treat a general *inhomogenous* electronic system as locally *homogeneous*. It is assumed that the exchange-correlation energy per electron of a *non-uniform* system at any point in space is equal to the exchange-correlation energy per electron in a *uniform* electron gas having the same density at this point. Thus,

$$E_{xc}^{LDA}[n] = \int d\mathbf{r} n(\mathbf{r}) \varepsilon_{xc}[n] \tag{2.11}$$

with

$$\varepsilon_{xc}[n] = \varepsilon_{xc}^{uniform}[n] \ . \tag{2.12}$$

By definition, the LDA is local as the $\varepsilon_{xc}[n]$ at each point in space depends only on the electron density at that same point. The $\varepsilon_{xc}^{uniform}[n]$ has been calculated and parameterized for different values of the density using Monte Carlo techniques [36].

Since the LDA is based on uniform electron gas, it is expected to be accurate only for systems in which the electron density varies very slowly, as with most bulk metals. It is not suitable for situations where the electron density undergoes rapid changes, as is the case for covalently-bonded solids, molecules and surface systems. To overcome this drawback and address the inhomogeneous issue, a new form of exchange-correlation functional was developed, which depends on the local electron density as well as the spatial density gradient, to improve the

LDA. This is called the Generalized Gradient Approximation (GGA) [37-40]. The GGA functional can be written as

$$E_{xc}^{GGA}[n] = \int d\mathbf{r} n(\mathbf{r}) \varepsilon_{xc}^{GGA}[n, \nabla n] . \qquad (2.13)$$

Conventionally, E_{xc} is assumed to be separate as the sum of exchange functional E_x and correlation functional E_c. The E_{xc}^{GGA} can be defined over local exchange as

$$E_{xc}^{GGA}[n] = \int d\mathbf{r} \varepsilon_x^{uniform}[n] F_{xc}[n, \nabla n] n(\mathbf{r}) \ , \qquad (2.14)$$

where $\varepsilon_x^{uniform} = -3k_F / (4\pi)$ is the Slater exchange energy density in the uniform electron approximation [41]. $k_F = [3\pi^2 n(\mathbf{r})]^{1/3}$ is the local Fermi wave vector. The analytic form of F_{xc} includes the correlation term E_c and exchange term F_x. F_x is the enhancement factor in the exchange functional and is a function of a dimensionless density gradient *s*, defined as $s = |\nabla n(\mathbf{r})| (2k_F n(\mathbf{r}))$. The correlation functional E_c is given by

$$E_c = \int d\mathbf{r} n(\mathbf{r}) \{\varepsilon_c[n] + H(t, r_s, V)\} . \qquad (2.15)$$

Here, r_s is the Seitz radius and ς is the spin polarization. The parameter *t* or scale density gradient is another dimensionless term defined as $t = |\nabla n(\mathbf{r})| / (2 g k_s n(\mathbf{r}))$ where $g = [(1+\varsigma)^{2/3} + (1-\varsigma)^{2/3}] / 2$ and $k_s = (4k_F / \pi)^{1/2}$. The term $\varepsilon_c[n]$ is the correlation energy density of a uniform electron gas. $H(t, r_s, \varsigma)$ is the correlation term to be parameterized.

Unlike a unique form for LDA, GGA can have many different forms depending on the parameterization. Examples of this include the Becke [37], the Becke-Lee-Yang-Parr (BLYP) [38], the Perdew-Wang 91 (PW91) [39] and its simplified version, the Perdew-Burke-Ernzerhof (PBE) [40]. Among this class of functionals, the PBE parameterization [40] is the most successful and commonly used. In the PBE functional, the exchange enhancement factor is denoted as

$$F_x^{PBE}(s) = 1 + \kappa - \frac{\kappa}{1 + \mu s^2 / \kappa} \tag{2.16}$$

where $\mu \sim 0.2195$ and $\kappa \sim 0.804$. The correlation term $H(t, r_s, \varsigma)$ in Eq.(2.15) is written as

$$H(t, r_s, \varsigma) = \gamma g^3 \log\left(1 + \frac{\gamma}{\beta} t^2 \frac{1 + At^2}{1 + At^2 + A^2 t^4}\right) \tag{2.17}$$

with $\beta \sim 0.0667$, $\gamma \sim 0.031$ and

$$A = \frac{\beta}{\gamma}\left[\exp\left(\frac{-\varepsilon_c(r_s, \varsigma)}{\gamma g^3} - 1\right)\right]^{-1} . \tag{2.18}$$

Significant improvements have been observed using the PBE functional over the LDA in the prediction of total energies, structural geometries, bulk modulus, atomic total energies and vibrational properties.

2.1.4 DFT+U

Despite the great success of DFT with LDA and GGA functionals, there are still inherent deficiencies when describing strongly correlated effects (*e.g.*, between localized *d* electrons in the transition metal oxides [40]). Additionally, since the Coulomb and exchange terms are calculated separately in Eq.(2.5), the self-interaction is not canceled exactly.

The shortcomings for the correlation and self-interaction effects with DFT can be amended with a simple DFT+U scheme based on the Hubbard model [42, 43]. Since the strong on-site Coulomb interaction is the source of strong electron correlation, the main idea of the

DFT+U method is to separate electrons into two subsystems: the strongly localized *d* (or *f* for the lanthanides) electrons and the delocalized *s* and *p* electrons. While the latter case still could be described using an orbital-independent one-electron potential such as LDA or GGA, the strong *d*-*d* Coulomb interaction in the former case is taken into account by adding a term, $E^{U} = \frac{1}{2} U \sum_{i \neq j} n_i n_j$, in the Hamiltonian. Here, *U* is the Hubbard parameter and n_i (n_j) is the occupancy of the *i*th (*j*th) *d* (or *f*) orbital. This method can be summarized by the expression of the new functional

$$E^{DFT+U}\left[n\right] = E^{DFT}\left[n\right] + E^{U}\left[n_i^{\sigma}\right] - E^{dc}\left[n_i^{\sigma}\right] , \tag{2.19}$$

where $E^{dc}\left[n_i^{\sigma}\right]$ is called the "double counting" term. As this term is included explicitly in the Hubbard term, it is necessary to remove the energy contribution of these orbitals in the LDA/GGA functional so as not to count them twice. E^{dc} is approximated as the mean-field value of the Hubbard term E^{U}. Therefore, the mean value of E^{dc} is *UN*(*N*-1)/2, where *N* is the total number of *d* (*f*) electrons $N = \sum_i n_i$. The *U* value varies for different transition metals, which makes determining the appropriate *U* for each compound a necessity. The value of *U* can be determined theoretically using methods such as the recently developed linear response method [43]. A simple approach involves selecting the value to match experimentally measured properties such as magnetic moments, band gaps [44] or lithium insertion voltages [45]. GGA+*U* calculations are used widely in combination with the plane-wave basis sets, as will be explained in the next section. In most cases this approach permits very accurate reproduction of electronic structures of insulators/semiconductors such as the band gap that is strongly underestimated in standard DFT calculations.

2.1.5 Periodic boundary conditions, and *k*-point sampling

Since there exists a large number of electrons (on the order of Avogradro's number 6.022×10^{23}) in a solid or other condensed matter, the solutions to the KS equations in Eq.(2.4) are still intractable. While the one-electron wave function of a metallic solid extends throughout the entire system, the basis set required to expand the KS orbital is infinite. Fortunately, perfect crystals can be described as spatially repeated unit cells that contain only a small number of nuclei and electrons. This leads to the use of PBC according to the Bloch theorem. The Bloch theorem states that the solution of the single-particle Schrödinger equation (*i.e.*, KS equation) in the presence of a periodic potential must have the form

$$\psi_j(\mathbf{k},\mathbf{r}) = e^{i\mathbf{k}\cdot\mathbf{r}} u_j(\mathbf{k},\mathbf{r}) \ , \tag{2.20}$$

where j represents the band, **k** represents the wave vector of the electron in the first Brillouin zone (BZ) and $u_j(\mathbf{k},\mathbf{r})$ is a periodic function where $u_j(\mathbf{k},\mathbf{r}) = u_j(\mathbf{k},\mathbf{r}+\mathbf{R})$ for any reciprocal lattice vector **R**. Thus, Eq. (2.20) can be rewritten as

$$\psi_j(\mathbf{k},\mathbf{r}+\mathbf{R}) = e^{i\mathbf{k}\cdot\mathbf{R}} \psi_j(\mathbf{k},\mathbf{r}) \ . \tag{2.21}$$

By substituting Eq.(2.21) into the KS equation Eq.(2.4), a new set of eigen-equations, each for a given **k,** was found. Each electron occupies an electronic state of definite wave vector **k**. The Bloch wave functions confine the calculation of a very large system (approximately Avogadro's number) into a single unit cell. Therefore, the problem of solving for an infinite number (~10^{23}) of electrons within the extended system is converted to solving for a finite number of electronic bands at an infinite number of *k*-points within the single (reciprocal) unit cell. Changing from one infinite number to another, however, does not make the problem simpler. Knowing that electronic wave functions at those *k*-points being close to each other are very similar, in practice, one can represent the wave functions over a small region of reciprocal space around one *k*-point by the wave function at that *k*-point. Therefore, only a finite number of *k*-points are needed to determine the ground state of solids.

Many efficient schemes have been developed for *k*-point sampling inside the first BZ. Using these schemes, one can obtain very good approximations for the electron potential and total energy of a solid. Any integral over almost continuous *k*-points in the first BZ is thus represented by the summation over a *k*-points mesh

$$\frac{V}{(2\pi)^3}\int_V d\mathbf{k} f(\mathbf{k}) \sim \sum_i f(\mathbf{k}_i) w_i \ , \qquad (2.22)$$

where w_i is the weight of the point $\mathbf{k}_i$. The most widely used scheme for the *k*-point sampling was developed by Monkhorst and Pack [46], known as the MP mesh. The MP mesh utilizes the space group symmetries of the lattice to reduce the number of *k* points by confining the sampling only to the irreducible wedge of the first BZ. The *k*-points are also selected according to their point group symmetries, which in turn determines the weight w_i. This scheme achieves a sufficient sampling with a very small number of *k*-points. The density of allowed *k*-points is generally proportional to the volume of the solid. The magnitude of error in the calculated total energy due to insufficient *k*-point sampling can always be reduced by using a denser *k*-point mesh.

It is noted that in addition to bulk solids, PBC can also be applied in the study of non-periodic systems such as isolated molecules and surfaces. For example, when studying surfaces it is common to retain periodicity in two dimensions and discard it in the direction perpendicular to the surface. In some cases, even the study of a liquid can make use of PBC in the first-principles calculations, as long as the size of the model system is large enough.

2.1.6 Plane-wave basis sets

Up to this point, it is possible to solve the KS equations in Eq.(2.4) with approximations of exchange-correlation functionals and by employing PBC. It is noted in Eq.(2.20) that in order to solve the KS equations numerically, KS orbitals need to be expanded by well-behaved basis sets such as plane-wave (PW) or atomic orbitals. The PW basis set is the most straightforward for solids. Plane-waves are exact eigenfunctions of the homogeneous electron gas. Plane-waves are not biased to any particular atom or its position. They form a complete basis set with very simple mathematical functions. The completeness of the basis set is easy to adjust and essentially only requires one parameter known as the kinetic energy cutoff E_{cut} .

Using the PW basis set, the KS orbital can be expanded as

$$\psi_j(\mathbf{k},\mathbf{r}) = e^{i\mathbf{k}\cdot\mathbf{r}} u_j(\mathbf{k},\mathbf{r}) = \frac{1}{\sqrt{V}} \sum_{\mathbf{G}} c_{j,\mathbf{k}+\mathbf{G}} \cdot e^{i\mathbf{G}\cdot\mathbf{r}} \cdot e^{i\mathbf{k}\cdot\mathbf{r}} \quad , \tag{2.23}$$

where **G** is the reciprocal lattice vector. In principle, an infinite basis set of G should be used to expand the KS orbital. In practice, it is possible to truncate the infinite basis set to include only the PWs with kinetic energies less than a defined cutoff energy E_{cut} :

$$|\mathbf{k}+\mathbf{G}| < G_{cut} \tag{2.24}$$

with

$$E_{cut} = \frac{\hbar^2}{2m_e} G_{cut}^2 \quad . \tag{2.25}$$

It can be seen from the above two equations that the number of PWs differs for each *k*-point. Clearly, the truncation of the PW basis set will introduce some error in the calculated total energy. However, this error should gradually decrease by increasing the energy cutoff E_{cut}. It is noted that a larger energy cutoff will increase the computational workload significantly. Therefore, in practical calculations, the assigned E_{cut} value should be well-tested to reach a good convergence of the calculated total energy but maintain an affordable computational efficiency.

2.1.7 Pseudopotential approximation

One of the main problems with the use of PWs as a basis set is the expensive PW expansion in the core region. Since the potential at the nuclear core region is steep (~ $1/r$) and all one-particle wave functions have to be orthogonal, the resulting orbital wave functions oscillate rapidly in the core region. Expanding oscillatory wave functions requires a large number of PW components. One way to solve this problem is to modify the potential. The modified potential is known as *pseudopotential* [47]. Since the core region of the atom is usually not involved in the bonding of specific materials, the core electrons and ionic potential can be pre-calculated and replaced with a smooth (nodeless) part, making the PW expansion much more effective. In this approximation, only the valence electrons outside the core region are considered. The pseudopotential acts on a set of pseudo wave functions instead of the true valence wave functions.

As a general rule, the constructed pseudopotential and pseudo wave functions should be identical to the all-electron potential and valence wave function in the valence region $r > r_c$, as shown in Figure 2. 1. The cutoff radius r_c is determined by the fact that the core regions of neighbouring atoms should not overlap. Choosing a smaller core cutoff radius usually means improving the transferability of the pseudopotential, making it suitable for a more diverse chemical environment. However, a small core cutoff also makes the pseudo wave functions tighter and therefore more PWs are needed in the expansion.

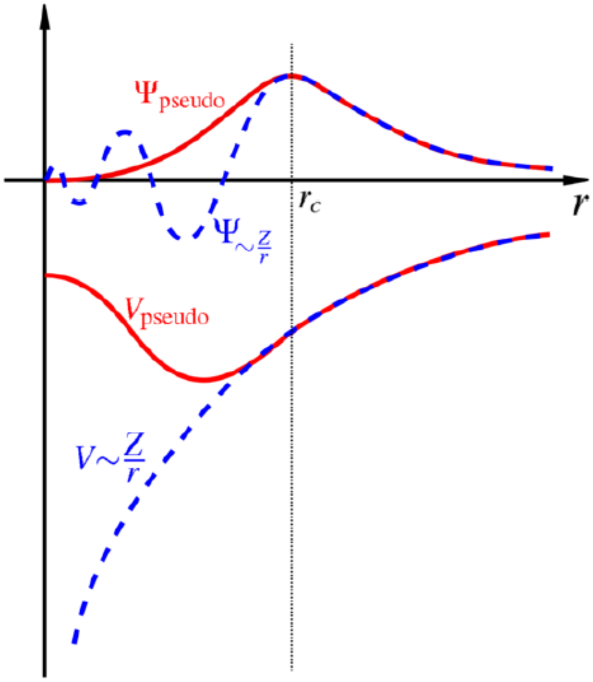

Figure 2. 1 Comparison of the pseudopotential (dashed) Coulombic potential (solid) of an atom (dashed curves) and the corresponding pseudo wave function (dashed) with the all electron wave function (solid curves).

The Projector Augmented Waves (PAW) method [16] is an alternative to the pseudopotential method. In principle, PAW is an all-electron potential that has been demonstrated as a very successful scheme for accurate and efficient calculation of the electronic structure of materials. PAW potential takes advantage of many ideas developed in the pseudopotential concept by reconstructing all-electron core wave functions from the pseudo wave functions in the core region [48]. When the all-electron partial waves are added to the total wave function, the corresponding pseudo partial waves must be subtracted (see Figure 2. 2). The reconstructed all-electron wave function is therefore a combination of the pseudo wave function outside the core region and the all-electron wave function inside the core region [48].

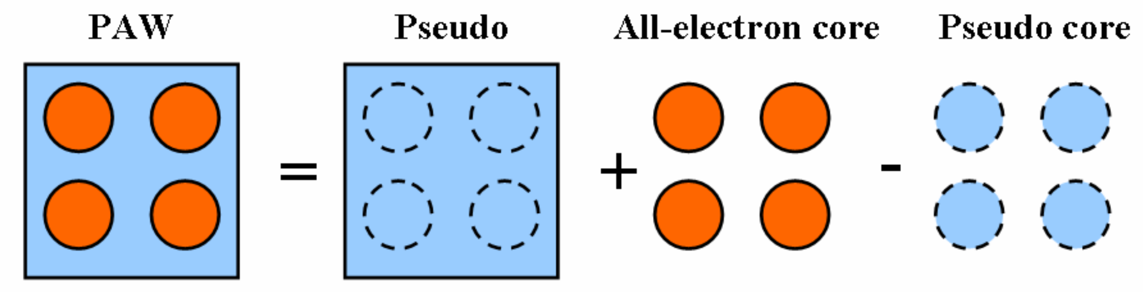

Figure 2. 2 A simplified depiction of reconstructed PAW wave function that contains onsite and out-of-site contributions from all-electron and pseudo wave functions.

2.1.8 Self-consistent solution

All ingredients needed to practically solve the KS equations are now completely described. In practice, the ground-state electron density can be solved self-consistently using the pseudopotential plane-wave method [49, 50]. This procedure is illustrated in the flow chart in Figure 2. 3.

The self-consistent calculation starts with an initial guess of electron density that is usually constructed by superimposing the electron densities of non-interacting atoms. From this electron density an effective potential $V_{\mathbf{eff}}(n)$ is constructed. The set of KS equations can now be solved for each *k*-point, producing a set of pseudo wave functions described by a finite set of PWs and truncated at the kinetic energy cutoff E_{cut}. The resulting KS orbitals are used to build a new electron density via Eq.(2.6) and convergence is checked by comparing the output and input densities. If the difference is beyond a tolerance, one has to construct a new set of potentials using the new electron density and repeat the calculations again. To speed up the convergence, the new input density can be constructed by mixing the output density from the last step with previous densities. This calculation is repeated until the solutions are self-consistent, where the output density is found to be sufficiently close to the input density. Once the convergence is achieved, the ground-state total energy, KS energies, KS orbitals, as well as forces can be calculated.

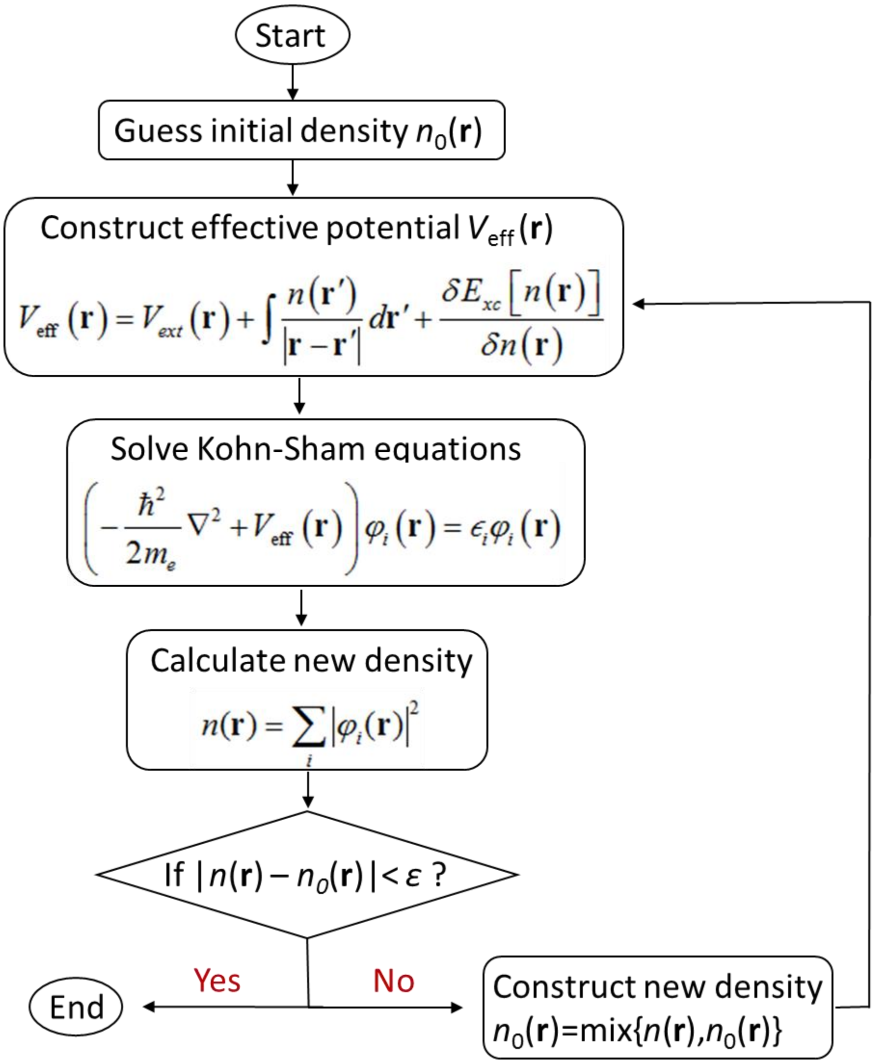

Figure 2. 3 Flowchart illustrating the basic steps in the Kohn-Sham self-consistency loop.

2.2 Nudged elastic band method

The nudged elastic band (NEB) method [51, 52] is used to trace a transition pathway when both the initial and final structures are known. This method works by interpolating a set of “images” linearly between the known initial and a guess final structure. The structure of each “image” is optimized and the total energy is calculated. The “image” is then moved according to the residual force acting perpendicularly to the path (F_{NEB}), which is an artificial spring force that keeps the “images” spaced along the minimum energy path (MEP). The procedure is then repeated when the final minimum energy structure is reached. Each "image" corresponds to a specific geometry of the atoms on their way from the initial to the final state. Thus, once the energy of this string of “images” has been calculated, the MEP for the transformation is obtained. The transition state for the transformation is the highest energy “image” along this trajectory. A schematic representation of the computational process is shown in Figure 2. 4.

An improved NEB method known as the climbing nudged elastic band (cNEB) scheme was further developed by Henkelman’s group [53, 54]. In this method, the highest energy “image” is driven up to the saddle point. This “image” does not feel the spring forces along the band; rather, its true force along the tangent is inverted. In this way, the “image” tries to maximize its energy along the band and minimize in all other directions. When this “image” converges, it will be at the exact saddle point or transition state.

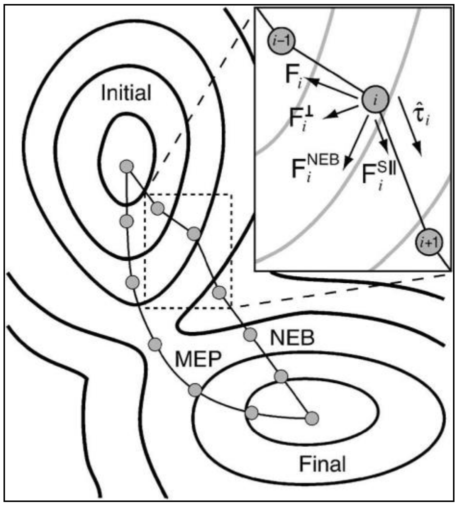

Figure 2. 4 A schematic potential energy surface showing the minimum energy pathway as determined by the nudged elastic band method. (Reproduced from http://theory.cm.utexas.edu/henkelman/research/saddle/)

2.3 First-principles molecular dynamics

As discussed above, the ground-state properties of solids can be determined through DFT-based electronic structure calculations. In practice, the properties observed for a material are for its electronic state at finite temperatures. MD, sometimes called a “virtual laboratory approach”, is a numerical method to simulate materials at the atomistic level in order to understand and predict a system’s behaviours by purely theoretical means. A variety of thermodynamic properties can be calculated and structural information on temperature dependent conformational changes can be determined from the MD trajectory. This technique is a popular computational tool to study dynamical chemical and biological processes and particularly to study atomic diffusion and the breaking and making of chemical bonds.

2.3.1 A simple MD program

Classical molecular dynamics is essentially the propagation of a system according to the Newtonian equations of motion,

$$\mathbf{F}_I = M_I \mathbf{a}_I = M_I \ddot{\mathbf{R}}_I \tag{2.26}$$

and

$$\mathbf{F}_I = -\nabla U(\mathbf{r}_I)\,, \tag{2.27}$$

where $\mathbf{F}_I$ denotes the force exerted on the atoms I by all other atoms in the system and M_I, $\mathbf{a}_I$ and $\mathbf{R}_I$ are the mass, acceleration vector, and generalized coordinates of that atom. As can be seen in Eq.(2.27), force can be calculated from the first derivative of the intermolecular potential $U(\mathbf{r}_I)$ with respect to the coordinate vector $\mathbf{r}_I$. Detailed information about the intermolecular potential will be discussed later. From the two above equations, atomic movements can then be calculated as a function of time to generate a trajectory.

As necessary inputs for MD simulation, atoms need to have defined positions in space that can be obtained from the experimental structure. Apart from the atoms' positions, the temperature of the system is determined by the starting velocities of the atoms. These velocities are generated from a random number adhering to the Maxwell distribution at the initial temperature. As seen in Figure 2.5, the basic MD loop is composed of two steps: the force evaluation and the integration of the equations of motion.

To solve the Newtonian equations of motion, the forces between atoms have to be calculated. In FPMD, the instantaneous forces acting on individual atoms are calculated by the Hellman-Feynman theorem [55] once the wave functions of the system are determined from the self-consistent calculations. With Born-Oppenheimer MD, the electronic structure part is reduced to solving the ground-state of the stationary Schrödinger equation. In another word, the static electronic structure problem in each MD step is solvable given the set of fixed nuclear positions at that instant in time. The resulting Born-Oppenheimer MD in Eqs.(2.26) and (2.27) can be rewritten as

$$M_I \ddot{\mathbf{R}}_I(t) = -\nabla_I \left\langle \Psi_0 \middle| H_e \middle| \Psi_0 \right\rangle , \tag{2.28}$$

$$E_0 \Psi_0 = H_e \Psi_0 . \tag{2.29}$$

Here, H_e is the static Hamiltonian of the electronic system for a given atomic configuration $\{\mathbf{R}_I(t)\}$ at time *t*, and E_0 and Ψ_0 are the corresponding ground state energy and wave function.

As shown in Eq. (2.28), the forces acting on the nuclei can be calculated from the electronic structure calculations. From the Hellmann-Feynman theorem [55], forces calculated from the SCF wave functions are then used in the Newtonian equations of motion to propagate the atoms. The most common scheme is the Velocity Verlet method [56], which is numerically stable and simple to implement. The time step for the integration is usually in the order of femtoseconds ($1fs = 10^{-15} s$). The MD loop is executed for each time step (see Figure 2. 5). All forces between atoms are calculated using the Hellman-Feynman theorem after solving the Schrödinger equation. Atoms are then propagated according to forces by solving the Newtonian equations of motion. Relevant properties of the system can be calculated from the atom positions, velocities and forces. The most important properties are the total energy and the temperature or kinetic energy of the system. The temperature is important because it directly influences the atom's motions. When the simulation is finished, a large amount of data including the instantaneous atomic positions, forces, energies and temperatures is generated. Post-processing analysis of the collected data can be used to extract relevant physical properties.

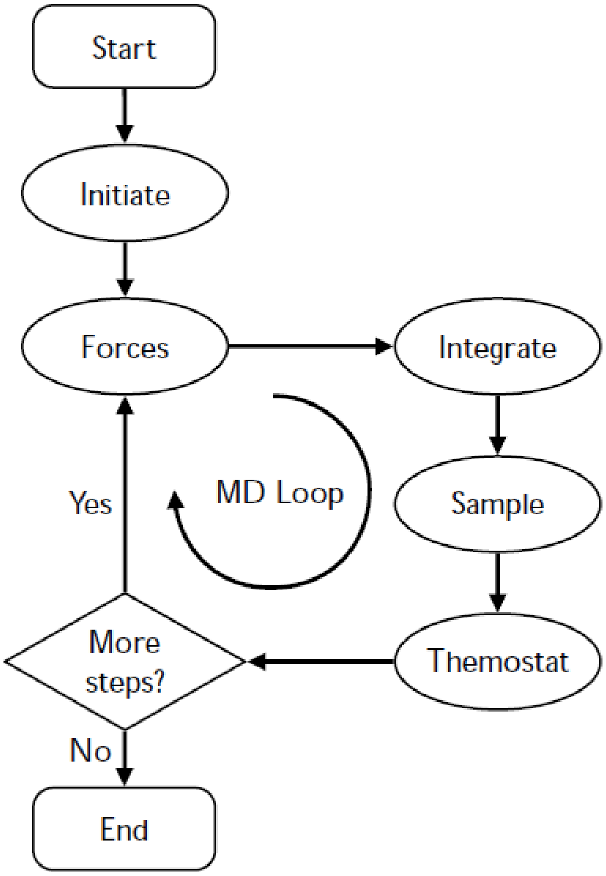

Figure 2. 5 The basic MD loop.

2.3.2 Velocity Verlet algorithm

The Velocity Verlet integrator [56] is probably the most commonly used integrator, giving the trajectories and velocities in a very straightforward way. It provides positions, velocities and forces at the same time step. This algorithm gives good long-time accuracy at the cost of a poorer short-time accuracy, resulting in shorter allowed timesteps. The positions (*r)* and velocities (*v*) at the next time step are generated by

$$r(t+\delta t) = r(t) + v(t)\delta t + \frac{f(t)}{2m}\delta t^2 \ , \tag{2.30}$$

and

$$v(t+\delta t) = v(t) + \frac{f(t+\delta t) + f(t)}{2m}\delta t \ , \tag{2.31}$$

where *f* is the force and *m* is the mass of the atom. With this method, velocities need to be calculated based on the velocity and force from the previous time step and the force calculated from the current position.

2.3.3 Post-processing methods

A large part of the computational work is performed after the MD simulation is complete. The direct result of any MD simulation is a trajectory containing the positions and velocities of the particles in a system at discrete time steps. Depending on the desired information, different analysis methods can be performed. An examination of atomic motions in real space can be accomplished by highlighting specific atoms with different colours. Calculations of autocorrelation functions and mean squared displacement functions yield dynamical properties of the system.

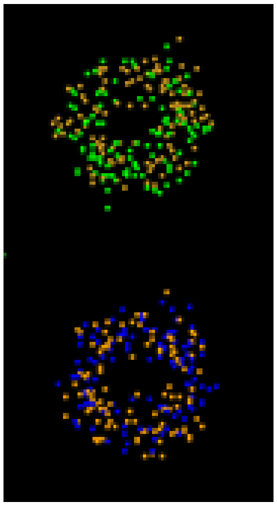

Figure 2. 6 Illustration of the trajectories of several atoms represented with different colours.

Trajectory colour coding

Colour coding was used in this thesis work to investigate the atomic dynamics by examining the collected atomic trajectory directly. Using this method, the atomic positions along the simulation (represented by dots in three-dimensional (3D) space) were plotted by assigning colour codes to different atoms or atomic species. Through an analysis of the evolution of same-coloured dots, the diffusion or other dynamical process of the corresponding atoms can be identified. These methods are useful to investigate the slow dynamical process (see the $LiFePO_4$ study in Chapter 4) as well as to study possible dynamical structural behaviour (see the hydrogen system in Chapter 3). For example, Figure 2. 6 shows a colour-coded trajectory for a number of atoms. When one examines the plot, one notes that the trajectory is a round, cloud-like spread over fixed lattice sites. Within each cloud, two colours are identified and the colour distribution is quite even with spherical shape. This indicates that the two atoms are bound together and rotate around their bond center. Therefore, the rotating molecules can be identified without further analysis.

Time-correlation functions

Time-correlation functions are an effective and intuitive way of representing the dynamics of a system. They provide a statistical description of the time-evolution of a variable for an ensemble at thermal equilibrium. A time-correlation function is defined as

$$C(t) \equiv \langle A(0)A(t) \rangle , \tag{2.32}$$

where $\langle \cdots \rangle$ represents an ensemble average and A is the dynamic variable of interest (*e.g.*, velocity, bond fluctuation, vector reorientation, *etc.*) Eq.(2.32) is technically a time autocorrelation function, as it correlates the same variable at two points in time. The autocorrelation function measures how the value of a dynamic quantity A at time t is dependent on its initial value. It describes how long a given property of a system persists until it is averaged out by microscopic motions and interactions with its surroundings. It also describes how and when the statistical relationship vanishes. If the temporal value of $A(t)$ is comparable with the value at zero time $A(0)$, this indicates that the property represented by A is highly correlated. In a liquid, this often happens in a short time interval but the correlation eventually decays to zero at long-time.

Since the atomic velocities are manifestations of the dynamics in a system, the atom velocity autocorrelation function (VACF) is the most convenient way to analyze dynamical properties. Information about relevant dynamical processes is contained in the fluctuations and time decay of VACF. The typical VACFs for a liquid and a solid are compared in Figure 2. 7. In solids or dense liquids, the oscillatory patterns characterize the vibrating motion of particles in the system. The oscillatory VACF always decays at long-time as random forces acting on the atoms destroy the correlated motions. In liquids, the diffusion motion leads to heavy damping of the oscillatory behaviour as there is less chance to collide with the surrounding atoms before they diffuse away.

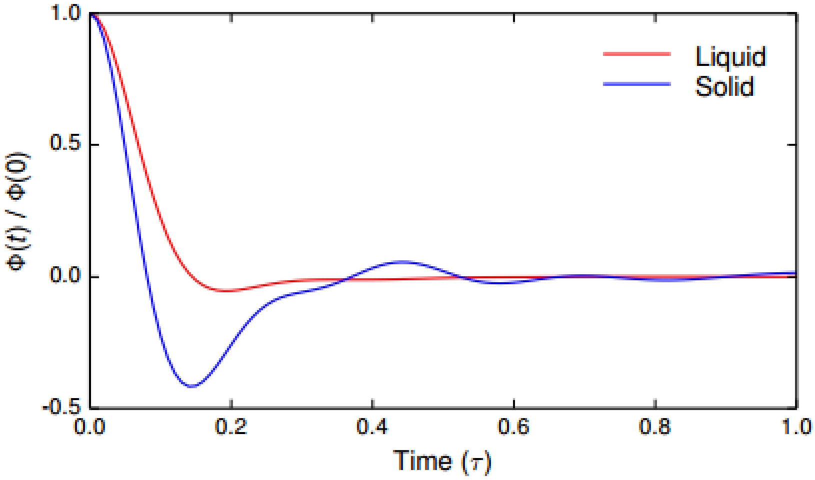

Figure 2. 7 The normalized velocity autocorrelation function.

A dynamical property that can be obtained from the VACF is diffusion coefficient *D*. Provided the VACF decays to zero at long-time, the Green-Kubo relation shows that the integrated area below the VACF plot gives the value of *D*, such that

$$D = \frac{1}{3}\int_0^\infty \langle \mathbf{v}(t)\bullet\mathbf{v}(0)\rangle \, dt \ . \qquad (2.33)$$

The Wiener-Khinchin theorem [52] states that the power spectrum of a dynamic quantity can be obtained through the Fourier transform of its autocorrelation function

$$F(\omega) = \frac{1}{\sqrt{2\pi}} \int_{-\infty}^{\infty} C(t) e^{-i\omega t} dt \ . \qquad (2.34)$$

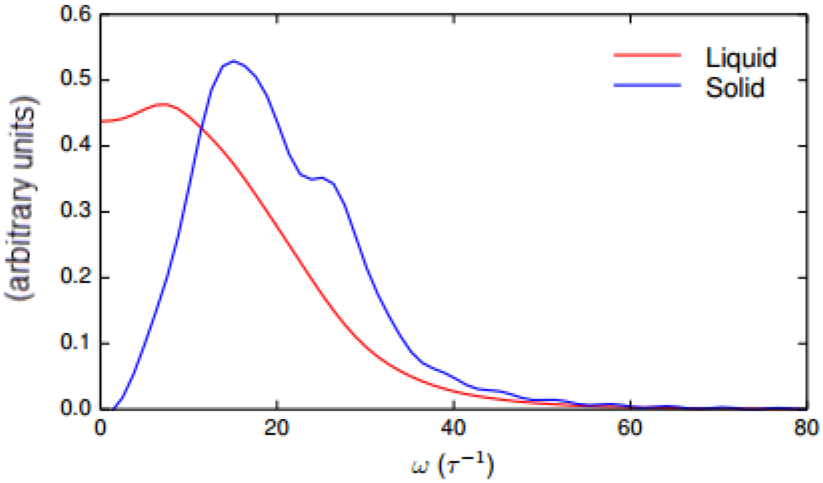

Figure 2. 8 Fourier transform of the velocity autocorrelation function.

For example, one can transform the VACF from coordinate to time domain via a Fourier transformation. The resulting power spectrum $F(\omega)$ in frequency space is simply the vibrational density of states (VDOS) representing the single particle dynamics. For a liquid, the VDOS at zero frequency is non-zero and is proportional to the diffusion coefficient *D* (see Figure 2. 8). The peaks of the VDOS are composed of all the vibrations, including both infrared (IR) and Raman active modes. For a classical system, a Fourier transformation of the autocorrelation of the molecular dipole moment $\langle \mu(t)\mu(0) \rangle$ and the polarizability corresponds to the IR spectra and Raman spectra, respectively. For a solid, the dipole of the unit cell can be computed from the Wannier function method [57, 58]. In essence, it is not possible to assign charges to the atoms in the unit cell of a periodic system. Instead, the electronic distribution of a periodic solid can be computed from the wave functions by projecting them on Wannier centers. The total dipole moment of the unit cell can be computed from the nuclear charges and the associated coordinates of the Wannier centers. The IR spectrum is obtained from the Fourier transform of the dipole moment weighed by a quantum correction factor [59].

An important use of the correlation function in this thesis work is the molecular orientation time function $P_2(t) = \frac{1}{2}\left(\left\langle 3\cos^2\theta(t)\right\rangle - 1\right)$, where $\theta(t)$ is the angle of the directional molecule at time *t* relative to the laboratory frame. The autocorrelation function $\left\langle P_2(t)\cdot P_2(0)\right\rangle$ is used to describe the reorientation dynamics that can be measured from nuclear magnetic resonance (NMR) spectra. The relaxation time τ_0 of the reorientation process can be extracted from a fit to $\left\langle P_2(t)\cdot P_2(0)\right\rangle = Ce^{-t/\tau_0}$ (*C* is a constant), which can be compared directly with results from the NMR measurement.

Mean squared displacement

Another method to analyze the dynamics is to calculate the mean square displacement (MSD) of selected particles in the system. MSD is defined as the square of the average distance a particle has moved from its starting point within the time interval *t*,

$$\mathrm{MSD} = \left\langle \left|\mathbf{r}(t) - \mathbf{r}(0)\right|^2 \right\rangle , \qquad (2.35)$$

where $\langle\cdots\rangle$ denotes an average of starting time origins and **r**(*t*) represents the particle position at time *t*. The MSD contains information on the atomic diffusivity information. As shown in Figure 2. 9, if the system is solid, the diffusion will be negligibly small and the slope of MSD is almost zero. Due to diffusive motions in the equilibrium state, the MSD for a liquid increases linearly with time. According to the Einstein relationship, the slope of MSD is related to the diffusion coefficient *D*,

$$D = \lim_{t\to\infty} \frac{1}{2n_d t} \left\langle \left|\mathbf{r}(t) - \mathbf{r}(0)\right|^2 \right\rangle , \qquad (2.36)$$

where n_d is the dimensionality of the diffusion (*e.g.*, 3 for 3D systems). At an infinite time limit, the *D* value obtained from Eq.(2.36) should be equivalent to that from the Green-Kubo relation given in Eq.(2.33) .

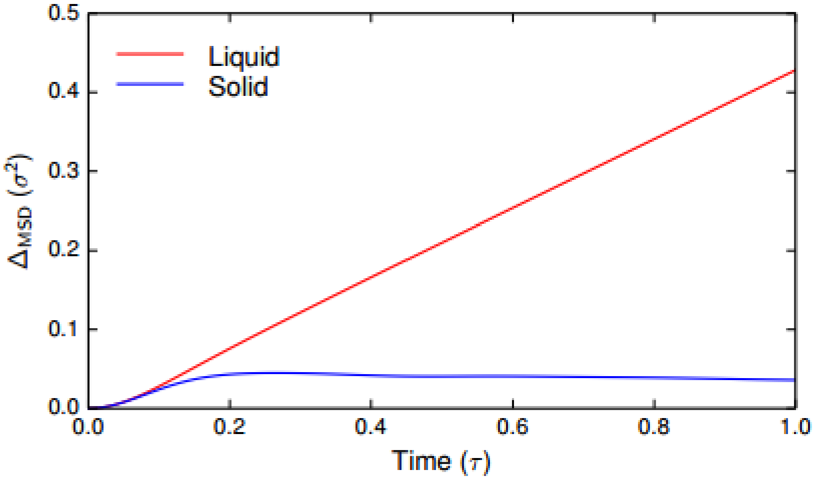

Figure 2. 9 The mean square displacement as a function of time.

2.5 First-principles software

Three first-principles electronic structure codes - *Vienna Ab-initio Simulation Package* (VASP) [60, 61], Quantum-ESPRESSO [62], and CP2K [63] - were used in the thesis research as described in ensuing Chapters 3 and 4.

VASP is a first-principles package based on the DFT theory. It can be used for static electronic calculations and quantum mechanical MD with pseudopotential and plane-wave (PSPW) methods. Born-Oppenheimer MD was implemented in the VASP code. An advantage of the VASP package is that the Blöchl's PAW potential was also implemented [64, 65]. In principle, the PAW potential is an all–electron potential and therefore allows for the calculation of all-electron properties from pseudopotential-based schemes by reconstructing all-electron wave functions from the pseudo wave functions. In general, the PAW method can produce more accurate results than general pseudopotentials. The PAW potential also allows the core orbitals to adjust under extreme pressure. Most static and dynamic calculations in this thesis work were performed with the VASP code (*e.g.*, geometry optimization, electronic property calculations and finite-temperature MD simulations with constant-volume and constant-temperature (NVT) ensembles).

Quantum-ESPRESSO is an integrated suite of first-principles codes for electronic structure calculations and material modeling based on the PSPW approach. While PAW potentials [65], in addition to other pseudopotentials, are also available included, a distinct advantage of the Quantum-ESPRESSO package is that MD calculations in the constant-pressure and constant-temperature (NPT) ensemble can be used. At the time the thesis work was performed, NPT ensemble was not available in the VASP package, so the Quantum-ESPRESSO package was used in the NPT ensembles study for the solid hydrogen project. The recent addition of the NPT algorithms in VASP facilitates the study of the structure and dynamics at high pressure and finite temperatures.

Finally, to calculate the infrared spectra of solid hydrogen, it is essential to evaluate the dipole moments from Wannier centers. For this purpose, the code CP2K [63] was used. CP2K is a pseudopotential code using localized atomic orbitals. The atom-centered localized orbitals facilitate the transformation of the Bloch wave functions to Wannier functions.

CHAPTER 3

STRUCTURE AND DYNAMICS IN CONDENSED MATTERS UNDER PRESSURE

As introduced in Chapter 1, atomic dynamics can play an important role in the intrinsic properties of condensed matters. As will be shown in this chapter, even solids at extremely high pressure are not immune to this phenomenon. Atomic dynamics can strongly affect the structure and properties of materials and pressure is the most sensitive probe to alter dynamics.

Liquids are disordered systems lacking long-range order. The short-range order in a molten matter is usually extended to a few tenths of a nanometer. This local structure is often considered to be analogous to the atomic arrangement of the corresponding solid [2]. However, this assumption is not always valid. An example of this is the long unsolved problem of molten gallium's structure. The presence of a shoulder on the high *q*-side of the main peak in the measured static structure factor $S(q)$ has been the subject of controversy. In the first part of this chapter, we study the structure of liquid gallium (*l*-Ga) using first-principles molecular dynamics (FPMD). Our objectives were to reproduce experimental observations and analyze the temporal structures to decipher the underlying physics of this peculiar $S(q)$ feature. We focus on the pressure effect on the liquid and compare it with available experimental results.

Rotational disorder may exist in some molecular solids. A typical solid with rotational disorder is solid hydrogen. At ambient pressure, H_2 molecules are freely rotating with the molecular centers arranged in an *hcp* lattice [19]. As discussed in Chapter 1, solid hydrogen has a complex phase diagram (*vide supra*). Under compression, solid hydrogen transforms successively into a number of high pressure phases. While the first three phases (I-III) are well-known, a new phase (IV) at high pressure (>220 GPa) and room temperature was recently identified [24, 25]. Due to a lack of structural information, computer simulation has been an effective tool to explore the structure. In the second part of this chapter, results on a study of the structure and atomic dynamics of this new dense hydrogen phase are reported.

3.1 Dynamical structure of liquid gallium at ambient and high pressures

Gallium is a metal known to show several phase transitions as a function of pressure and temperature. The P-T phase diagram is shown in Figure 3. 1 [15]. Similar to ice, an anomalous behaviour where the melting temperature decreases with pressure has been the subject of intense study and speculation. Therefore, it is interesting and relevant to study the structure of *l*-Ga. The structure of *l*-Ga at ambient pressure has been studied extensively by experimental researchers [10-14]. When just above melting temperature, a highly asymmetric first sharp (principal) peak in the static structure factor $S(q)$ with a distinct shoulder at the high-q side is observed. At a very high temperature, the shoulder merges into the principal peak and increases its asymmetry. This feature has been attributed to a non-close-packed liquid structure [66]. In order to explain the features in the $S(q)$, a large number of computer simulations [67-69] have been performed over a wide temperature range at ambient pressure. There are only a few studies concerning pressure effect [15, 70-72]. Moreover, most of the previous calculations on *l*-Ga were performed using empirical potentials. Only two first-principles [69, 73] and one orbital-free [74] MD simulations have been reported. The dynamics of *l*-Ga was studied recently by inelastic x-ray scattering [75] and the results revealed surprising dispersive, transverse acoustic vibrations, showing that the structure cannot be described as a simple hard-sphere liquid.

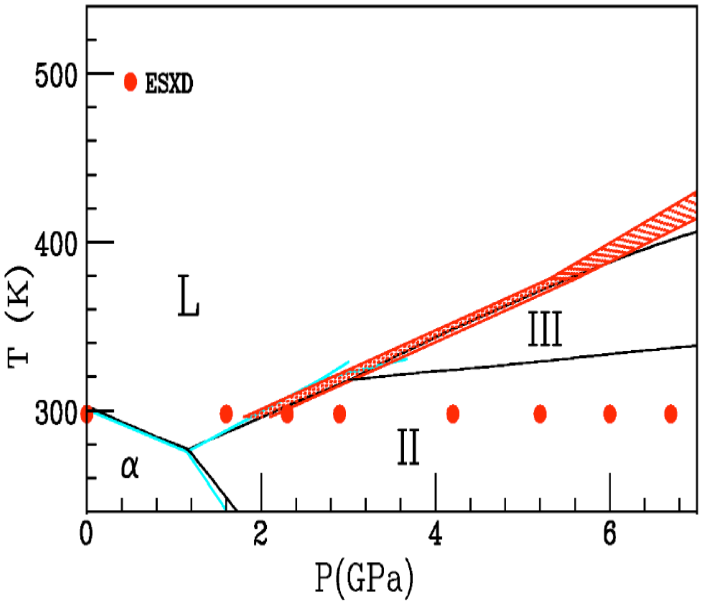

Figure 3. 1 Phase diagram of Ga. Reproduced with permission from Ref.[15].

In spite of extensive experimental and theoretical studies, there is no consensus on the structure of *l*-Ga. An unsettling problem is the origin of the distinct shoulder on the high-*q* side of the principal peak in the $S(q)$. The free-electron model suggests that the anomalous structural features observed in the $S(q)$ of metallic liquids are of purely electronic origin and are the consequence of *Freidel* oscillations in a non-close-pack structure [67]. From classical MD calculations, a structural model invoking the clustering of Ga was proposed [68]. In addition, a first-principles simulation of *l*-Ga at 1000 K [69] found the existence of covalent Ga_2 dimers and attributed the high-*q* shoulder in $S(q)$ to the presence of these dimers. However, the hypothesis that Ga_2 dimers are the origin of the high-*q* shoulder was questioned by Tsai and colleagues [76] with classical MD simulations.

Motivated by the lack of detailed investigations of pressure effect and the inconsistency between different theoretical interpretations about *l*-Ga's structure, we studied this structure near its melting temperature as a function of pressure with FPMD calculations [77]. Both the static and dynamic properties of *l*-Ga at ambient and high pressure were investigated. As will be demonstrated in the ensuing discussion, the observed features in the $S(q)$ and pressure dependency are correctly reproduced. Detailed analysis of MD trajectories found no evidence of the presence of Ga_2 dimers as proposed elsewhere. Through a comparison of the local geometry and electronic properties, the structure *l*-Ga was found to be similar to the underlying crystalline Ga-II and Ga-III solids.

3.1.1 Computational details

The aim of this study was to investigate the effect of compression on the structure and dynamics of *l*-Ga near its melting point. For this purpose, FPMD calculations were performed at pressures of 0, 1.6, 2.5 and 5.8 GPa at 300K with the VASP (*Vienna ab initio simulation package*) code [60, 78] using the Born-Oppenheimer MD method. Electronic structure calculations were performed with a projector augmented wave (PAW) potential [61, 65] in the GGA-PW91 approximation [79]. Electron orbitals were represented by plane-waves with an energy cutoff of 135 eV using a $2\times2\times2$ *k*-point grid [46]. FPMD simulations were performed on a bulk *l*-Ga model containing 128 Ga atoms in a cubic box with periodic boundary conditions. An initial liquid model was obtained by melting the ambient solid structure at 1000 K. The system was then cooled down at a rate of 175 K/ps to achieve the desired liquid state. At each pressure point, the system was first equilibrated for 7 ps. In the micro-canonical ensemble

(NVE), equilibrium was ensured by monitoring the fluctuation of the total energy. This was followed by a production run of 17 ps with the temperature controlled by a Nose-Hoover thermostat [80, 81]. A time step of 1 fs was used in the integration of equations of motion.

Table 3. 1 Comparison of the optimized structures of Ga-I, Ga-II Ga-III with experimental results [82-84] under the same pressure conditions (0 GPa for Ga-I and 2.8 GPa for Ga-II and Ga-III). The cell length (*a*, *b*, *c*) and volume (V) are in unit of Å and Å^3/atom, respectively.

	Cal.				Exp.			
	a	*b*	*c*	V	*a*	*b*	*c*	V
Ga-I	4.5922	7.7574	4.5881	20.43	4.5192	7.6586	4.5258	19.58
Ga-II	5.978	8.670	36.262	18.07	5.976	8.576	35.758	17.62
Ga-III	2.809	2.809	4.586	18.09	2.813	2.813	4.452	17.62

The system size and time span of the present MD simulation are much larger than in previous work [69, 73]. This permits more accurate description of the structural and dynamical properties. The pressure of the system was determined by the average of the calculated pressures for five randomly selected instantaneous configurations during the MD simulation. The error is estimated to be ±0.2 GPa. Under thermodynamic equilibrium conditions of 5.8 GPa and 300 K, Ga should crystallize into a solid [15]. The purpose of the calculation at 5.8 GPa was to investigate if there was any dramatic change in the structural and electronic properties of the meta-stable liquid in the over-pressurized region. The electronic density of states (DOS) was calculated with a denser $8\times8\times8$ *k*-point grid. Prior to MD simulations, the accuracy of the PW91 pseudopotential was examined by calculating the crystalline Ga-I, Ga-II and Ga-III structures. As shown in Table 3. 1, good agreements with experiments [82-84] were found. In addition, the

PBE functional [40] was compared to PW91 on the predicted crystal and electronic structures of solid Ga-I phase and the obtained results are nearly identical.

3.1.2 Results and discussions

To validate the computational parameters, the diffusive behaviour and static structure factor of *l*-Ga at ambient pressure and 300 K were examined first. At 0 GPa, the model system was liquid and exhibited behaviour typical of a linear relationship with the variation of the mean square displacement (MSD) and time. The diffusion coefficient *D* - which is the slope of MSD at long time - was estimated to be 0.160×10^{-4} cm^2/s; this closely matched the experimental value of 0.157×10^{-4} cm^2/s determined under similar thermodynamics conditions (*i.e.*, ambient pressure and 320 K) [85]. Figure 3. 2a shows the computed structure factor $S(q)$ as well as the measured x-ray and neutron diffraction data [11]. The concordance between theoretical and experimental results is remarkably good. Both the positions and heights of the maxima in the $S(q)$ as well as the characteristic shoulder at the high-q side of the first peak are reproduced qualitatively. In addition, the calculated profile of the radial distribution function (RDF) $g(r)$ at pressure of 1.6 GPa was compared with the result obtained from *in-situ* high pressure diffraction performed in a diamond anvil cell at 1.72 GPa [72], as shown in Figure 3. 2b. Apart from a minor discrepancy with the position of the third coordination shell, where the calculation overestimates the maximum by 0.2 Å, the agreement is once again excellent. Although it cannot be completely ruled out that the discrepancy of 0.2 Å on the position of the 3rd peak in the RDF (see Figure 3. 2b) was due to a deficiency in the GGA correction [86], a difference in pressure is the most likely explanation. Since the computed pressure of 1.6 GPa was lower than the experimental 1.72

GPa, the theoretical density should therefore be lower and manifest as a longer 3rd nearest neighbour distance, owing to a less closed-pack structure. The calculated coordination number (CN) of the first shell computed by integrating $g(r)$ to the first minimum was 11.7. This value is comparable to the 10.4 determined experimentally [10, 12]. The good accord between theory and experiment affirms the reliability of the present calculations.

The calculated RDF $g(r)$ at different pressures is compared in Figure 3. 3. For an isotropic monatomic liquid, the distance of the nearest neighbour peak is expected to shorten under uniform compression. In *l*-Ga, however, no appreciable change in shape was found from 0 to 2.5 GPa. The position of the first peak remained fairly constant at ~2.78Å. In comparison, the distances to the second and third nearest-neighbour in the same pressure range were reduced by 0.06 and 0.27 Å, respectively. This observation suggests that atoms in the second and third coordination shells are pressed inward and gradually occupy the interstitial voids to give a denser pack structure. The lack of compressibility in the computed nearest neighbour Ga-Ga distance has been reported in high pressure extended x-ray absorption fine structure (EXAFS) [71] and in-situ x-ray diffraction experiments [72]. Upon further compression to 5.8 GPa, the first Ga-Ga distance decreased by 0.024 Å from 0 GPa (see Figure 3. 3). The calculated CNs were 11.7, 12.1, 12.2 and 12.8 at 0, 1.6, 2.5 and 5.8 GPa, respectively. These values are typical for most metallic liquids [67]. More significantly, the predicted trend was in complete agreement with the measurements by Tsuji and colleagues [70]. The lack of substantial variation of CN in this pressure regime suggests there is no tendency for *l*-Ga to adopt more directional bonding as observed in some simple alkali metal liquids and solids under pressure [87].

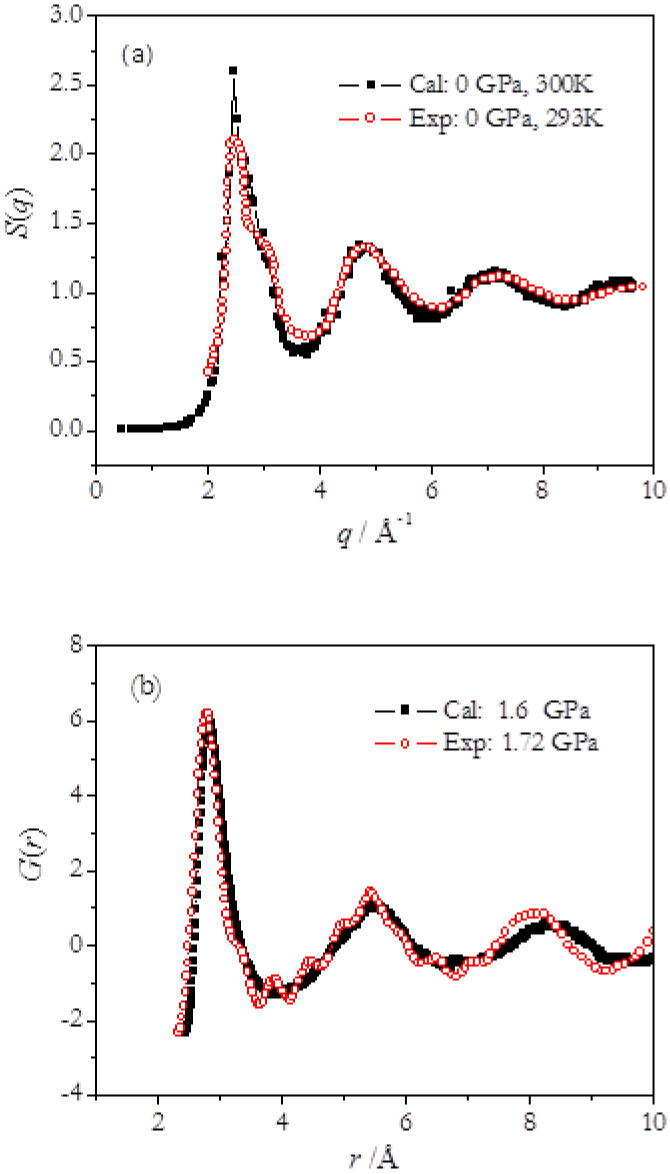

Figure 3. 2 (a) Comparison of static structure factors of our calculated *l*-Ga at 0 GPa and 300K (solid square line)and the experimental result of that at 0 GPa and 293K (hollow circle line) [11]. (b) Comparison of experimental [73] and calculated $G(r)$at 1.72 and 1.6 GPa, respectively. Note $g(r) = \frac{1}{2\pi^2 \rho r} G(r) + 1$ where ρ is the atomic density of the liquid.

The $S(q)$ at different pressures is compared in Figure 3. 4. No significant change in gross profiles was observed below 2.5 GPa. However, in detail, the principal peak became sharper with increasing pressure. Since the first peak of the structure factor for a disordered system [88] is related to the intermediate range structural order, this observation suggests the intermediate ordering of *l*-Ga changes with pressure and becomes more structured. This conclusion is consistent with the analysis of the $g(r)$ presented above, which also revealed structural changes in the second and third coordination shell upon compression.

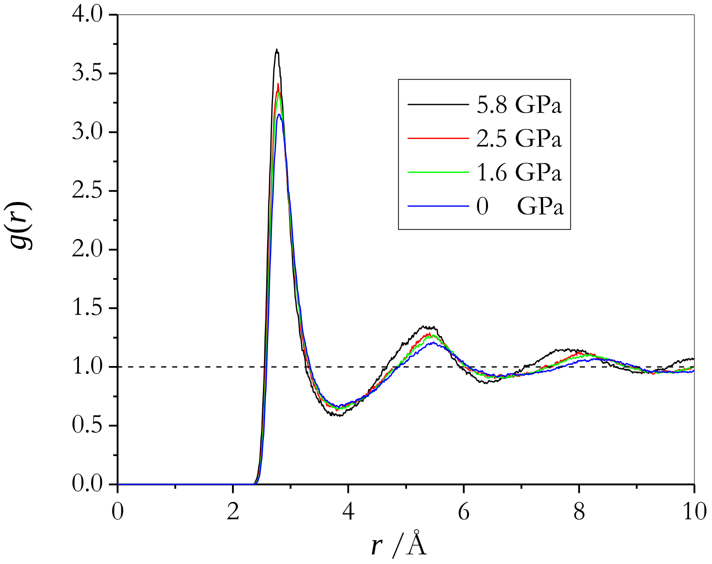

Figure 3. 3 Comparison of radial distribution function $g(r)$ of *l*-Ga near melting temperature at 0, 1.6, 2.5, and 5.8 GPa.

The origin of the high-q shoulder of the first peak of $S(q)$ has long been the subject of debate [68, 69]. Gong and colleagues.[69] attributed the presence of the shoulder to very short-lived covalent dimers – remnants of melted Ga – with a bond length of 2.44 Å. From classical MD calculations, Tsay's group [68] instead postulated that the shoulder structure was due to the formation of clusters in the *l*-Ga. Very recently, Tsai and colleagues [76] re-examined *l*-Ga structure using classical MD simulations and raised objection to the proposal of the presence of covalent Ga_2 dimers [69].

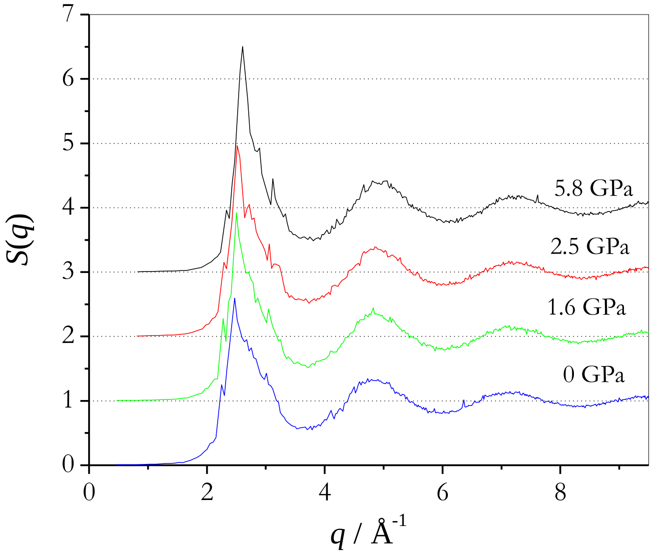

Figure 3. 4 Calculated static structure factor $S(q)$ for *l*-Ga near melting temperature at 0, 1.6, 2.5, and 5.8 GPa.

To examine the postulation about the formation of Ga_2 dimers, the temporal Ga-Ga distances between pairs of atoms were monitored during the MD calculations. Ga-Ga pairs separated by 2.5 Å were only found occasionally with a resident time of less than 0.2 ps. In *α*-Ga, the dimer vibration was found to be 7 THz [89], which corresponded to a vibration period of 0.14 ps. Therefore, no sustainable Ga_2 dimer was found in the liquid. It should be noted that previous FPMD calculations [69] were performed at 1000 K and the lifetime of the proposed Ga_2 dimer was determined to be only 0.05 ps. Therefore, the possibility of covalently bonded dimers in the liquid is very low, if not negligible. Finally, it has been proposed [89] that the shoulder at high-q of $S(q)$ in a metallic liquid is the result of medium-range order beyond the first shell caused by *Friedel* oscillations [67]. As will be shown later, an analysis of local geometry and electronic properties of *l*-Ga supports this explanation.

The local structure of *l*-Ga has been studied using the EXAFS method at the Ga *K*(1s)-edge [15, 16]. In agreement with total diffraction measurements, analysis of the experimental results revealed no discernible change in the first-neighbour distance at 2.76 Å from 0-1.9 GPa [16]. There were, however, small variations in the amplitude of the first peak in the reconstructed *g*(*r*) functions, where the height of the first-neighbour peak increased slightly with pressure from 3.5 at 0.6 GPa to 3.8 at 1.9 GPa [16]. The theoretical calculated heights at 0 and 2.5 GPa were 3.3 and 3.5, respectively (see Figure 3. 3).

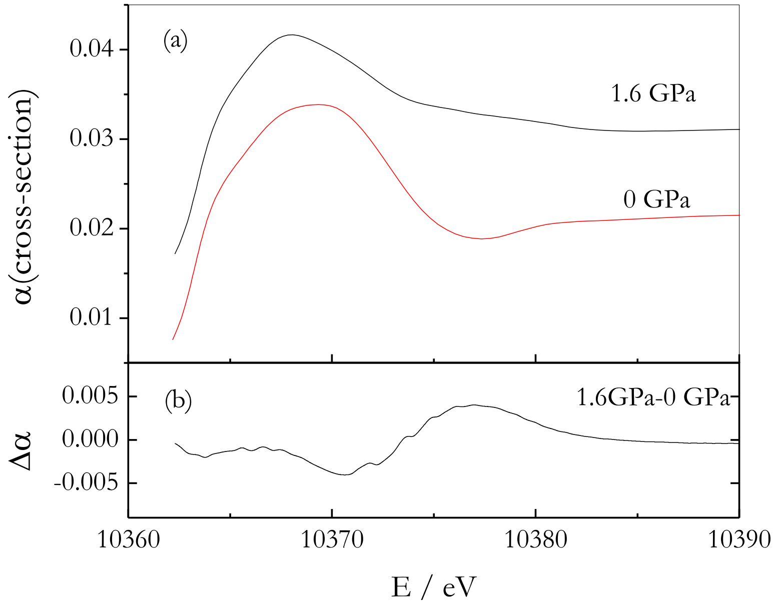

Figure 3. 5 (a) Calculated x-ray absorption spectra (XAS)α of *l*-Ga; (b) Difference of calculated XAS (Δα) spectra between 1.6 and 0 GPa. The XAS spectra in (a) at 1.6 GPa is up-shifted by 0.01.

More recently, fine differences even in the rather monotonous Ga *K*-edge XAS spectra were revealed in a confined droplet of *l*-Ga at high pressure [15]. A shift in the spectral density from the low- to high-energy regions near the ionization threshold was found by taking the difference of the normalized XAS spectra ($\Delta\alpha$) at 1.6 GPa and 0 GPa. A dip (intensity loss) was found at 10.369 keV, which is compensated for by an intensity gain at 10.378 keV. The dip and peak of the XAS difference spectrum were separated by 9 eV. Here, the *K*-edge XAS at 0 and 1.6 GPa was calculated using the multi-scattering method with the FEFF8 code [90], taking into account the core-hole effect. At each pressure, a snapshot from the MD trajectory was selected and the XAS spectrum was averaged from the calculations of 18 randomly selected Ga sites. The theoretical XAS spectra at 0 and 1.6 GPa, as well as the difference spectrum ($\Delta\alpha$), are shown in Figure 3. 5. These calculations reproduced the essential features in the experimental difference spectrum. The predicted energy separation between the dip and the peak of 7 eV is in qualitative agreement with the experiment. The strong accord between the theoretical and experimental features further affirms the reliability of the theoretical liquid model.

To investigate the dynamical behaviour of *l*-Ga, the diffusion coefficient (*D*) was calculated from both the velocity autocorrelation function (VACF) and the MSD. The results from both methods were almost identical. As already stated above, the calculated diffusion coefficient of 0.160×10^{-4} cm^2/s at 0 GPa was comparable to the experimental value of 0.157×10^{-4} cm^2/s [85]. When *l*-Ga was compressed to 1.6 GPa, *D* reduced slightly to 0.123×10^{-4} cm^2/s. It is interesting to note that the diffusion coefficient decreased almost linearly with increasing compression. This observation agrees with a previous study based on a modified embedded-atom model (MEAM) [91]. At 5.8 GPa, in the over-pressurized metastable liquid regime of *l*-Ga, the atomic diffusion slowed and *D* dropped to 0.077×10^{-4} cm^2/s.

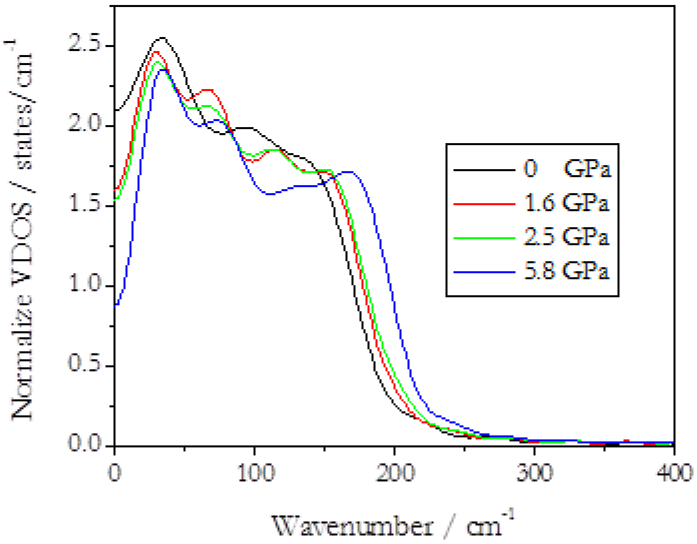

Figure 3. 6 Calculated vibrational density of states (VDOS) of liquid Ga at different pressures.

The dynamical behaviour of *l*-Ga can also be probed from the phonon spectra. The normalized vibrational density of states (VDOS) calculated from the Fourier transform of the VACF at different pressures is shown in Figure 3. 6. The non-vanishing VDOS at zero frequency ($\omega = 0$) is a consequence of the diffusive motions in the liquid. The calculated mean bandwidth of 150 cm^{-1} at 0 GPa is comparable to the measured width of 157 cm^{-1} (19 meV) from an inelastic neutron scattering experiment [92]. The calculated bandwidth increased with pressure and reached 185 cm^{-1} at 5.8 GPa. At 0 GPa, three peaks can be observed in the VDOS. At elevated pressure, four vibrational peaks are predicted. The two low frequency peaks at 40 and 85 cm^{-1} were not very sensitive to pressure. In contrast, the higher frequency peaks at 100 and 145 cm^{-1} at 0 GPa shifted to 150 and 185 cm^{-1}, respectively, at 5.8 GPa. The vibrations in a typical liquid are usually heavily damped and characterized by one featureless broad band. It is tempting to associate the two distinct low frequency peaks in the VDOS of *l*-Ga to the acoustic branches and the two high frequency peaks to the optic branches of the solid. The phonon dispersions of crystalline α- and β-Ga have been measured by neutron inelastic scattering experiments at ambient pressure [89, 93]. α-Ga consists of a pair of Ga_2 dimers in the primitive cell and the stretching frequencies of the dimer were found to lie between 223-247 cm^{-1} (6.7-7.4 THz) [89]. These frequencies are significantly higher than the calculated and observed cutoff frequency of *ca*. 200 cm^{-1} in the VDOS of *l*-Ga at 0 GPa. In comparison, the metastable β-Ga is monoclinic and is built from Ga polyhedra. The highest observed phonon frequency cutoff [93] was 200 cm^{-1}, which is comparable to the calculated VDOS of *l*-Ga at 0 GPa (see Figure 3. 6). Once again, from the comparison of the vibrational frequencies, it is unlikely that *l*-Ga is composed of Ga_2 dimers as speculated previously [69].

From the theoretical evidence and discussions presented above, it is certain that *l*-Ga is not composed of Ga_2 dimers. So what does the local structure of *l*-Ga look like? The clue lies in the analysis of the three-body angular distribution function $g(\theta)$. There was little difference in $g(\theta)$ functions at pressures under 2.5 GPa. The $g(\theta)$ showed a narrow distribution at 55^o and a broader distribution centered around 106^o. The angular distribution is very similar to the high pressure Ga-III phase which is stable above 2.8 GPa and over 319 K as well as the Ga-II phase which is stable between 2-10 GPa at room temperature [16]. The comparison is addressed in Figure 3. 7(a). Ga-III has a body-centered tetragonal structure. At 2.8 GPa and 298 K, a Ga atom is surrounded by 12 nearest neighbours at distances of 2.813 and 2.985 Å [84]. Ga-II has a complex orthorhombic structure consisting of 104 atoms per unit cell [83]. It is a precursor of Ga-III and may be viewed as a distorted body-centered structure. Both Ga-II and Ga-III show angular distribution of the nearest neighbour atoms between $55\text{-}60^o$. The broad distribution ("hump") in *l*-Ga, with the width extending from 80^o to 140^o and centered at 106^o, visually

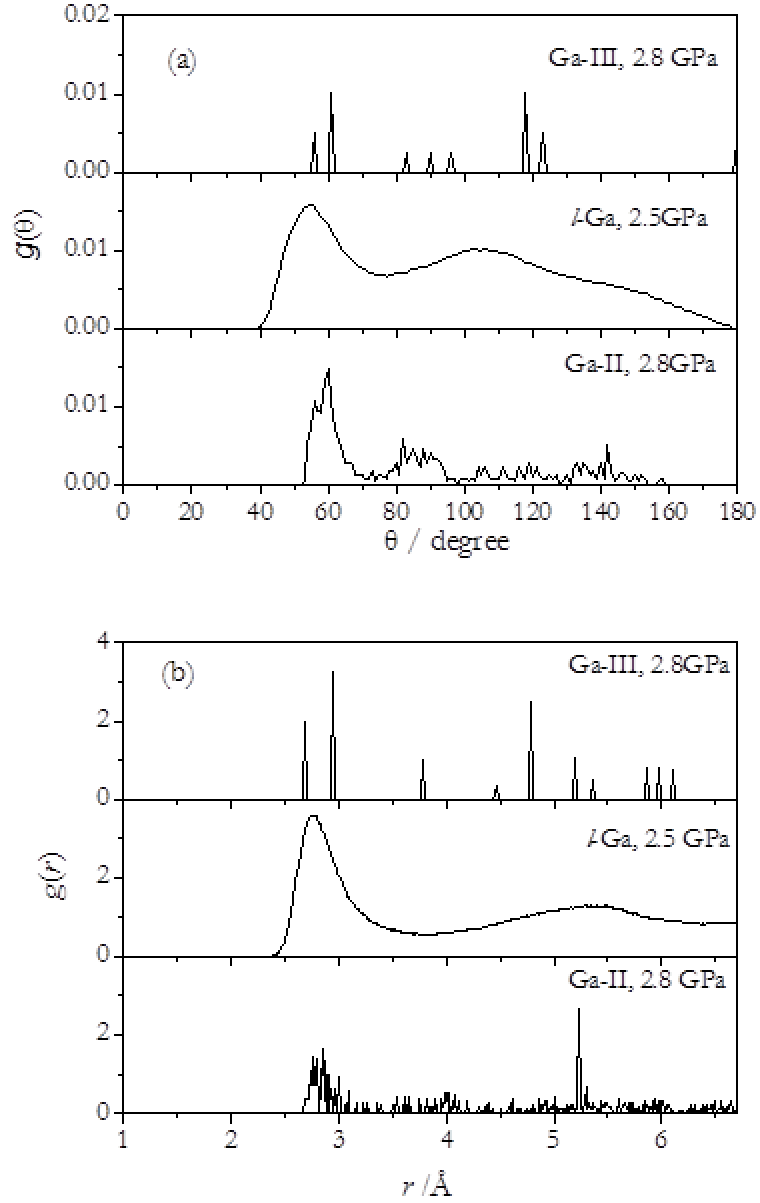

Figure 3. 7 Comparison of the calculated (a) angular distribution function $g(\theta)$ and (b) radial distribution function $g(r)$ of *l*-Ga at 2.5 GPa with those of experimental crystalline Ga-II and Ga-III.

resembles Ga-III more than Ga-II. Stimulated by the revealing comparison in $g(\theta)$ functions shown in Figure 3. 7(a), the $g(r)$ functions of crystalline Ga-II and Ga-III are also computed and compared with *l*-Ga in Figure 3. 7(b). Owing to the complex Ga-II structure, the $g(r)$ showed a quasi-continuous distribution with the nearest neighbour distance extending from 2.65 to 3.10 Å. Incidentally, this distribution resembles the broad first peak in the *g*(*r*) of *l*-Ga. In addition, the sharp distribution at *ca*. 5.2 Å is close to the center of the broad band at 5.5 Å in *l*-Ga. Ga-III has a much simpler crystal structure. As already discussed above, the two first nearest Ga-Ga distances fall into the first peak range of *l*-Ga. The longer range order in *l*-Ga did not compare well with Ga-II. Nevertheless, complete agreement between the liquid and crystalline solid was not anticipated. A comparison of $g(\theta)$ and *g*(*r*) functions, however, allows one to conclude with confidence that the structure of *l*-Ga is closer to the underlying high pressure crystalline Ga-II or Ga-III phase.

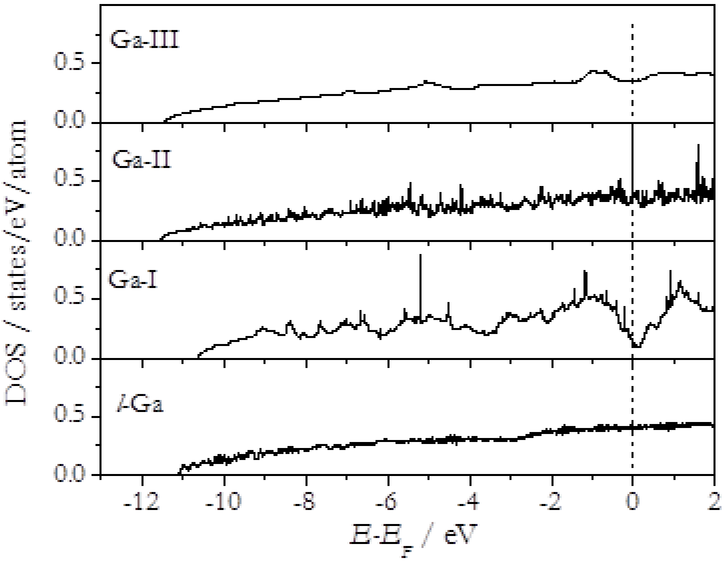

Figure 3. 8 Comparison of the total density of states for *l*-Ga and solid Ga-I, Ga-II and Ga-III.

Finally, the electronic density of states (DOS) for *l*-Ga was investigated. The DOS is not very sensitive to pressure and only the results at 0 GPa will be discussed in detail. The total DOS

(TDOS) for *l*-Ga at 0 GPa is compared with crystalline Ga-I (α-Ga), Ga-II and Ga-III in Figure 3. 8. The TDOS profile of *l*-Ga is typical of a free electron metal (*i.e.*, TDOS $\propto (E-E_f)^{1/2}$, where E_f is the Fermi energy). In comparison, the TDOS of *l*-Ga is very similar to that of Ga-II and Ga-III, both of which also have a free-electron like DOS distributions but are distinct from Ga-I. This is not surprising because the Ga-I structure consists of Ga_2 dimers and the electrons are localized in covalent bonds. The proximity of Ga-III to the melting line [15] lends support to the proposal that the liquid structure is akin to the distorted crystalline structure. The free-electron like electronic property of metallic liquid at ambient pressure has been studied previously [67, 73]. The present results re-affirm this description of the electronic structure but also address the similarity in electronic structure of liquid Ga and solid Ga-II and Ga-III.

3.1.3 Conclusions

FPMD calculations were performed at ambient pressures and medium pressures up to 5.8 GPa to investigate the structure of *l*-Ga near its melting point. It was shown that the first peak in the structure factor $S(q)$ became sharper with compression. Consistent with past experiments, the first nearest neighbour Ga-Ga distance showed no noticeable change below 2.5 GPa, whereas the distances to the second and third shells reduced. There was no evidence of substantial structural changes within the pressure range studied. Detailed analysis of the static and dynamical property compression trends showed that the proposal for the existence of Ga_2 dimers on the local structure of *l*-Ga was not valid. The instantaneous Ga-Ga contact within the range of a covalent bond has a very short lifetime. Furthermore, no signal of Ga_2 dimer vibrational mode was found in the experimental nor the calculated VDOS spectra of *l*-Ga. In fact, the three-body angular distribution and radial distribution functions as well as the electronic structures showed the liquid structure to be very similar to the underlying high pressure crystalline Ga-II or Ga-III. This "crystalline-like" liquid structure is manifested in the dispersive transverse acoustic vibrations revealed in a recent report [75]. The results of the present theoretical analysis are consistent with two previous experimental investigations showing that the structure of *l*-Ga cannot be described by the existence of "molecular pairs" or any molecular clustering [94, 95].

3.2 Structure and dynamics of dense hydrogen

The metallization of dense hydrogen is a central topic in high pressure physics. In 1935, Wigner and Huntington predicted that solid molecular hydrogen would transform into a monoatomic metallic state at sufficiently high pressure [26]. Later, the metallic phase was predicted to exhibit exotic properties such as high temperature superconductivity [27] and quantum fluidity [96]. Therefore, the search for metallic hydrogen is the Holy Grail in high pressure physics. While metallization has not yet been found, a rich phase diagram of dense hydrogen has emerged through both experimental and theoretical investigations [25]. This complex phase diagram of hydrogen under extreme pressures with an emphasis on experimental progress has been reviewed by Goncharov *et al.* [18]. A complementary discussion on theoretical progress was published as well [5].

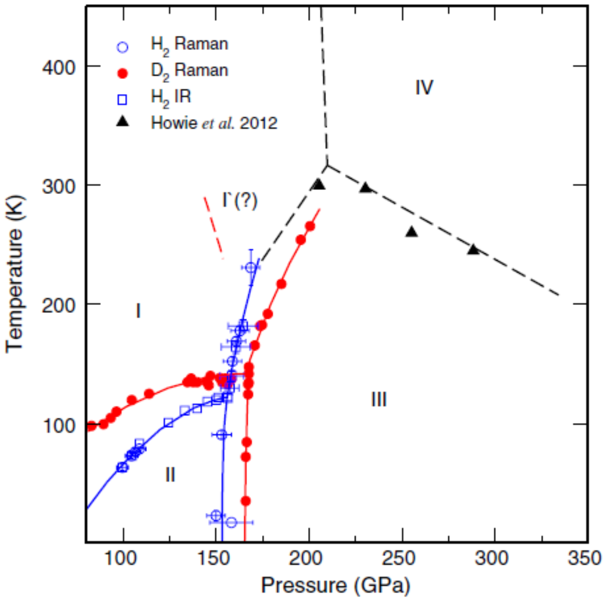

Figure 3. 9 High-pressure phase diagram of solid molecular hydrogen from experimental measurements. Reproduced from Ref.[5].

The phase diagram of solid hydrogen up to 300 GPa in Figure 3.9 shows the existence of at least four solid molecular phases [5]. The three low-temperature phases established experimentally are labeled phases I, II and III. At low pressures, intermolecular interactions between hydrogen molecules are weak and therefore hydrogen molecules can rotate freely (quantum rotors) about their center of mass that crystallize into an *hcp* lattice (phase-I) [20]. As the pressure increases and temperatures remain below 140 K, the rotational symmetry of phase-I is broken and the solid hydrogen transforms to phase-II. The phase transition boundary is dependent on temperature. The transition occurs at ~110 GPa and 8 K in H_2 [97]. This is followed by a transition to phase-III at 150 GPa. This transition is signified by a strong enhancement in the infrared (IR) vibron absorption intensity [22]. Recent synchrotron IR and optical absorption measurements suggest that phase-III is an insulator and stable up to at least 360 GPa over a broad temperature range [98]. In both phases II and III, the H_2 molecules are believed to be partially or completely frozen into orientationally-ordered structures. The molecular orientations, however, cannot be identified experimentally due to limitations with small sample size and low x-ray scattering efficiency of hydrogen atoms proportional to the atomic number squared [5]. Several theoretical studies have predicted the structures for phases II and III [5]. No consensus has been reached, but it is generally agreed that phase-III is an insulator and that H_2 molecules are orientationally ordered [99].

In late 2011, a report surfaced claiming that metallization was observed at 260 GPa and 300 K [53]. In a subsequent study with Raman and visible transmission spectroscopy, researchers found that when phase-III was warm compressed at room temperature (~300 K) to 220 GPa, it transformed to a new phase-IV of solid hydrogen [25]. Raman spectra of the vibrons further suggested that there are two distinct local H_2 environments in the structure [3]. More recent work showed that phase-IV is still an insulator and that the early claim of metallization is possibly incorrect. Nevertheless, this provides additional evidence for the existence of the new phase-IV.

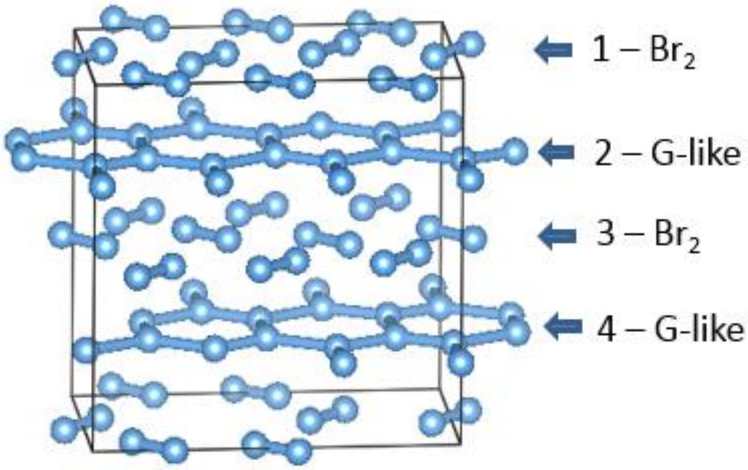

Figure 3. 10 Proposed structure of phase-IV of hydrogen with two distinct layers, *i.e.*, Br_2- and Graphene (G)-like.

A number of structural candidates have been proposed for the phase-IV from theoretical searches for the lowest enthalpy structures, including zero point vibration corrections [23, 28, 100]. Common to these predicted structures is the presence of two distinct structural components: a “molecular” (Br_2- like) layer and a graphene-like (G-) layer (see Figure 3. 10) stacked in an alternating A-B-A’-B sequence. However, the symmetry and exact structure of the G-layer, which consists of elongated and weakly-bonded H_2 molecules, remains a matter of debate. Static calculations (*i.e.*, at 0 K) indicate that the *Pbcn* structure [23], which consists of 3 kinds of hexagonal rings, is dynamically unstable because the lowest frequency libron $(H_2)_3$ ring mode has an imaginary frequency. Two very similar structures - Pc [100] and Cc [28],- have also been suggested as they have slightly lower enthalpy and show no imaginary frequencies.

Raman measurements of phase-IV show a dramatic softening of the G-layer vibron mode with pressure [25]. This is consistent with theoretical calculations [100] wherein the H-H distance in the H_2 molecules is elongated and the intermolecular interaction is weak. Therefore, it is anticipated that the H_2 in the G-layers may transform to a truly graphene pattern with symmetric hydrogen bonds [20], leading to a *Ibam* space group [100]. On the other hand, a *Cmca*-4 structure with four molecules per unit cell [23, 101] was found to be energetically favourable above 225 GPa [100, 102]. Metadynamics simulations [28] also showed the transition from phase-IV to the *Cmca*-4 structure at 275 GPa, which has been speculated to be the atomic metallic hydrogen structure reported in an earlier study [24]. However, the proposed band gap closure [24] disagrees with recent optical data [25]. So far, there is no conclusive structure for phase-IV.

As most structural predictions have been based on static geometry optimization, there is uncertainty surrounding whether the predicted structures may exist at ~300 K, where most experiments are performed. In this work, we examined the structure of phase-IV with FPMD calculations where the temperature effect is explicitly included. As will be shown below, we found that H_2 molecular fragments are fragile and exhibit large amplitude fluxional atomic motions including frequent molecular rotations and intermolecular atomic fluctuations, with intralayer H_2 rearrangements at temperatures between 250 and 300 K. This observation raised the question of whether or not the structure of phase-IV can be described simply by a unique space group. The theoretical finding, however, is substantiated by experimental observations of significant quantum effects in molecular vibrations and librations in the G-layer. The MD results show phase-IV will transform to the metallic *Cmca*-4 structure at 370 GPa, where the distinction between the Br_2-like and G-layers vanishes and large atomic motions ceases.

3.2.1 Theoretical methodology details

Constant pressure - constant temperature (NPT) ensemble classical molecular dynamics calculations were performed with the PAW potential in conjunction with a plane-wave basis set (kinetic energy cutoff of 80 Ry)The PBE functional was employed. The quality of the PAW potential has been checked against all electron calculations to guarantee results are valid within the pressure range studied in this work. A $1\times1\times2$ *Pbcn* [23] supercell with 48 atoms was used as the initial structure. The Brillouin zone (BZ) was sampled with a $4\times4\times4$ *k*-grid [46]. All MD simulations were performed with the Quantum-ESPRESSO code [62]. The structural optimization and electronic structure calculations of the *Cmca*-4 phase were carried out with VASP [60, 61], where the PAW potential with the PBE functional was employed with an energy cutoff of 875 eV for the plane-wave basis set and a *k*-mesh of $6\times4\times4$ for sampling the BZ.

We performed MD calculations for phase-IV of hydrogen at 250 – 370 GPa and 250 - 300 K. Thermodynamic equilibrium was usually achieved in the first 6 ps. The length of the simulation varied from 20 ps at both 250 and 370 GPa to 87 ps at 300 GPa. The maximum deviation during the MD calculations was less than 0.4 meV/atom in the internal energy and the pressure was within 2% of the target. The results of the simulations should be at least qualitatively correct since the ratio of the mean atomic distance $(V/N)^{1/3}$ and the thermal de Broglie wavelength were slightly larger than 1 for the density range [103] studied. Since the quantum effect normally enhances delocalization of the hydrogen spatial distribution, it was expected that the quantum zero-point motions would not fundamentally alter the classical results at relatively high temperatures (*ca*. 300 K), which tends to show hopping and molecular rearrangement processes [104].

3.2.2 Fluxional structure of phase-IV

All MD simulations were performed with an initial *Pbcn* structure. Figure 3. 11 summarizes results of the MD trajectory analyses for two dissimilar planes originating from the *Pbcn* structure. H atoms are colour coded to differentiate individual H atoms on each layer. Same colour dots represent the trajectory of a certain H atom across the simulation time.

As seen in the leftmost columns of Figure 3. 11, at 250 GPa the Br_2-like layers consist of a hexagonal lattice of round “clouds”, each composed of two H atoms, corresponding to the nearly free rotation of H_2 molecules about the center of their bonds. At the same time, the intramolecular bond lengths (0.72 Å) are well maintained as characteristic of “free” molecules. The disordered, rotational motion of H_2 molecules in this layer resembles that of free rotors observed in phase-I [20]. In contrast, the G-layers can be represented as an almost equally populated honey-comb lattice. One does not see any difference in the dimensions or shape of the constituting hexagons, which is expected for *Pbcn* [23] and *Pc* [100] structures. Further inspection employed the colour codes method to trace the atomic motion. The same coloured dots represent the trajectory from the same H atom, therefore the change in colour on crystal sites of G-layer would correspond to the H transfer or collaborative hopping of the H atoms. At 250 GPa (see Figure 3. 11), within our simulation time (~20 ps), the site-to-site H transfer can be identified from the G-layers, where an average frequency of hopping is *ca.* 1 jump every 4 ps.

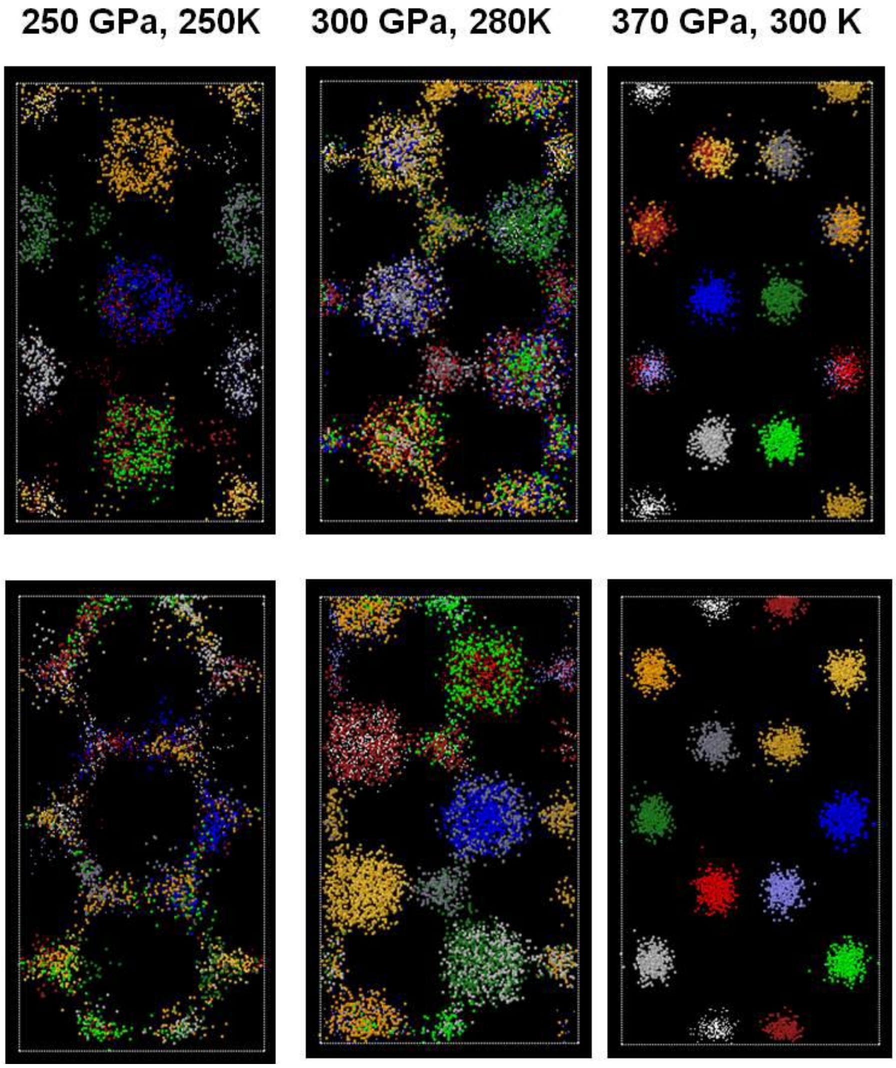

Figure 3. 11 Molecular dynamics trajectories of the two distinct layers from *Pbcn* structure for different pressures near room temperature. The top row corresponds to the Br_2 like layer, while the bottom row to the G-layer. Different colours correspond to different atoms.

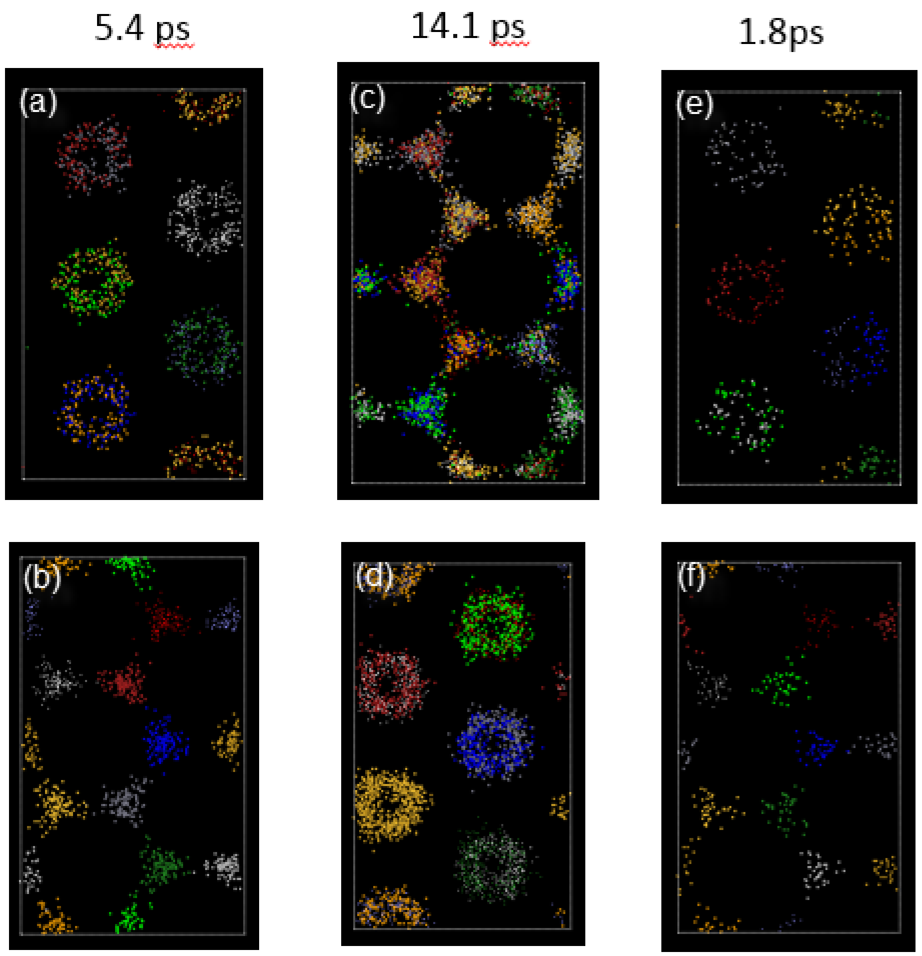

Figure 3. 12 Split trajectories on the two distinct layers of hydrogen at 300 GPa and 280 K. (a), (c) and (e) represent the consecutive structural change within one layer, and (b), (d) and (f) represent the consecutive structural change within the other layer with the same time span.

As seen in the central columns of Figure 3. 11, at 300 GPa the average time difference in the distribution of H atoms between the Br$_2$- and G-layers seems to disappear. Both layers show a honeycomb structure superimposed by an increased number of “clouds,” the result of molecular rotations. Closer analysis of the MD trajectories revealed a synchronized intralayer atomic fluctuation where the molecular-like Br$_2$-layers and the atomic-like G-layers interchanged. This process is clearly identifiable when the trajectory is split into a series of time slices, as shown in Figure 3. 12. It can be seen from the upper panels of the plot that the atomic arrangements in this layer started from the molecular Br_2-layer structure and sustained for a time period of 5.4 ps (see (a)). The structure then changed abruptly to the G-layer arrangement (see (c)). After a span of 14.1 ps, it changed back to Br_2-layer structure (see (e)). As expected, the atomic arrangements of the other layers (see the lower panels (b), (d) and (f) of Figure 3. 12) concomitantly oscillated from the G- to Br_2- and then back to G-layer. Longer time simulations confirmed the continual structural alternation between Br_2- and G- layer arrangements. It is noted that the structural change occured in both layers simultaneously. This indicates that at any given time the crystal structure of hydrogen at 300 GPa and 280 K is always composed of Br_2- and G-layers. This is consistent with the static structure predicted for phase-IV [23, 100]. However, the simulation showed that the structure is not static but is, in fact, dynamic. It should be emphasized that no H transfer was found between the two distinctive layers.

As seen in Figure 3. 11, we already observed H transfers within the G-layer at 250 GPa by identifying the different colour codes for the individual atomic trajectories. This novel phenomenon is magnified at 300 GPa and appears in Figure 3. 12(c) as a significant spread of the same coloured dots over a large range of lattice sites. The H transfer mechanism was examined further by dividing the trajectory (see Figure 3. 12(c)) into five shorter time slices (see Figure 3. 13) of several picoseconds. Within each given time slice, with the exception of the middle panel where some H atoms – indicated by yellow arrows - are moving too fast, the atomic arrangement is unchanged. H transfers occurred between two consecutive time slices with the H atoms moving in the directions shown by the yellow arrows. Figure 3. 13 highlights the fact that H atoms are very fluxional and can transfer to their nearest neighbouring lattice site within a few picoseconds or less. Occasionally, as shown in the middle panel of Figure 3. 13, the proton transfer process is nearly continuous. More intriguingly, the collaborative H transfer led to "pseudo"-rotations of the hexagons in the G-layer.

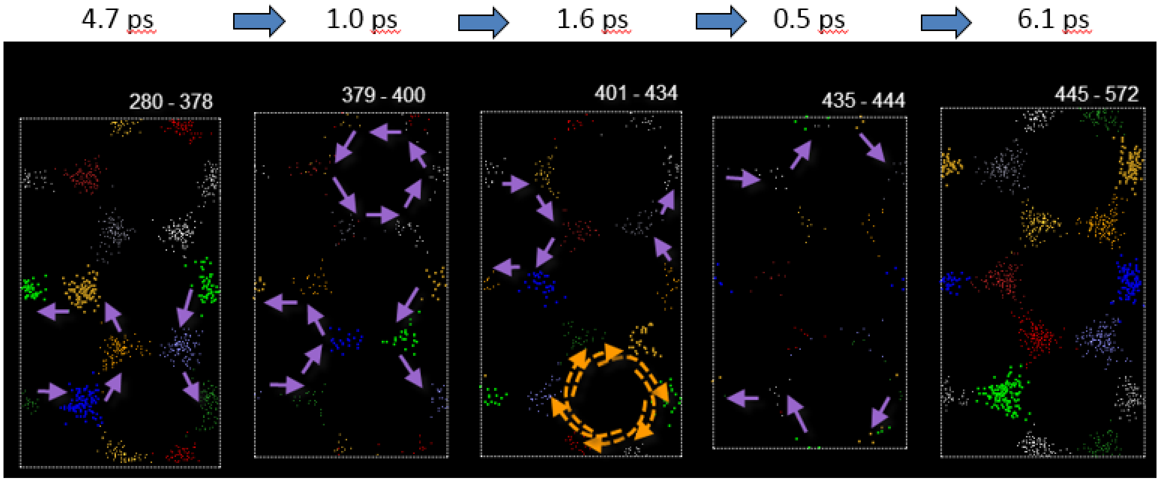

Figure 3. 13 Intralayer H transfer within G-layer shown with five continuous time spans of trajectories. Arrows represent the moving directions of the H atoms to enter into the configuration as appears in the next time span.

The H transfer phenomenon may be explained by pressure-induced changes in the H-H distances within the hexagons of the G-layer, as shown in Figure 3. 14. In the top plot of this figure, at 250 GPa three molecules are identified with intra-molecular bond lengths (from a, c, e contacts) of ~0.80 Å and are loosely bonded with a longer H-H distance (from b, d, f contacts) of ~1.10 Å. This hexagonal geometry is quite stable over the simulation time at 250 GPa but becomes brittle when the pressure increased to 300 GPa. This is seen on the bottom plot of Figure 3. 14. At 300 GPa, the intra-molecular bonds (a, c, e contacts) are stretched so that the they become weak, leading to a shorter H_2 molecule lifetime. The H atom in the hexagon can bond with the nearest neighbour to either the left or the right and temporarily form a molecule.

The rapid H motions reduce the molecular character of the G-layer and lead to the "pseudo"-rotation of the hexagonal rings.

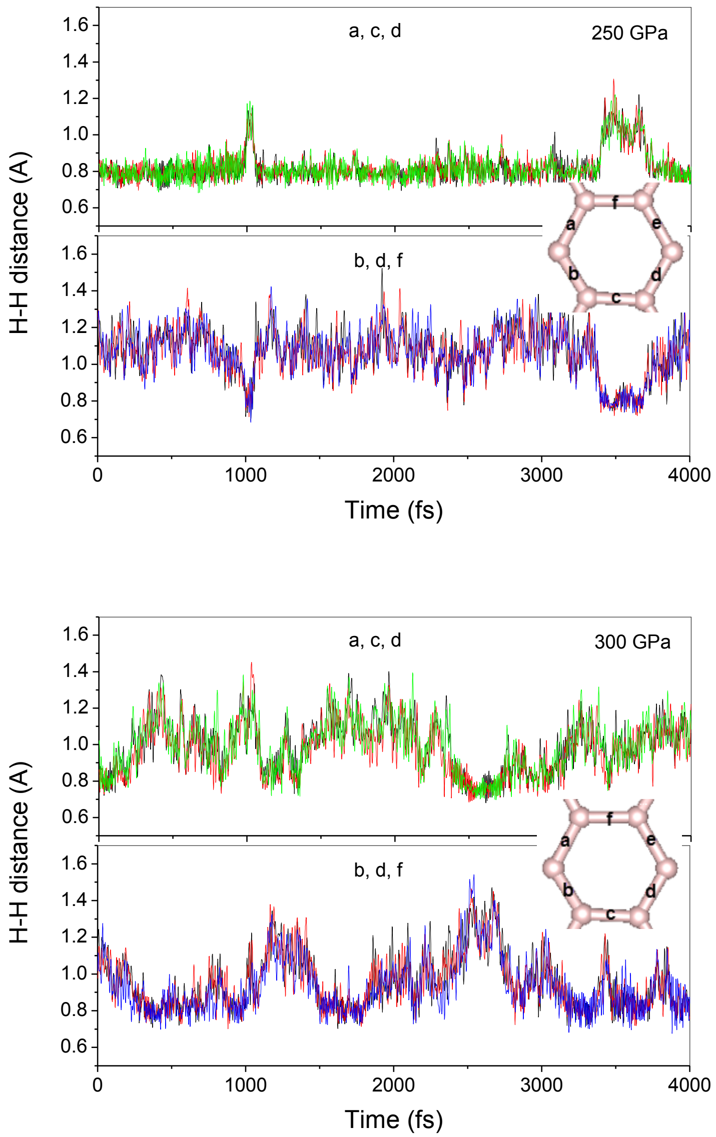

Figure 3. 14 The H-H distances between two neighbouring atoms within the hexagon from the G-layer. Top and bottom plots are for 250 and 300 GPa, respectively.

Upon completion of this study, we were notified of a publication reporting similar dynamical properties of phase-IV [105]. Rotation of the H_2 molecules in Br_2 layer and H transfer in the G-layer was reported, however, the interlayer structural fluctuation was not observed [64]. This discrepancy may arise from the relatively short simulation time (~10 ps) in this reference study compared to the present thesis work (over 90 ps). Our calculations showed that the interlayer fluctuation was a rare event and the structure may remain "stationary" for a period of up to 14.1 ps (see Figure 3.12).

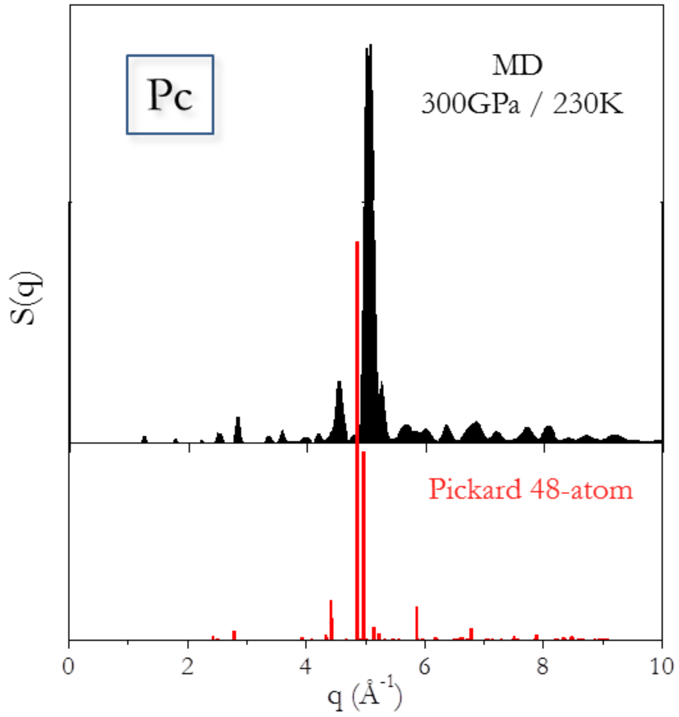

Figure 3. 15 Comparison of diffraction pattern calculated from the MD trajectory with the static *Pc* structure as reported in Ref. [23].

The large atomic fluctuations observed in the MD runs at 250 and 300 GPa showed that the conventional static structure representation of phase-IV as an ideal crystal lattice may not be appropriate. The diffraction pattern ($S(q)$), however, can be calculated directly from the trajectory, as shown in Figure 3. 15. The time averaged structure is consistent with the predicted "static" *Pc* structure [23].

3.2.3 Transition to the metallic *Cmca*-4 phase

To examine how the dynamical structure observed in phase-IV at 250 and 300 GPa would develop in a higher pressure range, we continued the MD simulation of phase-IV at 300 K and raised the pressure to 370 GPa. The calculations revealed a spontaneous transition to another structure. As shown in the rightmost columns of Figure 3. 11, the amplitudes of the atomic motions became much smaller and the layers were crystallographically equivalent. An approximate structure was obtained by taking the average of the instantaneous atomic positions. Geometry optimization led to the *Cmca*-4 structure as proposed previously [23, 101]. The structure is still molecular and consisted of crystallographically equivalent molecules with H-H bond length of 0.776 Å (see Figure 3. 16).

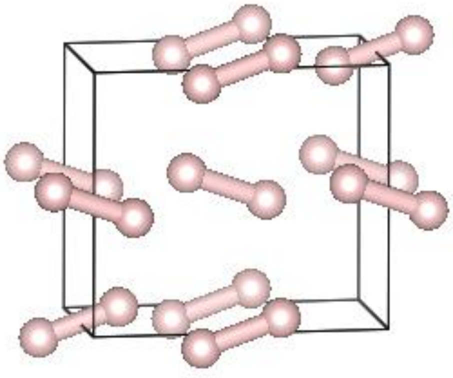

Figure 3. 16 Crystal structure of solid hydrogen in *Cmca*-4 phase.

The calculated electronic structure showed that the *Cmca*-4 phase is metallic. The charge density plot (Figure 3. 17) shows that electron density is partially pushed out from the intramolecular bond to interstitial space. The electron density topology is not unlike those reported previously for light elements under extreme pressure [106].

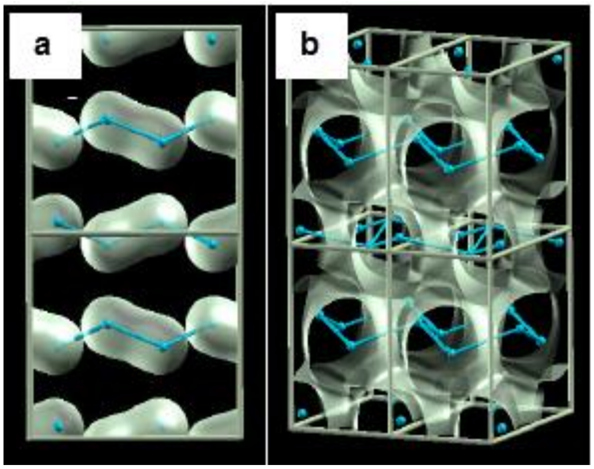

Figure 3. 17 Charge density isosurfaces for the *Cmca*-4 metallic phase at the contour values of (a) 1.0 e/Å^3 showing the persistence of H-H molecules, and (b) 0.5 e/Å^3 illustrating the presence of interstitial electron density.

3.2.4 Vibrational properties of phases-IV and *Cmca*-4

To compare with experimental vibrational spectra, single atom power spectra were calculated from the Fourier transform of the hydrogen atom VACF. The power spectrum contained both IR and Raman active modes. Owing to the fluxional (disordered) nature of phase-IV, there is no well-defined symmetry and so the Raman spectra should comprise all vibrations. As a first approximation, the power pattern is a good representation of the Raman spectrum. The power spectra for hydrogen phases-IV (the top two panels) and *Cmca*-4 (the bottom panel) are compared in Figure 3. 18. At 250 GPa and 250 K, there were two broad vibrational branches at ~ 4500 cm^{-1} and ~ 3600 cm^{-1}. When the system was compressed to 300 GPa at 280 K, the high frequency branch remained largely unchanged while the lower frequency branch shifted to a lower frequency at ~3100 cm^{-1}.

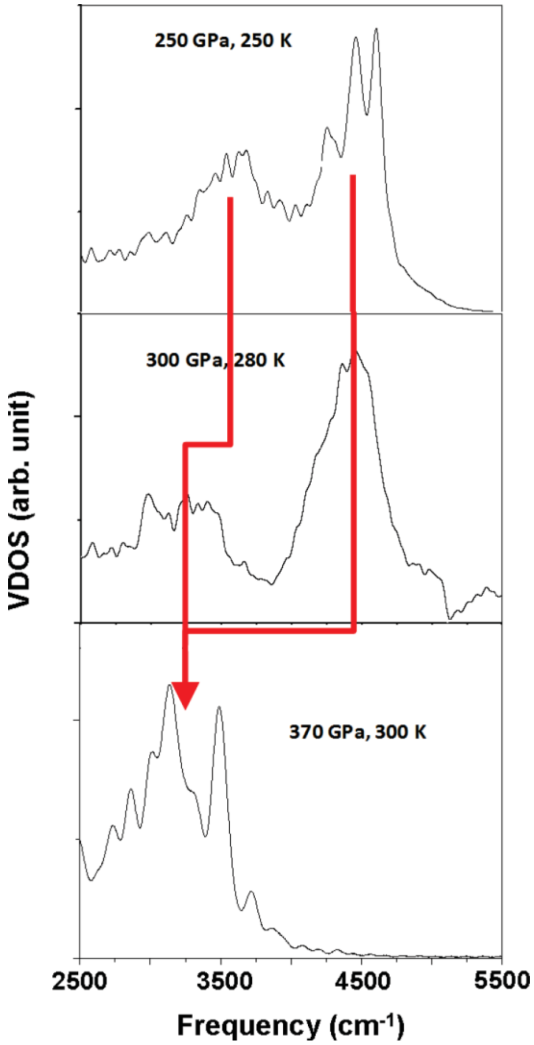

Figure 3. 18 Power spectra for hydrogen at different conditions.

The change in features in the vibrational spectra can be explained by the structure of phase-IV. The higher frequency branch at ~ 4500 cm^{-1} arose from the nearly free rotating H_2 molecules in the Br_2-layer. The lower frequency branch at ~ 3600 cm^{-1} can be attributed to the H_2 vibron of the elongated molecules in the G-layer. At higher pressures, the molecule bond length from the Br_2-layer remained nearly unchanged (0.72 Å). In contrast, H_2 vibration in the G-layer became weaker. This interpretation is consistent with the experimental Raman spectra obtained by our collaborators. This is shown in Figure 3. 19 where the two distinct vibrational bands disappeared at the highest pressure (316 GPa) and the vibrons band merged into a single set of modes at ~3100 cm^{-1}.

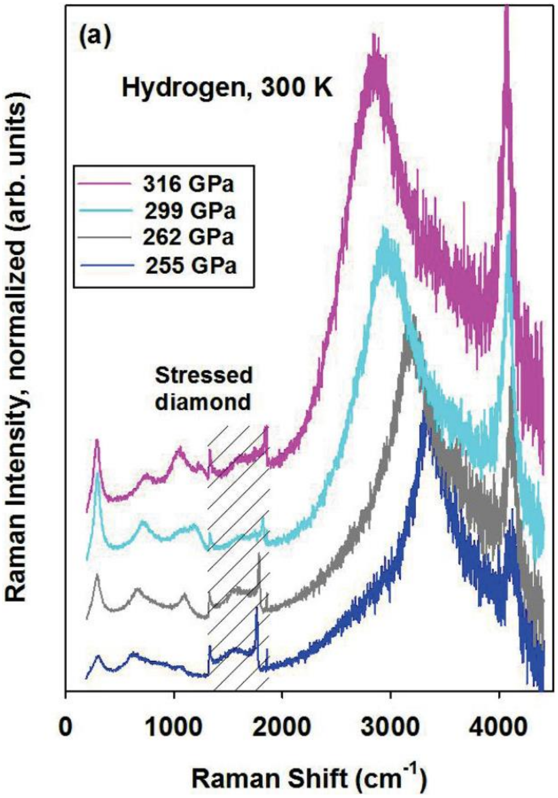

Figure 3. 19 Raman spectra of solid hydrogen with pressure. (Reproduced with the permission from Ref.[107])

3.2.5 Structures and structural transformations of solid hydrogen at low pressure

Following the successful FPMD study on phase-IV, we revisited the structures of solid hydrogen in the low pressure region, as there is very limited information concerning the phase transitions between phases I, II and III. As mentioned earlier, phase-I is a crystal consisting of rotating H_2 molecules where the center of the molecules is arranged in an *hcp* lattice. Details on the structures and molecular orientations in phase-II and III, however, are still not well characterized. While the information on the structure and phase transitions from x-ray diffraction experiments is very restricted [21], valuable but indirect structural information was obtained from IR, Raman and optical measurements [99]. One key experimental observation was that upon passing from phase-I to II, the frequency of the roton mode underwent substantial changes, indicating that the molecules changed from a rotationally free state to more restricted librations (rotational oscillations) [97]. Moreover, the IR activity increased dramatically at the phase-II to III transition and the IR and Raman vibron frequencies softened by about 80 cm^{-1} [99, 108]. We employed FPMD simulations to model the dynamic processes that occurred in solid hydrogen at a pressure range of 25-160 GPa at ~245 K. IR spectra in particular was computed in order to compare with available IR results obtained at a similar pressure and temperature (~300 K) range [109].

A starting model at 25 GPa was constructed from the experimental hexagonal structure but was represented in an orthorhombic cell consisting of 48 hydrogen molecules with random orientations. At each pressure, an NPT MD at 245 K lasting about 10 ps (time step of 1 fs) was performed using Quantum-ESPRESSO code [62]. The cell constants were then computed by averaging cell fluctuations. Using the averaged cell constants, a second set of NVT calculations was performed using the CP2K code [63]. During the course of these MD calculations, the electronic wave functions were transformed into Wannier centers. This facilitated the calculation of the instantaneous dipole moment of the simulation cell. As presented in Chapter 2, the IR spectrum can be computed from the Fourier transform of the dipole moment time autocorrelation function.

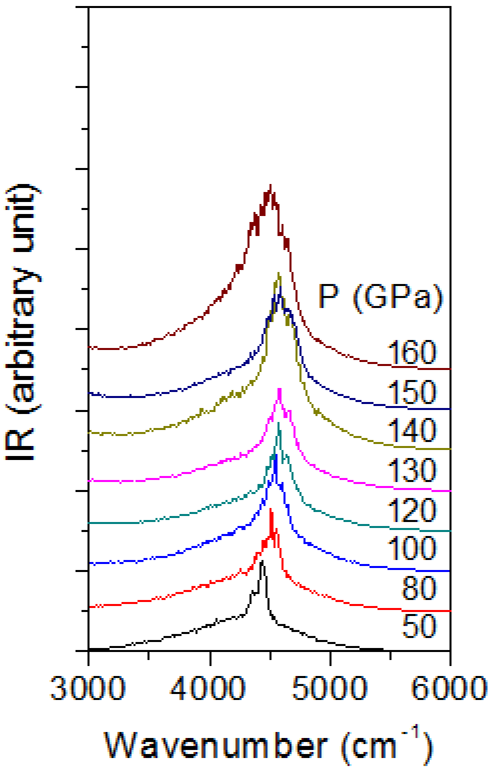

Figure 3. 20 Calculated IR spectra for solid H_2 at different pressures.

The calculated IR spectra at selected pressures from 25 to 160 GPa are displayed in Figure 3. 20. The profile of the IR below 130 GPa is quite similar, but above 130 GPa there is a prominent change. The extracted H_2 vibron frequencies from the IR spectra were compared with the available experimental data [107] in Figure 3. 21. The vibrational frequency was found to increase gradually upon compression from 25 GPa to 140 GPa and then started to decrease at 160 GPa. Both the trend and the calculated frequencies are in excellent agreement with experimental measurements. The change of the vibron frequency at 160 GPa is indicative of a phase transition. As will be shown below, a subtle change in the molecular dynamics occurred between 120 - 140 GPa as well.

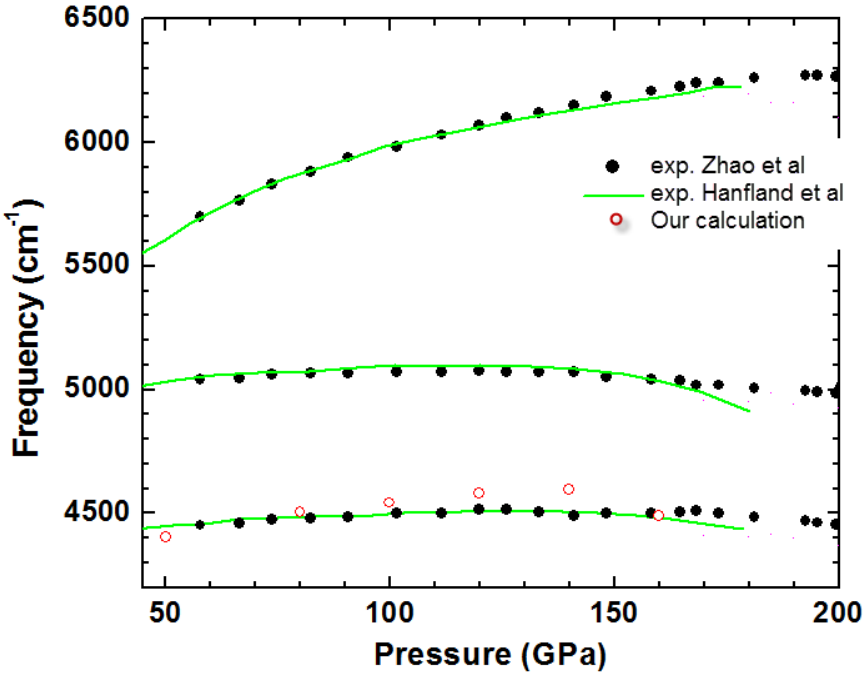

Figure 3. 21 Vibron frequencies from calculated and experimental IR as a function of pressure.

The atom colour-coded dot plots of the MD trajectories of the hydrogen atoms at different pressures viewed along the hexagonal *c* axes (*y*) and orthogonal direction (*x*) are shown in Figure 3. 22 and Figure 3. 23, respectively. Below 100 GPa, the colour-coded dot plots show unambiguously *round* shaped "clouds" in the two orthogonal viewing directions. This showed that the H_2 molecules were freely rotating, as is expected in phase-I. When the pressure was increased from 100 GPa, *triangular* patterns gradually emerged when viewed down the hexagonal *c*-axis (*y*) (Figure 3. 22). However, the *round* "cloud" patterns still persisted in the perpendicular *x* direction (Figure 3. 23). Starting from 130 GPa, *triangular* patterns became more prominent. Concomitantly, the motions viewed down the *x* direction had *flattened*. This indicated the H_2 molecules were no longer freely rotating. Furthermore, a detailed examination showed that the *triangular* features arose from restrictive molecular rotations within the *x*-*z* plane of the orthorhombic cell.

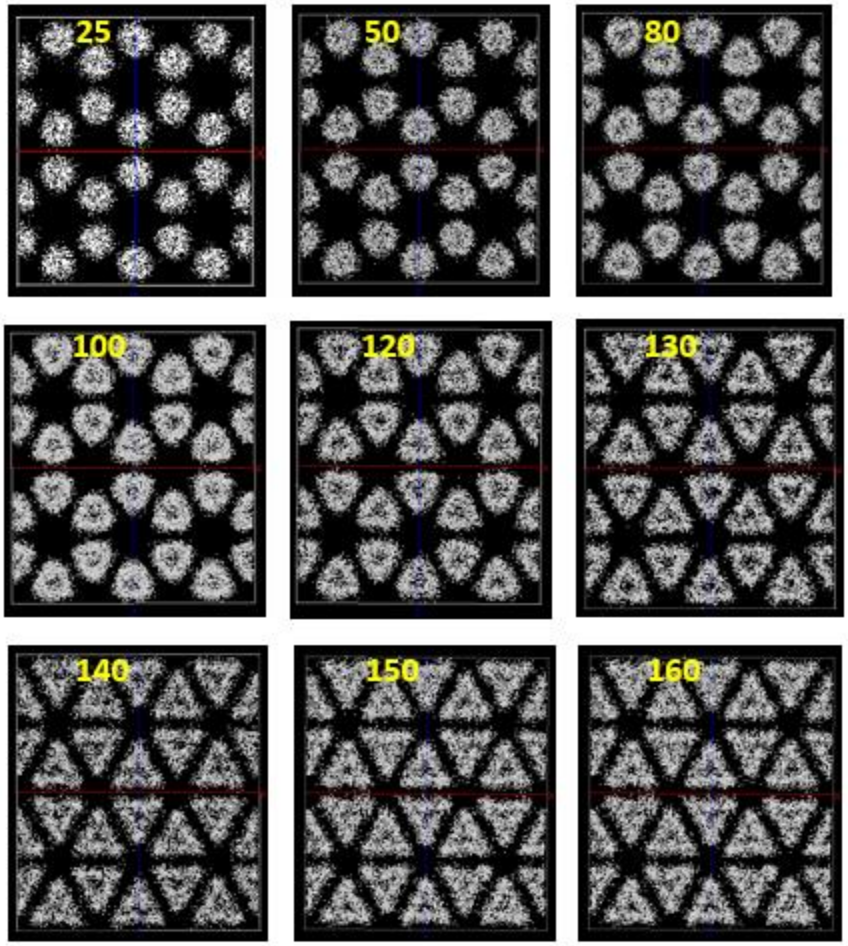

Figure 3. 22 Trajectories of solid hydrogen as a function of pressure. Viewed along *y*-direction. The pressure values (in unit of GPa) are indicated in the plot.

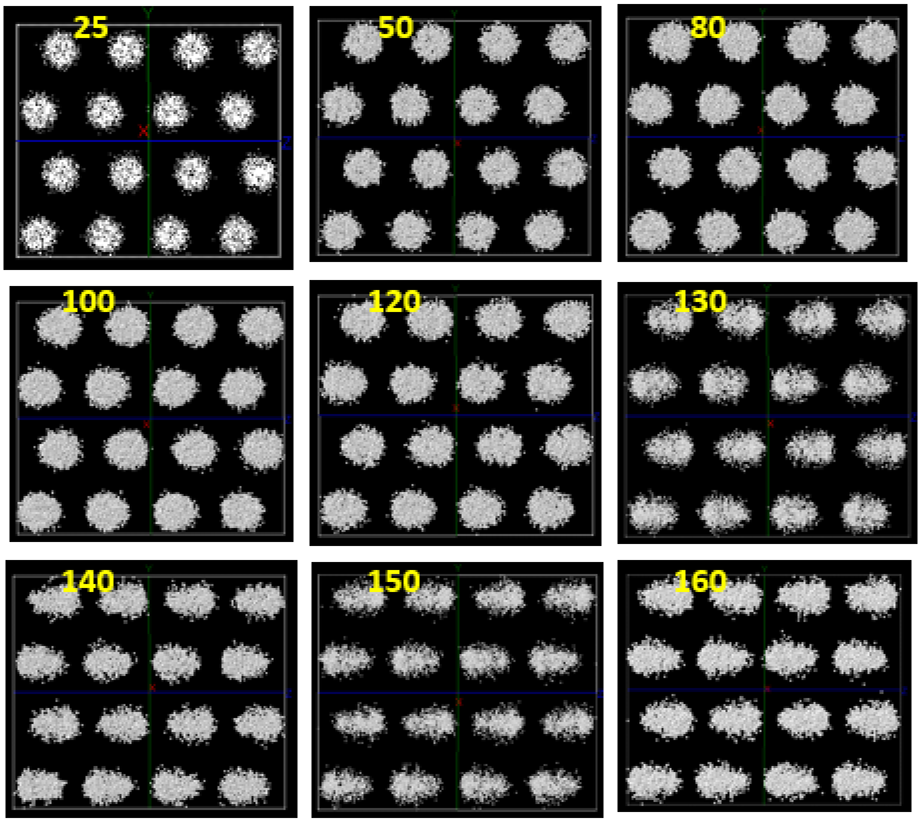

Figure 3. 23 Trajectories of solid hydrogen as a function of pressure. Viewed along *x*-direction. The pressure values (in unit of GPa) are indicated in the plot.

The visually suggestive, restricted H_2 molecular motions were confirmed from an analysis of orientations function P_2 introduced in Chapter 2. The relaxation time at each pressure was estimated by fitting the short-time behaviour of the orientation autocorrelation function $\langle P_2(t)\cdot P_2(0)\rangle$ to an exponential function plotted in Figure 3. 24. It was found that the relaxation time increased abruptly from 15 fs at 120 GPa to 25 fs at 130 GPa. This discontinuity signified a structural transition from a free rotor phase-I to a restricted rotor phase-II. The longer relaxation time in phase-II was the result of restricted H_2 rotations.

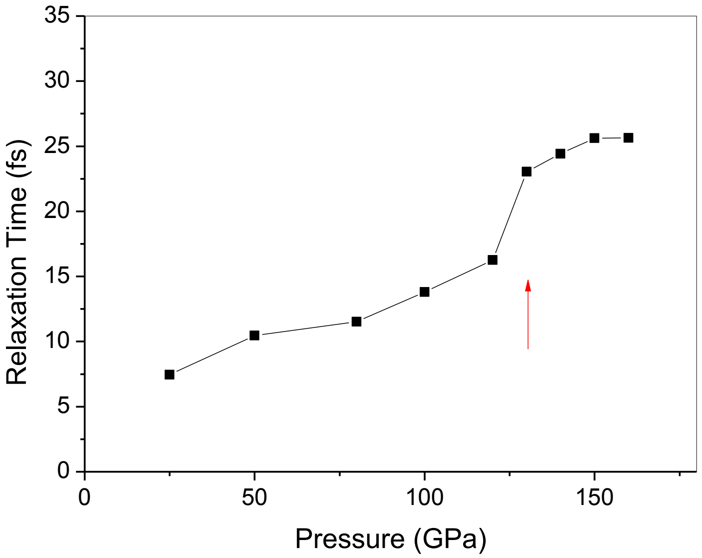

Figure 3. 24 Relaxation time from the time autocorrelation function of $P_2(\theta) = \frac{1}{2}(3\cos^2\theta - 1)$ of hydrogen molecules in the solid state at pressures between 25-160 GPa. The phase-I → II transition is indicated by the red arrow.

At 160 GPa, the large amplitude H_2 rotational motions were largely inhibited and the H_2 molecules were now liberated about their centers of mass. The instantaneous configuration was found to be a layered structure with a monoclinic *C*2/*c* symmetry. This structure is the same as the lowest enthalpy structure previously proposed for phase-III [23].

FPMD calculations correctly reproduced the experimental trend of successive phase transitions in solid hydrogen from phase-I to II to III. The transition pressures at 245 K were estimated at 130 and 160 GPa, respectively. The present results showed that at high compression, free rotation of H_2 was no longer feasible. Calculations of the orientation autocorrelation functions and the relaxation time indicated that at 130 GPa phase-I is transformed to a restricted rotor phase-II. At 160 GPa, rotations were inhibited and phase-II transformed into an orientation-ordered phase-III.

3.2.6 Conclusions

FPMD simulation method was used to study the dynamics and structural transformations in dense hydrogen at 250-300 K and between 250-370 GPa. While previous theoretical prediction studies were focused on the static structures, we investigated structural dynamics near room temperature. It was found that the proposed two distinct layers in phase-IV can exchange dynamically. These molecular layers are composed of rotating H_2 molecules and “atomic” G-layers displaying fast site-to-site proton transfer. These findings are novel and unprecedented. At room temperature, the structure of phase-IV solid hydrogen was dynamic with molecular orientation disorder and large amplitude proton hopping. These results challenge the appropriateness of conventional static space group descriptions of a crystal structure. Nevertheless, the time average structure is close to the *Pc* space group suggested in a theoretical prediction. Simulation results also showed that when compressed to 370 GPa, phase-IV will transform spontaneously to metallic *Cmca*-4 symmetry. The latter structure is still molecular in nature and the existence of a monatomic solid hydrogen structure is still elusive.

CHAPTER 4

IONIC TRANSPORT IN LI-ION BATTERY MATERIALS

As presented in Chapter 1, a rechargeable lithium-ion battery (LIB) consists of three principal components: a positive electrode (cathode), a negative electrode (anode), and an electrolyte (electronic conduction medium). To design LIBs that meet the demands for high-power devices, there are many technical challenges to overcome. Fast charging rate and high energy density are two critical issues. The charging/discharging rate is directly related to Li transport ability. Information on the diffusion mechanisms and diffusion paths is crucial to improve the performance of LIBs. However, the behaviour of Li transport in many potential electrode and electrolyte materials is not well understood. Molecular dynamics based on first-principles methods is able to provide valuable information to characterize Li transport behaviour at the atomic scale.

In this chapter, selected materials of the three components of the LIB were studied using first-principles methods. $LiFePO_4$, a promising replacement to the current $LiCoO_2$ cathode, was investigated in the first part of this chapter and two diffusion mechanisms were revealed by first-principles molecular dynamics (FPMD) simulations. The anti-site pathway (*vide supra*) found in the calculations helps to resolve a controversy on the experimentally-measured Li diffusion dimensionality [110-114]. Based on theoretical results, suggestions for further experimental work to improve the Li transport properties of this material are proposed. The second part of the chapter concerns the possibility of using type-II clathrate Si_{136} as an anode. It was found that this silicon material possesses many properties superior to the current graphite anode. These include its intrinsic metallic character, extraordinary structural stability, as well as low and flat liathiation voltages. The Li migration pathways between the cages in the clathrate structure were studied in detail. An unusual diffusion mechanism involving collaborative motions of Si framework atoms and the formation of transient chemical bonds was revealed. The relatively high activation barrier affects ionic diffusion rate and low Li intercalation concentration limits energy capacity. Despite these shortcomings, Si clathrate is still probably useful as an anode material for specific applications where safety is the highest concern. Finally, the Li transport and ionic conductivity in the potential solid electrolyte material Li_3PS_4 will be studied. The calculated electrochemical window was found not to be as wide as suggested by experiments. The general trends of the Li conductivity in the crystalline γ-, β-Li_3PS_4 as well as the nano-clusters are consistent with experimental observations. In contrast to the expected continuous flow of Li ions, even in the superionic state a hopping mechanism between Li sites was found.

4.1 Cathode: $LiFePO_4$

A systematic survey of suitable cathode materials identified $LiCoO_2$, $LiMn_2O_4$ and $LiFePO_4$ as the most promising candidates. $LiFePO_4$ [115] in particular has attracted the most attention due to its safety, high energy-density, low cost, structural stability and environmental benign properties. $LiFePO_4$ has a maximum lithium intercalation potential of 3.5 V and a theoretical capacity of 170 mAhg^{-1} [116]. In $LiFePO_4$, the O atoms are covalently bonded to the P atoms forming tetrahedral PO_4 units. The PO_4 units reduce the problem of oxygen gas generation due to heating on overcharge which can cause the battery to catch fire when combined with a flammable organic electrolyte. It also has the advantage of being relatively inexpensive. These merits have made $LiFePO_4$ favourable for commercial battery applications. However, a major obstacle to realize the full potential of $LiFePO_4$ is its low electronic conductivity, which inhibits high-rate applications [117].

Many theoretical calculations have been used to investigate the electronic properties of $LiFePO_4$ in order to improve its applicability. Since the valence 3*d* electrons in Fe containing compounds are localized, they are highly correlated. The common density functionals employing local (spin) density approximation (LSDA) or the generalized gradient approximation (GGA) have failed to describe the correlated electronic state. It has been shown that the Hubbard model (LDA/GGA+U), where an onsite repulsion parameter U is used to describe the Coulomb repulsion interaction, is an empirical method that can provide reasonable results [118]. This method is used in this thesis work to study the electronic structure of $LiFePO_4$ [118]. Using an empirical U parameter of 3.71 eV for the Fe 3*d* electrons, the band gap was found to be 3.8 eV and the activation energy for electrical conductivity was *ca.* 0.6 eV [119]. The reason for the low electronic conductivity in pristine $LiFePO_4$ is the intrinsic insulating nature of the material. To achieve a high rate of charge and discharge requires not only high electronic conductivity, but also fast ionic conductivity within the electrode material. The Li ion diffusion constants obtained from Galvanostatic Intermittent Titration Technique (GITT) and Electrochemical Impedance Spectroscopy (EIS) ranged from 10^{-13} to 10^{-16} cm^2/s [8-11]. Efforts to increase electrical conductivity have been focused on particle size reduction [120], carbon coating [116] and cation doping [117, 121]. Very recently, Kang and Ceder demonstrated that extraordinarily high discharge rates of Li batteries with $LiFePO_4$ as a cathode could be achieved with a fast ion-conducting surface phase through controlled off-stoichiometry [122]. This experiment and the hypothesis, however, have been heavily criticized [123]. Fundamental knowledge of the Li diffusion process in $LiFePO_4$ in the atomic scale is essential to determinate the factors governing the electrochemical behaviour of this material.

$LiFePO_4$ has an olivine structure belonging to the *Pnma* space-group. As illustrated in Figure 4. 1, the LiO_6 octahedra are edge-shared parallel to the *b*-axis of the crystal, thus creating Li channels along this [010] direction. These chains are bridged by edge- and corner-shared PO_4 tetrahedra, creating octahedral interstitial sites along the *c*-axis. A cursory inspection of the crystal structure suggests a possible pathway for Li transport is through the Li ion channels along the *b*- or *c*- directions. Previous first-principles calculations [110, 111] indicated that the Li ion mobility was much higher in the diffusion channel along the [010] direction (along the *b*-axis) than the [001] direction (along the *c*-axis). Therefore, it is generally believed that Li ion hopping between channels is highly unlikely. Similar conclusions were reached by the calculations of Islam's group using empirical potential models [112].

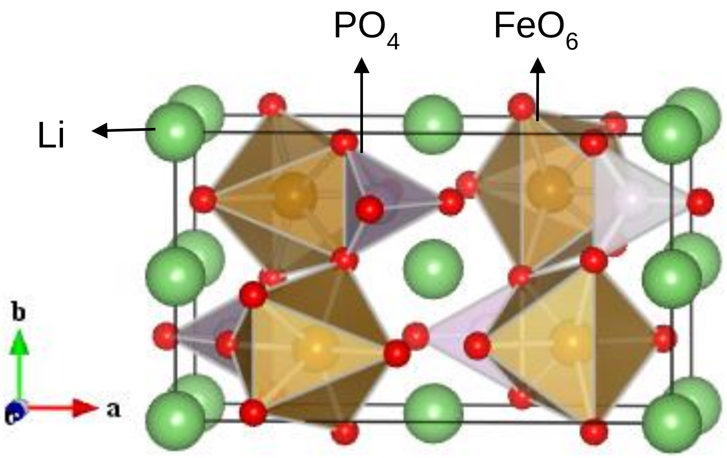

Figure 4. 1 Polyhedral representation of $LiFePO_4$ crystal structure in a unit cell (space-group *Pnma*) viewed along the *c*-direction.

While most theoretical calculations [110-112] agree that the Li ion transport in the ordered structure of $LiFePO_4$ should follow a “zig-zag”, one-dimensional (1D) pathway along the *b*-axis direction, experimental results have been contradictory. For example, measurements on pure and doped single crystals suggest that the low Li ion conductivity is primarily two-dimensional (2D) and confined within the *b*-*c* plane [113, 114]. In contrast, another single-crystal measurement of ion conductivity shows that ionic conductivity along the “*b*” direction is a few thousand times larger than that in the two orthogonal directions consistent with the prediction of a 1D migration pathway [124]. A recent analysis of neutron powder diffraction patterns by Nishimura et al. using the maximum entropy method also revealed a “zig-zag”, 1D pathway for Li ion transport along the [010] direction [125]. On the other hand, there has been recent speculation about the possibility of antisite defects in $LiFePO_4$ that may affect the diffusion behaviour [126, 127]. Classical molecular dynamics simulations have already been employed to investigate how structural disorder (*i.e.*, intrinsic anti-site defects) affects anisotropy of the ionic diffusion coefficient [128, 129]. It was concluded that the anti-site of Fe on Li could impede the Li ion diffusion along the [010] channel.

All previous theoretical studies [110-112] predicting a 1D diffusion along the Li [010] channel were based on the calculation of the migration energy barrier following a pre-conceived “minimum” energy path (MEP). Most calculations were performed with the nudged elastic band (NEB) method [130] which depends on *a priori* assumed initial and final geometry. Because self-diffusion of Li ion in $LiFePO_4$ is a thermally induced process, molecular dynamics simulation offers a more direct approach to explore feasible diffusion pathways. In the present study, the Li ion diffusion behaviour in $LiFePO_4$ was studied with FPMD calculations. As described above, the Hubbard GGA+U model [118] is essential to take into account for the important electron-correlation effect [118], therefore GGA+U FPMD were performed to characterize the Li transport pathways in $LiFePO_4$. To the best of our knowledge this is the first time that a spin polarized GGA+U method was used in a FPMD calculation.

4.1.1 Computational details

Spin polarized FPMD calculations were performed using the pseudopotential plane-wave method with projector augmented wave (PAW) potentials [61, 131] replacing the atomic core electrons. Electron orbitals were represented by the expansion of plane-waves with an energy cutoff of 400 eV. To account for electron correlation in the Fe 3d orbitals, the GGA functional [132] was augmented with a Hubbard on-site repulsion term, U (GGA+U) [133]. The effective interaction U_{eff} = U-J of 4.3 eV, where J represents the Coulomb interaction, was used. This U_{eff} value has been shown to give the correct electronic ground state structure and band gap energy as well as the experimental intercalation potential of $LiFePO_4$ [118]. All calculations were performed with the aforementioned method as implemented in VASP code [60, 134]. Calculations on the ground state properties of bulk olivine-type $LiFePO_4$ (*Pnma*, 28 atoms/unit cell) were performed using a $1 \times 2 \times 3$ Monkhorst-Pack *k*-point mesh [46]. To calculate the electronic density of states (DOS), a denser *k*-mesh of $3 \times 5 \times 7$ was used. Convergence with respect to self-consistent iterations was assumed when the total energy difference between cycles was less than 10^{-5} eV and the residual forces were less than 0.005 eV/Å. In agreement with experimental and previous theoretical studies, the ground state of $LiFePO_4$ was found to be anti-ferromagnetic. Results on the optimized structural parameters and the band gap are summarized in Table 4. 1 and are in substantial agreement with experimental data [118, 135].

Table 4. 1 Comparison of calculated and experimental structural parameters and bandgaps of $LiFePO_4$ (space group *Pnma*).

	a (Å)	*b* (Å)	*c* (Å)	Bandgap (eV)
Calculated	10.4060	6.0565	4.7442	3.64
Experimental [135]	10.3377	6.0112	4.6950	3.8-4.0 [117]

In the molecular dynamic calculations, a 1×2×2 supercell containing 16 $LiFePO_4$ units (112 atoms) was employed. For this fully lithiated $LiFePO_4$ system, the Brillouin zone sampling was performed at the Γ point. Since $LiFePO_4$ is antiferromagnetic, spin polarization (unrestricted) calculations were performed. The model system was first thermally equilibrated in a micro-canonical ensemble (NVE) for 2 ps then followed by a MD production run of 20 ps where the temperature was controlled by a Nose-Hoover thermostat [80]. A time step of 1 fs was used for the integration of the motion equations. Initial simulations performed at 600 and 1000 K showed no significant Li migration, even when simulation time lasted for 20 ps. To reduce the computation effort and increase the possibility of Li ion diffusion, the temperature was raised to 2000 K. It was found that the Li atoms diffused readily. Statistically significant Li diffusion events were obtained by registering a number of atomic jumps for both the Li and Fe atoms in the MD trajectories.

4.1.2 Li self-diffusion mechamisms

Li ion migration in fully lithiated $LiFePO_4$ was observed from the MD trajectory at 2000 K. An important finding was that the Li transport is not the continuous process previously anticipated [125]. In contrast, the migration occurred in discrete steps with the Li ions hopping between different sites but not in a concerted manner. In the crystal structure, each Li atom was surrounded by six nearest O atoms forming a LiO_6 octahedron. The hopping process was highlighted via the examination of the time evolution of the relative Li-O distances, $d_{\mathrm{Li\text{-}O}}(t)/d_{\mathrm{Li\text{-}O}}(t_0)$, where t_0 is the time origin. Oscillation of the relative Li-O distances about a constant mean value indicated the Li ions were trapped. A sudden and dramatic change in the value of the relative Li-O distances, instead, signified that a “jump” (hopping) of a Li ion from one site to another site has occurred. It should be noted that it is not necessary for all six relevant Li-O distances to experience a big change when a Li ion is migrated (*e.g.*, when the initial and final sites share a common O atom at similar distances). All Li atoms in the model system were examined.

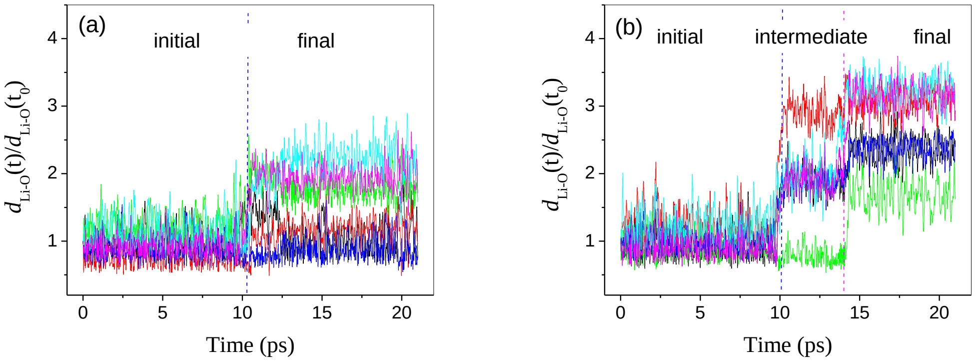

Figure 4. 2 Time evolution function of relative Li-O distances within a LiO_6 octahedron involved in the crystal $LiFePO_4$. The sudden change of the Li-O distance value indicates the hop from one site to another has occurred. (a) a migrating Li ion hops from one Li site to a second Li site along the *b*-axis direction as involved in the first diffusion mechanism; (b) with the second diffusion mechanism a migrating Li ion hops from a Li site to a neighbouring Fe site and then to a second Li site in an adjacent Li [010] channel.

To illustrate the Li hopping process, only two separate events for two Li ions are shown in Figure 4. 2a and Figure 4. 2b. As shown in these Figures, both Li ions hop from one site to another at *ca*. 10.5 ps. In the case of the Li ion in Figure 4. 2b, a more complex diffusion process was identified. At 10 ps it hopped and then became "trapped" at an intermediate site for 4 ps before a second hop at 14 ps. The self-diffusion of Li is therefore not a continuous process as anticipated; rather, it consists of a sequence of consecutive processes where Li ions are trapped momentarily and oscillate for a short time before jumping to the next available site.

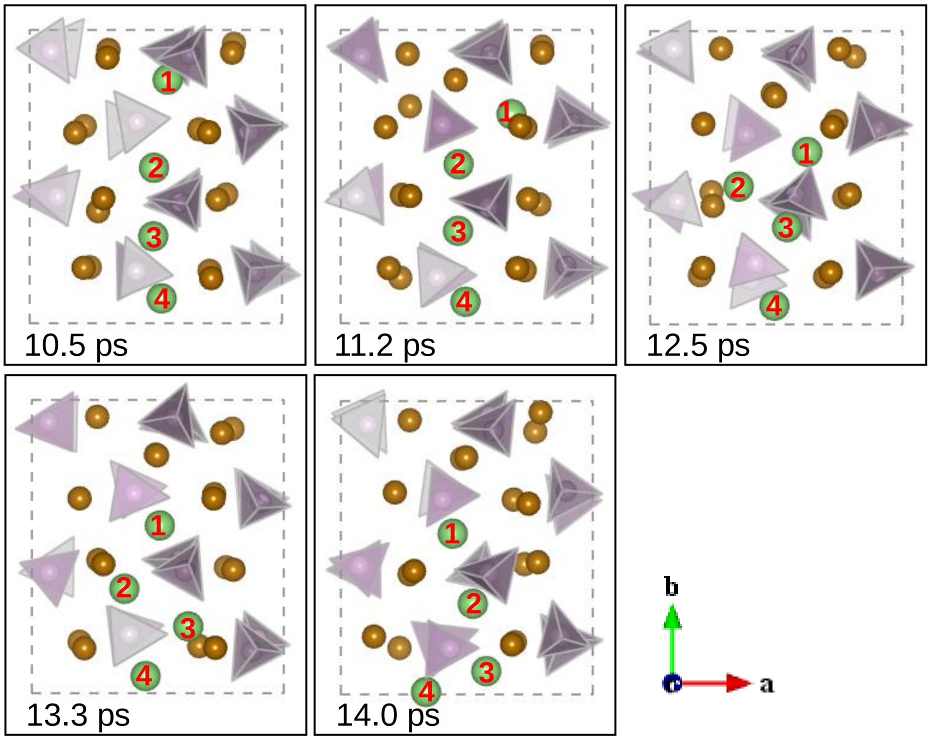

Figure 4. 3 Snapshots from the MD simulation of the fully lithiated $LiFePO_4$ at 2000 K showing Li diffusing along the *b*-axis direction, where those Li atoms without getting involved in this diffusion mechanism as well as those O atoms are not shown for clarity. Large (light green) and small (brown) spheres represent Li and Fe atoms, respectively. Numbers on Li atoms are given indices of atoms in the crystal structure for the facility of description. Dashed lines show the size of the used supercell.

Further analysis of the atomic motions revealed that the two Li ions illustrated in Figure 4. 2 are actually involved in two distinct diffusion mechanisms. In Figure 4. 2a, the adjoining Li ions in the channel parallel to the crystal *b*-axis hopped between the neighbouring Li sites, leading to a 1D diffusion mechanism similar to what has been proposed in previous theoretical calculations [110-112]. A more detailed representation of the atomic processes of this diffusion mechanism is depicted in Figure 4. 3. Four Li atoms are shown with a number index of 1, 2, 3 and 4 in the simulated cell situated sequentially in the channel along the *b*-axis. First, atom Li-1 moved away from its site towards the adjacent Li-2 in a circuitous route. Due to the increased repulsion from the approaching Li-1, Li-2 started to move towards the nearest neighbour Li-3 site on the other side of the channel. Concomitantly, atom Li-3 became displaced and atom Li-4 was pushed away, forming a Fe anti-site (*vide infra*) with atoms Li-1, Li-2 and Li-3 all migrated forward to occupy the former Li-2, Li-3 and Li-4 sites, respectively.

To illustrate the diffusion pathway more clearly, trajectories of three Li atoms (Li-1, Li-2 and Li-3) involved in the migration process are depicted in Figure 4. 4. For clarity, the positions of the “spectator” atoms (*i.e.*, Fe and PO_4) are fixed at their initial configurations. The “zig-zag” diffusion pathway of the Li ions along the *b*-axis channel confined in the *a*-*b* plane can be easily identified. The FPMD calculations also revealed other details about the atomistic migration processes. It was found that the thermal vibration of trapped Li ions is anisotropic with a preferred direction towards the face-shared tetrahedral Li sites (see Figure 4. 4). This picture of the Li diffusion pathway and the vibration anisotropy is consistent with experimental findings [125] and previous theoretical predictions [110-112]. The observation of the replacement of an Fe site by a Li ion in the simulation was due to the fact that our model system was fully lithiated and there were no vacant Li sites. In previous studies [110-112], the presence of defect vacant Li sites was always assumed and no dynamical simulation were performed. Nevertheless, the features for the 1D "zig-zag" Li diffusion pathway observed here is very similar to that obtained before.

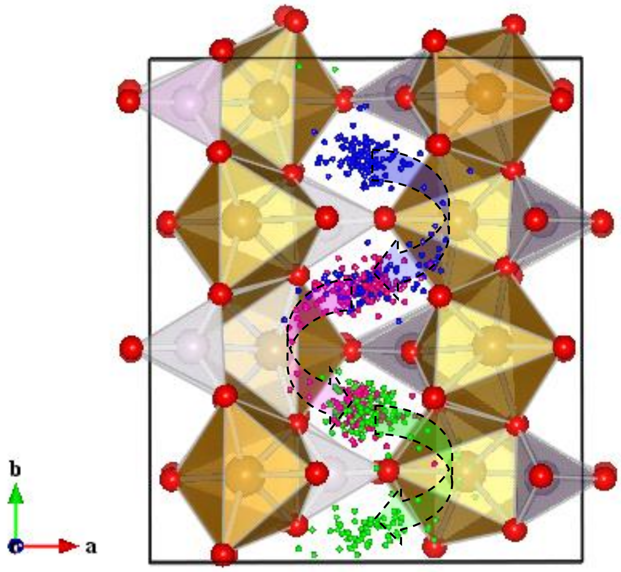

Figure 4. 4 Trajectories of the three Li atoms originally situated in the crystalline $LiFePO_4$ structure along the *b*-axis obtained from the MD simulation at 2000 K. The three specific Li atoms are highlighted with different colours, and all other Li atoms are omitted for clarity. A "zig-zag" diffusion pathway can be clearly identified (shown with the curved arrows) along the *b*-direction and confined in the *a*-*b* plane.

It is surprising that at the transition point when a Li ion migrates and passes the neighbouring PO_4 tetrahedron, there is no noticeable collaborative change in the orientation of the PO_4. One would expect that a concomitant rotation of the PO_4 may help to reduce the repulsion between the three O atoms, forming the tetrahedral face with the hopping Li ion promoting mobility. However, it was found that the orientation change of PO_4 was at the same time scale as that of the thermal effect (refer to Figure 4. 2). The PO_4 tetrahedra were identified as intact with only minor changes in the P-O bond lengths (±0.3 Å). In contrast, the FeO_6 octahedra were more fragile. On a few occasions (*vide supra*) the Fe ions were found to migrate between different sites. As will be described below, this is the basis for the second Li ion migration mechanism.

The second Li ion migration route involved the formation of a Li-Fe anti-site defect (*i.e.*, the exchange between Li and Fe ions). Li-Fe anti-sites have been suggested as an intrinsic defect in $LiFePO_4$ by a theoretical calculation [112]. It was speculated that even at low temperatures there should be a small percentage of Li-Fe anti-sites because of the low exchange energy (*ca*. 0.7 eV) [112]. The Li ion diffusion mechanism involving the formation of a Li-Fe anti-site is illustrated in Figure 4. 5. The mechanism is highlighted from a pair of Li (pink) and Fe (blue) ions in a series of snapshots captured during the MD simulations. It was shown that a Li ion in the [010] channel diffuses to the adjacent Li ion channel facilitated by the formation of a Li-Fe anti-site. A Li ion (see Figure 4. 2b) initially in the Li ion channel displaced a Fe ion in the neighbouring site (anti-site Li) and simultaneously the Fe ion migrated to another Li site, forming an anti-site Fe. The anti-site Li ion continued to migrate to an available Li site in the adjacent Li ion channel. Consequently, Li ion diffusion between adjacent [010] channels can be accomplished with the formation of a pair of Li-Fe anti-sites. This possibility was raised by Malik and colleagues based on the results of static first-principles calculations [136]. The activation energy for a Li ion migrating to the nearest Li channel through a vacant intermediate Fe site was determined to be 0.491 eV. Although this is higher than that the 0.27 eV for Li migration along the [010] Li channel [110], the crossing of the Li ion channels was anticipated to occur whenever the migrating Li encountered an anti-site Fe in the Li channel due to a larger energy barrier along the channel (0.70-0.74 eV) [129, 137]. After crossing the channel, the Li ion can continue migrating in a new diffusion path along a second [010] channel. Migration across channels, however, can reduce the diffusion rate as compared to the 1D diffusion along the [010] channel. Overall, the presence of anti-site defects was expected to reduce Li ion mobility and thus the electrochemical capacity. A low concentration (<3%) of anti-sites has been observed in hydrothermally synthesized $LiFePO_4$ [127]. The result is in reasonable agreement with a scanning transmission electron microscopy (STEM) measurement, where the concentration of anti-site defects was found to be approximately 1% [138]. Recently, Hamelet and colleagues have reported a Li-Fe exchange in $LiFePO_4$-based nano powders with a significant amount of structural defects [139].

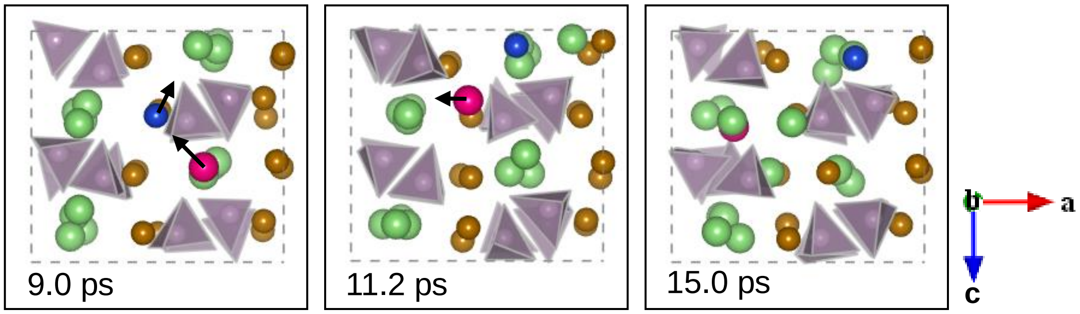

Figure 4. 5 Snapshots from the MD simulation of the fully lithiated $LiFePO_4$ at 2000 K showing the second diffusion mechanism involving the formation of Li-Fe antisite. Large (light green) and small (brown) spheres represent Li and Fe atoms, respectively. A pair of Li (pink) and Fe (blue) atoms are highlighted to illustrate this mechanism. Dashed lines indicate the size of the used supercell.

As discussed above, the formation of Li-Fe anti-sites indicates that the Li diffusion process is “two-dimensional”. The present results lend credence to the recent and perhaps surprising suggestion that Li ion diffusion in single crystal $LiFePO_4$ is 2D [113, 114]. It is possible that this2D diffusion mechanism may affect the overall diffusion rate of Li ions compared to the 1D one along the [010] channel. A future experiment, particularly one considering the temperature effect, may help to resolve this issue since the formation of Li-Fe anti-sites is a thermal activated process. Nevertheless, in a practical $LiFePO_4$ cathode, the concentration of the anti-site defects may be small but it may still impede the normal Li diffusion along the [010] channel.

4.1.3 Conclusions

The Li ion self-diffusion in crystal $LiFePO_4$ has been studied using GGA+U AIMD calculations. Two distinct Li ion diffusion mechanisms were found. The results showed that diffusion processes are more complex than suggested from previous static calculations. The Li migration was shown to involve temporal collaborative relaxation or be assisted by the migration of Li and Fe ions at close proximity. In agreement with previous studies [110-112], a “zig-zag” 1D diffusion along the *b*-axis direction and restricted in the *a*-*b* plane was identified [125]. A second pathway not previously proposed involved diffusion across the [010] channels, aided by the formation of Li-Fe anti-sites. The formation of Li-Fe anti-site defects is consistent with suggestions in experimental findings. Li transport through the anti-site defect is expected to be slower than the route along the 1D pathway down the [010] channel. The simultaneous occurrence of two distinct Li transport processes suggested that the gross result of Li diffusion was not a simple linear process but may exhibit features of a 2D diffusion pattern. It should be recognized that the study of diffusion mechanisms by FPMD is still a challenging problem; this is owing to the limited accessible time scale. The preliminary results presented here demonstrate the strength of this approach in providing deeper insight into the atomistic processes for diffusion mechanisms. Future investigations will focus on realistic systems such as Li transport in partially lithiated Li_xFePO_4 ($x<1$) systems, with and without the presence of an electric field gradient.

4.2 Anode: Type-II Si Clathrate

4.2.1 Introduction

A suitable anode material for rechargeable LIBs is expected to possess the following key properties: an open structure for lithiation and delithiation, a high specific capacity, low and constant voltage, great structural stability and good electron and Li ion conductivity. In practice, it is difficult to satisfy all these conditions with a single material. For example, silicon (Si) has attracted great attention as potential anode application due to its extremely high theoretical specific capacity (4200 mAh/g) [140] compared to the current graphite anode (372 mAh/g). A major obstacle to realize the practical application of these high energy density materials is the significant volume change associated with lithiation and delithiation in the charging and discharging processes. This often leads to anode fractures and failure of the battery [141]. A remedy is to employ nano-structured Si with larger open surface area instead of bulk Si [142]. Below we study another alternative.

Si clathrates are polymorphs of silicon with open frameworks constructed from the three dimensional links of sp^3 Si atoms. Metal atoms can be encapsulated in the empty voids. Since the synthesis of two distinct clathrate phases - Na_8Si_{46} (type-I) and Na_xSi_{136} ($x<11$) (type-II) - was first reported in 1965 there has been considerable interest in exploiting these open framework compounds as tunable semiconductors and thermoelectric materials. Type-I Si clathrate has a simple cubic structure (*Pm*-3*n*) and contains 46 Si atoms per unit cell (Si_{46}). It is composed of two "small" dodecahedron (5^{12}) cages with 20 Si atoms and six larger truncated trapezohedron ($5^{12}6^{2}$) formed by 24 Si atoms. Type-II clathrate consists of 136 Si (Si_{136}) in a face-centered-cubic structure (*Fd*-3*m*). There are also two types of cages: sixteen small (5^{12}) cages and eight large hexadecahedron ($5^{12}6^{4}$) made up of 28 Si atoms. Metal-intercalated Si clathrates exhibit many novel properties, including superconductivity in $Na_2Ba_6Si_{46}$ and Ba_8Si_{46} [143, 144] and tunable electronic properties in Na_xSi_{136} achieved by adjusting the concentration of the intercalated Na [145]. More significantly, silicon clathrate Si_{136} has been found to possess very low compressibility (*i.e.*, comparable to that of the diamond) up to 12 GPa [146], indicating type-II Si_{136} has a rigid framework.

Recently, an American patent suggested that Si clathrates might be used as anode materials for LIB applications [147]. However, there was insufficient information to support this expectation. In this thesis we report a systematic investigation of the suitability of type-II Si_{136} clathrates as anode materials with first-principles calculation methods. The two reasons that type-II clathrates were investigated are: (i) there are more small cages which Li can occupy due to the energy preference of the small guests to the small cages; and (ii) its framework is thermodynamically more stable than type-I, as one would expect from the analogous water clathrates [148]. It was found that pristine Si_{136} clathrate is energetically less stable than the normal face-centered cubic (fcc) Si. However, we demonstrated that the Si_{136} clathrate can be stabilized by doping with barium (Ba) and forming intercalated Ba_xSi_{136} ($6 \leq x \leq 8$) compounds. It is noteworthy that it is possible to synthesize guest-free type II Si clathrate via the controlled thermal decomposition of sodium monosilicide NaSi under vacuum [149]. During the course of this study we reported successful lithiation into the almost empty Si_{136} [150]. However, reversible lithiation/de-lithiation was not demonstrated [150]. Moreover, as will be shown below, intercalation of Li into the empty Si_{136} structure is not sufficient to compensate for the energetic difference of the empty clathrate with respect to fcc Si. This structural instability may explain the observed “collapse” of the clathrate structure during the lithiation process [150]. In comparison, the Si_{136} framework stabilized with the addition of Ba (Ba_xSi_{136} ($6 \leq x \leq 8$)) and the stability was more likely maintained upon reversible lithiation and delithiation cycles. This investigation focused on the Ba-stabilized clathrates and examined their suitability to serve as an anode.

From the present theoretical investigation, it was found that lithiation had a minimal effect on the clathrate structure, indicating the Ba_8Si_{136} clathrate is a nearly zero strain material. The calculated voltage associated with lithiation of Ba_8Si_{136} clathrate was found to be very low and almost constant with Li content. The most significant finding was that the barrier of Li diffusion was determined by the geometry of the polyhedral face (*i.e.*, pentagonal or hexagonal) shared by neighbouring cages. A surprising result was that the energy barrier for Li diffusion through the smaller pentagonal face (Si_5 ring) was lowered significantly by the presence of Ba atoms in the two adjacent $5^{12}6^4$ cages. This unusual diffusion mechanism uncovered here may provide valuable information to help further development of this material as anode for LIBs.

4.2.2 Computational details

First-principles density functional theory calculations on type II Si_{136} clathrate doped with Ba and Li atoms were performed using VASP code [60, 134]. The projected augmented wave (PAW) potentials [61, 131] were used along with the PBE-GGA exchange-correlation functional [40]. For Ba atoms, the 5*s*, 5*p* and 6*s* orbitals were treated as valence. Electron orbitals were represented by a plane-wave basis set with an energy cutoff of 450 eV. Most geometry optimization and electronic structure calculations were performed in the primitive cell comprising of 34 Si (Si_{34}). Brillion zone was sampled with a 6×6×6 Monkhorst-Pack (MP) *k*-point mesh [46]. Self-consistent iteration convergence was assumed when the total energy difference between successive cycles was less than 10^{-6} eV. To calculate the energy of the Li diffusion barriers, an improved NEB method known as the climbing NEB (cNEB) scheme [54] was used. In this case, the full cubic cell was employed to reduce the influence from the effect of periodic images, and a less dense MP *k*-grid of 2×2×2 was used.

4.2.3 Results and discussions

Crystal structure and stability

The conventional cell of a Si_{136} clathrate is shown in Figure 4. 6. Assuming single occupancy (*i.e.*, one guest atom for each cage, which is true for most alkali and alkaline metals), a total of 24 guest atoms were encapsulated into the Si_{136} framework. It is usually the case that larger metal atoms tend to prefer large cages and the converse is true for the small cages.

The first step of the calculation was to optimize the crystal structure of pristine Si_{136}. The calculated lattice constant of 14.73 Å was in good agreement with the experimental value of 14.62 Å [151]. Compared with the conventional fcc Si, the pristine Si_{136} clathrate was found to have a total energy higher by 0.052 eV/Si and was therefore thermodynamically less stable. Encapsulation of metal atoms is needed to help to stabilize the crystal structure [152].

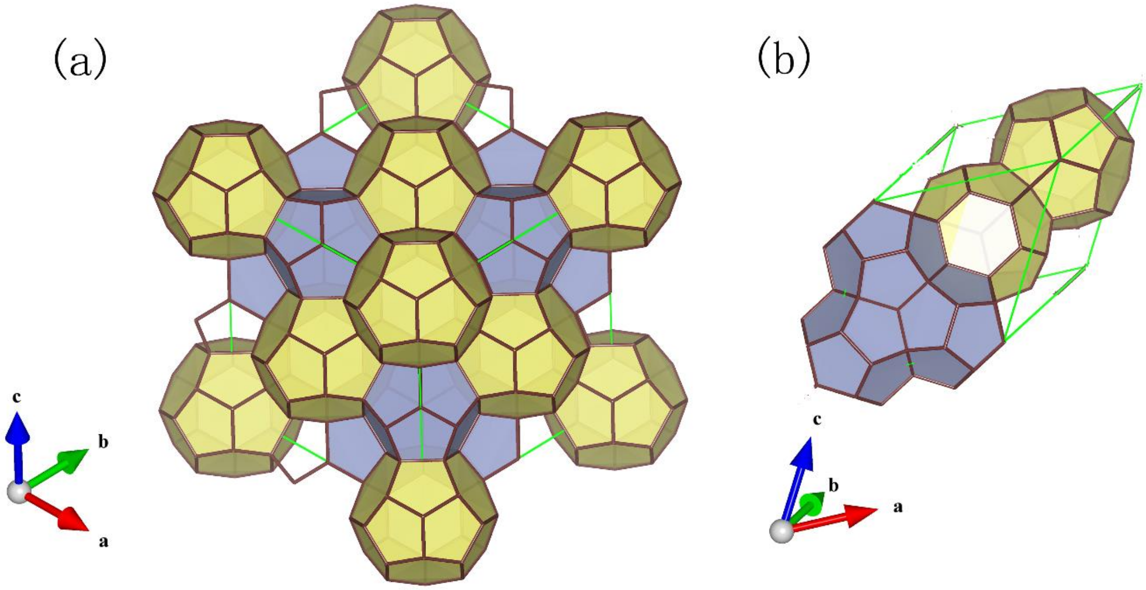

Figure 4. 6 Crystal structure of a type II Si_{136} clathrate with two types of cages: small cage 5^{12} (cyan) and large cage $5^{12}6^4$ (yellow) (a) in the conventional cell and (b) in the primitive cell. Green lines indicate the cell boundary.

First, the effect of Li encapsulation into the cages of an empty Si_{136} was studied. It was noted that Li preferred to be situated at the center of the small cage but off-center in the large cage. Due to their small size, Li atoms preferred the small cages. In fact, when a single Li atom was put in the large cage of an empty Si_{136}, the total energy was raised by 0.060 eV/Li, indicating the structure destabilized. However, when all small cages were first occupied by Li atoms, further doping Li atoms in large cages was found to be energetically favourable as well. The stability of the Li-doped Si_{136} with respect to fcc Si and body-centered cubic (bcc) Li metal was determined by the energy of formation per Si atom, E_{form}. In the primitive cell, E_{form} is calculated by the following formula,

$$E_{\mathrm{form}} = [E(M_x\mathrm{Si}_{34}) - 34E(\mathrm{Si}) - xE(M)]/34 \ , \qquad (4.1)$$

where $E(\mathrm{Si})$ = -5.4249 eV/Si and $E(M=\mathrm{Li})$ = -1.8993 eV/Li. These are the total energies per atom for the fcc Si and bcc Li metal, respectively. A summary of the calculated energies is shown in Table 4. 2. The decreasing formation energy E_{form} indicates that the doping of Li atoms in the clathrate Si_{136} structure is energetically favourable. However, the overall positive values of E_{form} clearly show that the incorporation of Li did not improve the stability of the Si clathrate structures with respect to fcc Si. For this reason, it is not surprising that the crystalline Si_{136} structure was found to collapse upon increasing Li content [150]. It is reasonable to conclude that empty Si_{136} will not be a suitable material for anode application.

Table 4. 2 Formation energy of clathrates $\mathrm{Li}_x\mathrm{Si}_{34}$ ($x \leq 6$) upon lithiation with respect to fcc Si and bcc Li. The first four doped Li atoms were put into the small cages, and then the next two Li were further doped into the two large cages with Li being off the cage centers.

x in $\mathrm{Li}_x\mathrm{Si}_{34}$	**1**	**2**	**3**	**4**	**5**	**6**
E_{form} (eV/Si)	0.051	0.046	0.039	0.030	0.024	0.021

For Si clathrate to be useful as an anode, it is necessary to introduce metal atoms into the $5^{12}6^4$ cages to stabilize the framework while leaving the 5^{12} cages empty to incorporate the smaller Li atoms. For this purpose, the relative stability of Si_{136} clathrate intercalated with Na atoms into the large empty $5^{12}6^4$ cages was calculated. The energies reported in Table 4. 3 show the clathrate structure Si_{136} was not stabilized with respect to fcc Si and bcc Na metal through the addition of Na. It is known that Ba atoms favour the large $5^{12}6^4$ cages [153]. The effect of Ba doping was evaluated from the calculations of the formation energy per Si atom, E_{form}, of the $\mathrm{Ba}_x\mathrm{Si}_{136}$ ($x \leq 8$) clathrates (with conventional crystal cells) based on an equation similar to

Eq.(4.1). The calculated formation energies are summarized in Figure 4. 7, where E(Ba) (= -1.92324 eV/atom) is the total energy for a stable bcc Ba metal. As can be seen from the figure, as the number of encapsulated Ba increased, E_{form} decreased gradually. This indicates that the Ba_xSi_{136} structures are becoming more competitive to empty Si_{136} and Ba metal. At $x \geq 6$, the formation energy became negative, showing that the Ba_xSi_{136} turned out to be more stable than fcc Si and bcc Ba.

Table 4. 3 Formation energy of clathrates Na_xSi_{136} ($x \leq 8$) upon lithiation with respect to fcc Si and bcc Li. E_{form} was calculated in the similar formula of Eq.(4.1) but in the conventional cell.

x in Na_xSi_{136}	**1**	**2**	**4**	**6**	**8**
E_{form} (eV/Si)	0.050	0.049	0.046	0.039	0.036

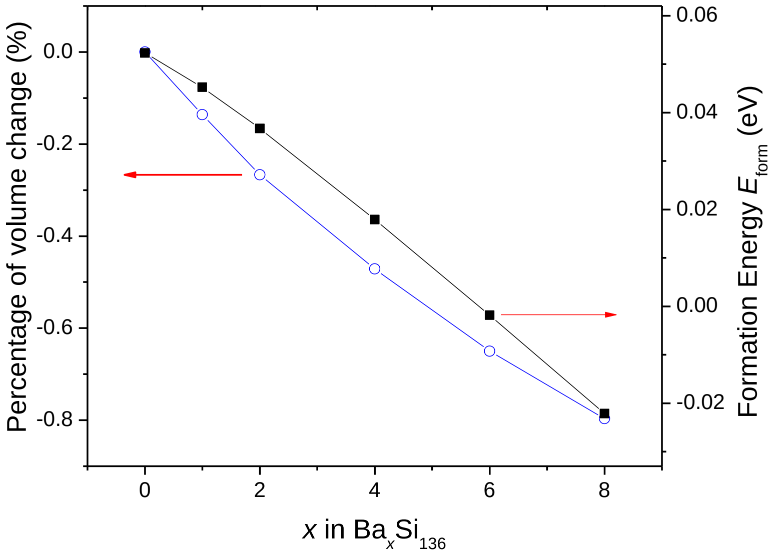

Figure 4. 7 Formation energy E_{form} and the percentage of volume change of Ba-doped clathrates Ba_xSi_{136} as a function of Ba content x.

Upon the addition of Ba, it was also noted that the volume of Ba_xSi_{136} clathrate contracted very slightly (see Figure 4. 7). For example, at the maximum Ba content when the eight large $5^{12}6^4$ cages were completely filled, the volume of Ba_8Si_{46} was only 0.8% smaller than the empty Si_{136}. The almost constant volume over a large Ba concentration indicates rigidity of the open Si framework. Since Li atoms favour the small 5^{12} cages, the ensuing study focused mainly on the stabilized clathrate Ba_8Si_{136}. For reasons to be discussed below, less Ba-doped Ba_6Si_{136} was also studied in the investigation of Li transport mechanisms.

The effect of Li intercalation into Ba_8Si_{136} was studied by gradually filling the 16 small cages. It was found that the smaller Li atoms prefer to reside at the center of 5^{12} cage (see Figure 4. 6). To reduce computational effort, formation energies were calculated in the primitive cell $Li_xBa_2Si_{34}$ ($x \leq 4$). The results are listed in Table 4. 4. All Li-intercalated clathrates had negative formation energies relative to Ba_2Si_{34} (Ba_8Si_{136} in the conventional cell) and bcc Li, indicating the Li occupation of the 5^{12} cages was energetically favourable. The volume of Li-intercalated clathrate as a function of Li content is also tabulated in Table 4. 4. Once again, the cell volume of $Li_xBa_2Si_{34}$ ($x \leq 4$) only reduced marginally with increasing Li content. The overall volume change, however, was negligibly small: only 0.021% when all small cages were filled ($x = 4$). In comparison, the volume changes of other anode materials such as graphite (~10%) [154] and silicon (~400%) [155] are more substantial. The very small volume change for the Si_{136} clathrate was remarkable. This observation showed that $Li_xBa_8Si_{136}$ has superior structural rigidity upon adding and removing Li. This is a critical factor to reduce the fast capacity fading rate during charge and discharge cycles.

Table 4. 4 Formation energy and volume change of clathrates $Li_xBa_2Si_{34}$ ($x \leq 4$) upon lithiation. E_{form} is calculated relative to the Ba_2Si_{34} and bcc Li.

***x* in $Li_xBa_2Si_{34}$**	**E_{form} (eV/Li)**	**V ($Å^3$)**	**$\Delta V/V_0$ (%)**
0	0	794.77	0
1	-0.361	794.18	-0.007
2	-0.378	793.70	-0.013
3	-0.396	793.55	-0.015
4	-0.421	793.11	-0.021

Electronic structure

To examine the effect of Li intercalation on electronic properties, band structures for Si_{34}, Ba_2Si_{34}, $LiBa_2Si_{34}$, and $Li_4Ba_2Si_{34}$ were calculated and compared (see Figure 4. 8). In agreement with previous studies [156-158], empty Si_{34} was found to be a semiconductor with a direct band gap of 1.38 eV. In a Zintl description, the encapsulation of Ba and Li atoms lead to electron transfer from the metal to the Si_{34} framework. As a result, the conduction band of Li- and Ba-doped Si_{34} was populated and showed metallic character. The conduction band profiles of $Li_xBa_2Si_{34}$ (x=1,4) were modified slightly from that of the parent Ba_2Si_{34}. The inherent metallic property of Li-intercalated Ba_8Si_{136} is a distinct advantage for anode applications as it ensures a good electrical conductivity.

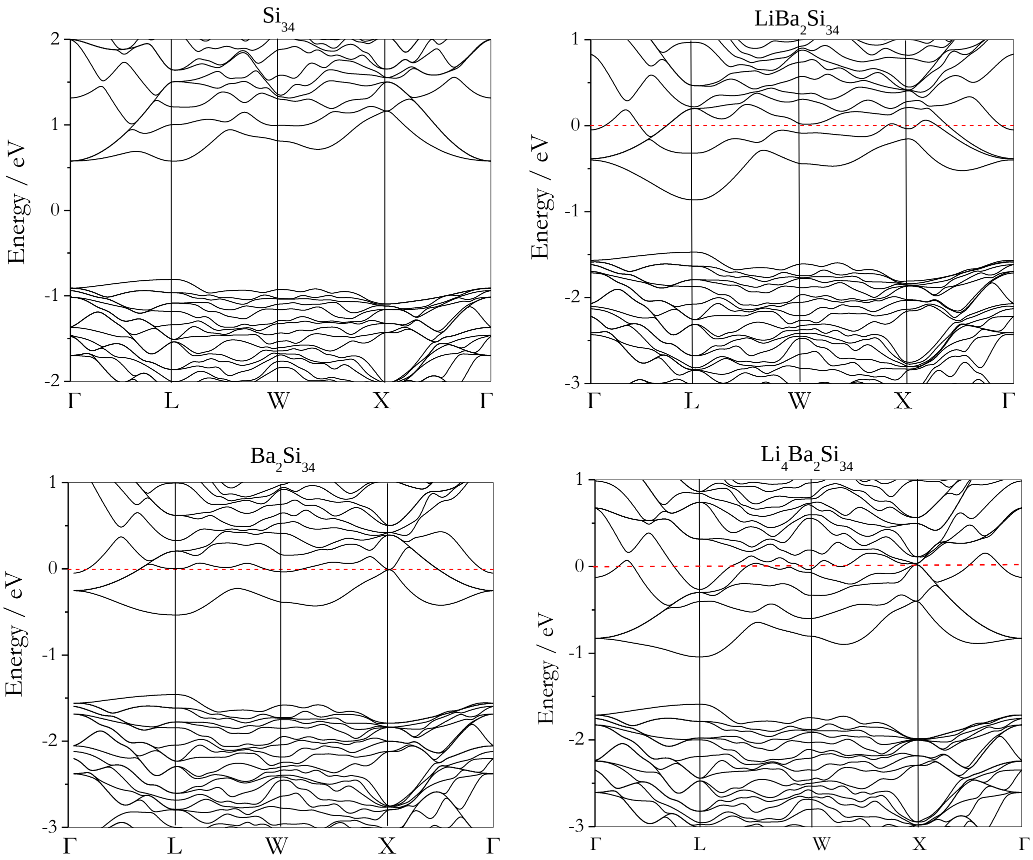

Figure 4. 8 Bandstructures for pristine Si_{34} clathrate (Si_{136} in the cubic cell) and metal-doped clathrates Ba_2Si_{34}, $LiBa_2Si_{34}$, and $Li_4Ba_2Si_{34}$.

Li-intercalation voltage

The voltage associated with lithiation is a critical parameter for anode materials of LIBs. The average voltage V is related to the difference in the Gibbs free energy between the charged and discharged states with Li metal as the reference. Since the contributions of entropy and volume effects to the Gibbs free energy difference are very small, one may approximate the voltage using the energy difference computed at ground state (zero temperature and pressure) [159], given by the formula

$$eV = -[E(\mathrm{Li}_{x+\Delta x}\mathrm{Ba}_2\mathrm{Si}_{34}) - E(\mathrm{Li}_x\mathrm{Ba}_2\mathrm{Si}_{34}) - \Delta x E(\mathrm{Li})]/\Delta x \ , \qquad (4.2)$$

where E is the total energy, e is the free electron charge and Δx is the increment on Li content. This method has shown to be remarkably accurate in predicting voltage profiles for many materials [160]. Figure 4. 9 shows the average intercalation voltage of $Li_xBa_2Si_{34}$ as a function of Li content. It was found that the voltage increased only slightly with Li intercalation. This trend is opposite to those observed in other anode materials [159, 161]. However, the most relevant and important observation is that the overall voltage variation was very flat (< 0.1 V), changing from 0.36 V to 0.46 V for the entire intercalation process until all the small cages were fully occupied. The low and flat potential of ~0.4 V is desirable, as a high cell voltage LIB may be constructed when combined with an appropriate cathode material.

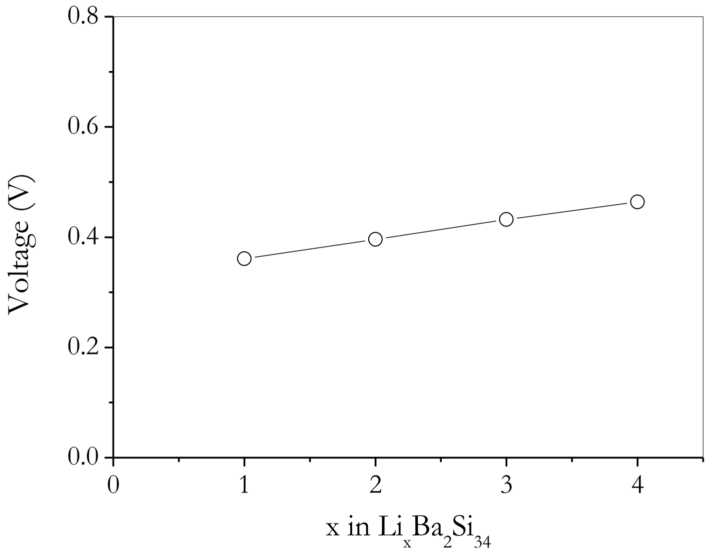

Figure 4. 9 Calculated average voltage of Li intercalation in Ba_2Si_{34} as a function of Li content.

Li diffusion barrier and mechanism

Fast Li ion transport in electrode materials is essential to high power capability (*i.e.*, high rate of charge and discharge) in LIBs. This requires a low energy barrier for the Li ion to migrate in the electrode. To investigate the Li mobility, the crystal structure was examined to identify possible ion diffusion pathways (see Figure 4. 6). In Si_{136} clathrate, the small 5^{12} cage is composed of twelve pentagonal (Si_5) faces, while the large $5^{12}6^4$ cage contains four additional hexagonal (Si_6) faces. Large $5^{12}6^4$ cages share all their hexagonal faces, forming a diamond-like, three-dimensional (3D) network. If all the cages in Si_{136} were accessible by Li, three possible diffusion pathways were identified: (i) between two small 5^{12} cages through the shared Si_5 face; (ii) between small 5^{12} and large $5^{12}6^4$ cages through the Si_5 face; and (iii) between two large $5^{12}6^4$ cages through the Si_6 face. To study the energy barrier for Li diffusion, the potential energy profile along the diffusion path was computed using the cNEB method. In the calculations, selected structures along the pathway between the two fixed end points [54] were fully optimized. All calculations were performed in the cubic conventional cell to avoid fictitious interactions with the periodic images.

In the Ba_8Si_{136} (or Ba_2Si_{34}) system studied above, all large $5^{12}6^4$ cages were occupied by Ba atoms, such that the only accessible migration pathway was through a pentagonal face shared by two small cages. Two models with different Li concentrations were studied. In the first model ($LiBa_8Si_{136}$), there was only one intercalated Li atom. The second model ($Li_{15}Ba_8Si_{136}$) represented the other extreme, where 15 out of the 16 small 5^{12} cages were occupied by Li. The potential energy curves for the diffusion path between two adjacent 5^{12} cages are compared in Figure 4. 10. It was found that the reaction profiles for the two models were quite similar except for a small difference in the activation barriers (0.85 eV and 0.97 eV for the first and second model, respectively). Therefore, it is not unreasonable to expect the energy barrier for other Li concentrations ($1 < x < 15$) should bracket between these two values. Since the reaction profiles as well as energy barriers obtained from these two extreme models were similar, the first model with dilute Li concentration (see Figure 4. 10a) was used for ensuing studies and discussions.

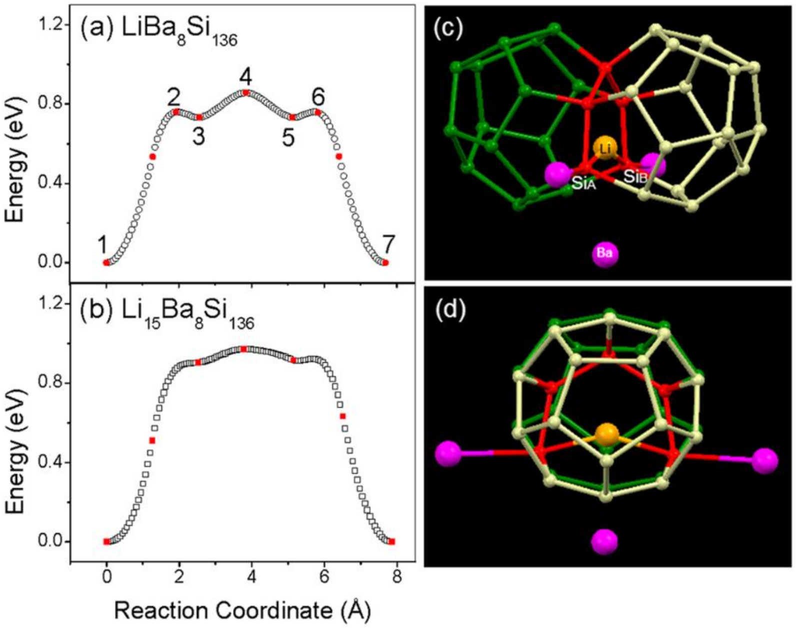

Figure 4. 10 Potential energy curves along the reaction path between two small 5^{12} cages through the shared pentagonal face (red) for the two employed models (a) $LiBa_8Si_{136}$ and (b) $Li_{15}Ba_8Si_{136}$ (see text); (c) side view and (d) front view of the transient configuration of the transition state. For clarity, only the two small cages, as well as the Ba atoms (purple) encaged in the three adjacent large cages are shown. The bonding between Si_A and Si_B is interrupted by the incoming Li atom (brown).

At first glance, the potential energy profile along the pathway (i) was apparently trivially simple that the Li atom migrated directly from one 5^{12} cage to the next nearest 5^{12} cage through the connecting pentagonal face (see Figure 4. 10a). However, the energetically preferred path revealed from an analysis of the trajectory was quite different. In actuality, this process was the result of a sequence of complex processes. The Li did not diffuse freely through the middle of the pentagonal face but rather "through" a Si-Si bond by breaking the bond and forming two transient Li-Si bonds. Significantly, the broken Si-Si bond (denoted as Si_A-Si_B) was not arbitrarily selected but must be the pair connecting the two neighbouring $5^{12}6^{4}$ cages (see Figure 4. 10c and d). The detail diffusion process can be depicted as follows: at the starting point (point **1** in Figure 4. 10a), the Li atom was situated at the center of the 5^{12} cage, corresponding to the global minimum energy along the reaction path. The initial migration step disrupted the favourable interactions between Li and Si cage atoms. The potential energy rose with the displacement of Li from the cage center. As the Li atom approached the common pentagonal face of the neighbouring cage, it deviated from the linear path and moved towards the aforementioned Si_A-Si_B bond. When the atom got even closer (point **2** in Figure 4. 10a), the Si_A-Si_B bond of the shared Si_5 ring was pulled apart with the $Si_A…Si_B$ distance elongated to 4.5 Å. At this point, the potential energy reached a local maximum of 0.76 eV. Further migration towards the pentagonal face re-established the Li-Si interactions between the Li atoms and the Si_A/Si_B atoms and lead to a local potential minimum at point **3**. The transition state with a barrier of 0.85 eV occurred at the highest point **4** where the Li atoms were at the boundary of the two connected 5^{12} cages. Li was located nearly at the center of the broken Si-Si bond and the Li-Si interactions formed transient Li-Si_A/Si_B bonds as short as 2.5 Å. After passing the transition state, the Li atoms followed a mirror route of what had happened before, reaching transition state by migrating towards the new 5^{12} cage center. Concomitantly, the broken Si_A-Si_B bond was recovered during this process. This mechanism maintained efficient Li-Si interactions along the diffusion pathway and at the transition state, even to the extent of breaking a Si-Si bond. This is a surprising but important finding.

Results on the investigation of the other two possible Li diffusion pathways (ii) and (iii) are discussed below. Both pathways involved the migration of Li into a large $5^{12}6^{4}$ cage (*i.e.*, from a small or large cage). In both cases, the large $5^{12}6^{4}$ cages involved in the diffusion paths could not be occupied by Ba atoms. To model this situation, another energetically stable clathrate, Ba_6Si_{136}, was used when the two empty $5^{12}6^4$ cages were located next to each other. $LiBa_6Si_{136}$, a system with a dilute Li concentration, was chosen for detailed study. Prior to modeling the diffusion path, the Li position in the large $5^{12}6^4$ cage was optimized. Unlike the small cage, the intercalated Li atom favoured an off-center position in the large cage and displaced as much as 1.7Å towards the hexagonal face. This configuration displayed a total energy 0.2 eV lower than when the Li atom was at the cage center. This preference towards off-center site in large $5^{12}6^4$ cages has also been reported in Na, Cs and Rb [162] doped type-II clathrates.

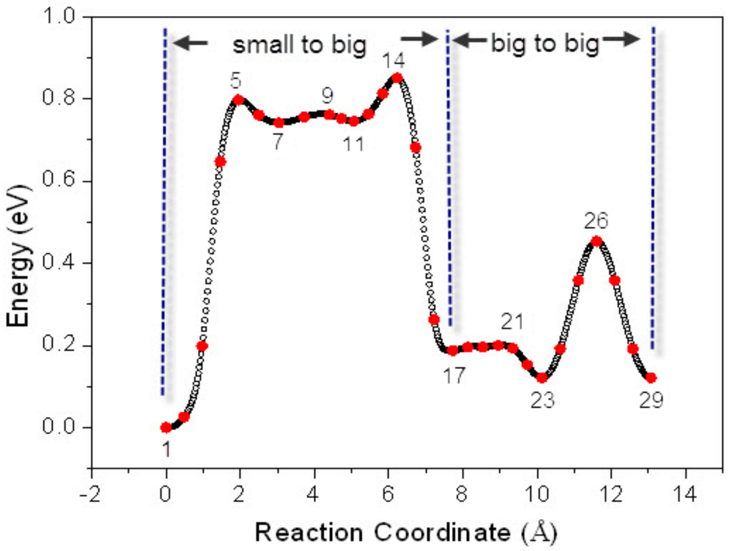

Figure 4. 11 The Li diffusion potential energy along the successive reaction path $5^{12} \rightarrow 5^{12}6^4$ and $5^{12}6^4 \rightarrow 5^{12}6^4$ computed with the $LiBa_6Si_{136}$ model.

The Li diffusion pathways (ii) and (iii) can be collectively represented by successive migration through the polygon faces (*i.e.*, $5^{12} \rightarrow 5^{12}6^4 \rightarrow 5^{12}6^4$). Figure 4. 11 shows the calculated potential energy along the reaction path. The diffusion started with Li at the center of a 5^{12} cage (point **1** in Figure 4. 11). As it approached the pentagonal face, the energy rose quickly up to 0.8 eV (point **5**). At this position, the Li was 1.34 Å away from the small cage center. Instead of approaching the center of the pentagonal face, it moved towards the Si_A-Si_B bond. The diffusion mechanism along pathway (ii) was similar to what happened along pathway (i) (*vide supra*). Like the earlier discussion of Figure 4. 10a (*vide supra*), the Si_A-Si_B bond was disrupted and lead to a local minimum at point **9** as a result of the Si_A-Si_B bond breaking and enhanced interactions between Li and the two Si atoms. After that, the Li entered the first large $5^{12}6^4$ cage. The energy maximum of 0.85 eV at point **14** is simply the mirror image of point **5** but the Li atoms were now inside the large cage. The potential energy dropped quickly to 0.19 eV at point **17** when the Li was 0.12 Å away from the center of the large cage. However, the Li never got closer to the $5^{12}6^4$ cage center; rather, it roamed along the cage wall until it reached the most stable location (point **23**) (*i.e.*, close to the center of the hexagonal Si_6 face shared with the next large $5^{12}6^4$ cage). The Li atom continued to migrate along pathway (iii) (*i.e.*, $5^{12}6^4 \rightarrow 5^{12}6^4$) through the center of the hexagonal Si_6 face (point **26**) to the second large $5^{12}6^4$ cage (point **29**).

The $5^{12} \rightarrow 5^{12}6^4$ barrier was found to be 0.85 eV; this is the same as the barrier of the $5^{12} \rightarrow 5^{12}$ diffusion path (compare Figure 4. 11 and Figure 4. 10a). In the reverse diffusion direction, (*i.e.*, $5^{12}6^4 \rightarrow 5^{12}$) the energy barrier was lowered slightly by 0.12 eV. The results highlight the difficulties for Li to diffuse through the pentagonal faces, either along path (i) or (ii). Nonetheless, both paths were similar and were only slightly influenced by the environment of the starting cage (5^{12} or $5^{12}6^4$). It is noted that the predicted barrier heights were higher than those reported with crystalline Si (0.58 eV) [163]. Overall, diffusion mechanisms for pathways (i) and (ii) involved the breaking and reforming of a Si-Si bond from the pentagonal face to facilitate Li migration through the bond center and avoid the direct penetration through the Si_5 face center. On the other hand, Li migration along pathway (iii) (*i.e.*, $5^{12}6^4 \rightarrow 5^{12}6^4$) through the hexagonal

Si_6 interface was found to have a much lower energy barrier of 0.33 eV. This activation energy is comparable to the Li diffusion barrier (0.12-0.20 eV) found on the surface of Si nanowires [163]. The theoretical results show that Li diffusion through the hexagonal face is easier than through the pentagonal face. As shown above, this seemingly trivial result is much more complicated than a naive consideration of static effect on the size of the open polyhedron faces.

In Si_{136} clathrate, the effective radius of the hexagonal Si_6 ring in clathrate Si_{136} was 2.36 Å. This is comparable to the Li…Si distance of 2.37 - 2.45 Å found in bulk Si when Li is located at the tetrahedral/hexagonal sites [163]. Therefore, when the Li trespasses the Si_6 face center (point **26** in Figure 4. 11) along path (iii), the hexagonal ring is only expanded slightly to a Li…Si distances of 2.43 Å. Consequently, the activation barrier was low for this diffusion path. On the other hand, the pentagonal Si_5 face had a much smaller radius of 2.01 Å. This is too small to allow the Li to penetrate through without severely distorting or even destroying the ring structure. As will be indicated below, forced "squeezing" of the Li through the Si_5 center would result in a very high barrier of 2.08 eV.

To further explore the Si-Si bond breaking mechanism, the role of the participating Si_A-Si_B bond was scrutinized. For example, consider a delithiated Ba_6Si_{136} structure where the Si_A-Si_B bond length of ~2.405 Å is longer than the other Si-Si bond (2.36-2.37 Å) in the same pentagon. A longer Si-Si bond length is an indication of a weaker bond. Therefore, this specific Si_A-Si_B bond should be easier to break. When Li moves towards the pentagonal face, instead of penetrating through the center (which is highly repulsive due to its small opening) directly, the system gains stability from sacrificing a weak Si-Si bond to form two transient Li-Si bonds. This mechanism is akin to that reported for Li-assisted Si-Si bond breaking in bulk Si [164]. Full geometry optimization of the configuration at the transition state showed that the broken Si_A-Si_B

bond “heals” itself when the Li migrated further into the $5^{12}6^4$ cage, similar to what was found along the NEB reaction. The ability to reform the broken Si_A-Si_B bond in the Li diffusion process retains the integrity of the host structure in the lithiation and delithiation processes. In another word, the Li intercalation process is reversible in Si clathrates.

As discussed above, if the Si_A-Si_B bond break is the result of a weak Si-Si bond from the pentagonal face in Ba_6Si_{136}, then what is the reason that the particular Si_A-Si_B bond is weaker than the rest in the same pentagon ring? Even in the empty Si_{136} clathrate, the corresponding Si_A-Si_B bond length was found to be longer than the others at, 2.395 Å versus 2.35-2.37 Å. It was found that the Si_A-Si_B bond length did not change unless the two $5^{12}6^4$ cages connected by the Si_A-Si_B bond were both filled with Ba. In this case, the Si_A-Si_B bond was lengthened to 2.405 Å. In another word, if one of the two adjacent $5^{12}6^4$ cages is occupied by Ba, the effect on the Si_A-Si_B bond length is very small. To test this hypothesis, the diffusion process for a system with only one neighbour Ba occupancy was investigated. It was found through NEB calculations that instead of breaking the Si_A-Si_B bond, the Li “squeezes” through the center of the pentagon. At the transition state, the Si_5 ring was severely distorted and all Si-Si bonds were stretched outwards. The elongated Si-Si bonds had lengths in the range of 2.48-2.80 Å with an average Li-Si distance of 2.21 Å. The significant distortion of the pentagon leads to a very high energy barrier of 2.08 eV. A similar scenario was also found for the Li diffusion between two small cages (*i.e.*, $5^{12} \rightarrow 5^{12}$). These results indicate that when Li is confined in the small 5^{12} cage of Si clathrate, it has a very low probability of diffusing out of the cage if at least one of the two $5^{12}6^4$ cages connected by the Si_A-Si_B bond from the pentagonal face are empty. In contrast, when those two $5^{12}6^4$ cages are occupied by Ba, the Li is able to diffuse via the pentagon interface by breaking the weaker Si_A-Si_B bond with a much reduced energy barrier of 0.85 eV. Therefore, the

Li diffusion mechanism through the pentagonal face is unique. It is dependent on the occupancy of the adjacent large cages by Ba. Under favourable conditions, the Si_A-Si_B bond connected by the two large cages can be broken and then reformed during the Li migration. It could be that breaking the Si_A-Si_B bond is easier when the two adjacent $5^{12}6^4$ cages are occupied because of transferred valence electrons from the Ba atoms into the Si clathrate framework. These “extra” electrons occupy the empty anti-bonding Si-Si levels in the conduction band and weaken the specific Si-Si bond.

Storage Capacity

Since only one Li atom can be inserted into each small cage, a maximum of 16 Li atoms can be stored in Ba_8Si_{136} clathrate. The calculated theoretical discharge capacity of $Li_{16}Ba_8Si_{136}$ clathrate was 85 mAh/g, which is much smaller than the reversible value of 320 mAh/g of the current LiC_6 anode. However, as the results presented above show, it is not necessary to completely fill the large cages with Ba to stabilize the Si_{136} framework. For example, in Ba_6Si_{134} there are two large, vacant cavities where additional Li atoms would be inserted. Moreover, due to the size of the $5^{12}6^4$ cage, it may even accommodate more than one Li atom. Theoretical calculations showed that the $5^{12}6^4$ cage could, in principle, accommodate up to three Li atoms without significantly affecting the crystal structure and volume. The hypothetical $Li_{16+3\times2}Ba_6Si_{136}$ clathrate can achieve a maximum capacity of 123 mAh/g. This value can be compared with the capacity of 140 mAh/g for $LiCoO_2$ [165] and 170 mAh/g for $LiFePO_4$ [116] cathodes. Although the theoretical capacity for $Li_{16+3\times2}Ba_6Si_{136}$ clathrate is still lower than the graphite, it matches well with these cathode materials and therefore may be suitable as an anode. On the other hand, when compared with the extremely high theoretical capacity (~4200 mAh/g) of Si anode, a lower

Li storage capacity in Si clathrates is not surprising. The lithiation process in Si clathrates is based on an intercalation mechanism, which is not the same as the alloying one as found in the Si anode where the crystal structure has completely changed.

4.2.4 Conclusions

A systematic and comprehensive investigation using first-principles calculations on the structural stability, electronic properties, Li intercalation voltages, Li ion diffusion mechanisms and theoretical capacities of thermodynamically stable lithiated Ba_8Si_{136}/Ba_6Si_{136} clathrates was performed. The Ba-doped clathrates were found to possess very high structural rigidity, almost insensitive to the intercalated Li content. This property is far superior to the currently used anode materials in LIBs and ensures structural integrity for repeated charge and discharge processes. The lithiated clathrates are metallic and therefore expected to have good electrical conductivity. The average intercalation voltage was found to be roughly constant at ~0.4 V relative to Li metal. The low and nearly constant voltage is a good feature of an anode for the design of high cell voltage and long life-time LIBs. The most chemically interesting observation was the Li diffusion mechanisms. The barrier through the hexagonal face was 0.33 eV, which is much lower than that through the pentagonal face of ~0.85 eV. Surprisingly, the energy barrier through the pentagonal face was found to depend on the occupation of the neighbouring large cages connected by a Si-Si bond from the Si_5 face. When the two adjacent large $5^{12}6^4$ cages were occupied by Ba, this Si-Si bond was broken upon lithiation, which lowered the “diffusion” barrier from 0.85 to 0.73 eV. If at least one of the above mentioned two large cages was empty, the pentagon face would be distorted and expanded extensively in order to accommodate the migrating Li, resulting in a substantially higher migration energy barrier of 2.08 eV. In summary, the structural rigidity, low and flat voltage, metallic property and reasonable Li transport barriers of Ba-doped Si_{136} clathrates offers the possibility of potential applications as anode materials for LIBs. On the other hand, the theoretical capacities for the lithiated Ba_8Si_{136}/Ba_6Si_{136} clathrates studied here are relatively low but still comparable with the current favourable cathode materials. Previously, single crystalline nanostructures of clathrate-II phase of Na_xSi_{136} have been successfully synthesized [166]. In order to fulfill the useful Li storage capacity of Si_{136} clathrate as an anode, we suggest synthesizing the stable crystalline Ba_6Si_{136} first. The crystalline nanoparticles of Ba_6Si_{136} may then be pressed into a pellet and used as the anode in LIB. Finally, it is noteworthy that there is another class of metal doped Si-clathrate with a channel framework (*e.g.*, $BaSi_6$ [167]) that can also be explored as potential anode materials, as the shared polyhedral face along the channel is expected to have a larger opening size than a regular pentagonal face. This, in turn, might lead to faster Li transport.

4.3 Solid Electrolyte: Li_3PS_4

4.3.1 Introduction

Currently, most lithium-ion batteries use organic liquids as an electrolyte. This choice has imposed a limit for achieving high energy density as it poses significant safety problems (*e.g.*, explosion and fire). For example, liquid electrolytes are expected to react with a graphite anode. On the other hand, lithium metal has the highest gravimetric energy density of all anode materials; however, it cannot be used as an anode in conjunction with a liquid electrolyte due to the electrochemical reaction with the organics. The formed solid-electrolyte-interface (SEI) layer can significantly decrease battery performance and create severe safety problems. Several recent articles suggest that replacing organic liquids with solid-state electrolytes will provide high energy density cells and may eliminate some of the potential hazards [7]. Solid electrolytes such as superionic Li conductors are expected to be more stable and safer. A major limitation in the application of the current solid electrolytes is that the ionic conductivities are generally too low to meet LIB requirements. Therefore, the search for new solid Li electrolyte materials is an active research area.

The prospect of the design of LIB batteries with solid electrolytes was encouraged by the discovery of crystalline $Li_{10}GeP_2S_{12}$ [168], synthesized by partially substituting the P with Ge in Li_3PS_4. This has a room-temperature ionic conductivity comparable to that of liquid electrolytes [168]. A more recent study [169] reported nanoporous Li_3PS_4 and also showed significant technological promise with ionic conductivity improved by several orders of magnitude as compared to the crystalline forms [170, 171].

Bulk Li_3PS_4 exists in the γ-phase (SG: $Pmn2_1$) at room temperature. It transforms to the β-Li_3PS_4 phase (SG: *Pnma*) when heated to 195 ^oC [171]. The ionic conductivity of γ-Li_3PS_4 was measured to be 3×10^{-7} S cm^{-1} at room temperature. The ionic conductivity increased abruptly when it transformed into the β-Li_3PS_4 form [170, 171]. A conductivity of 8.93×10^{-7} S cm^{-1} was found when the conductivity of β-Li_3PS_4 from the Arrhenius plot (see Figure 1 in [169]) was extrapolated to room temperature. This value is much higher than that of the room temperature γ-phase. Synthetic nanoporous Li_3PS_4 has a conductivity nearly three orders of magnitude higher than the crystalline forms reported [169]. High Li conductivity in solid electrolytes is often attributed to fast diffusion (*i.e.*, superionic conductivity) of Li ions in its structural framework. A recent theoretical study [172] analyzed Li mobility in both γ- and β-Li_3PS_4 phases with the NEB method [51, 52] and it was found that there were multiple energy valleys for Li ions. The calculated activation barriers were very low, less than 0.3 eV. However, no details on the transport mechanism were studied. The NEB method is a series of static calculations depending on *a priori* assumed initial and final geometry. Alternatively, finite temperature molecular dynamics is an effective tool for the exploration of potential energy surface. As demonstrated in the study of $LiFePO_4$ (*vide infra*), FPMD has been successful in identifying a non-intuitive antisite diffusion pathway of Li ions [173]. In this work, the same simulation method was used to investigate the diffusion processes in the two crystalline phases (β- and γ-Li_3PS_4) and the nanoporous cluster.

4.3.2 Computational details

All calculations were performed using the GGA-approximation with the PBE functional [40] implemented in the VASP [60, 61]. PAW potentials [65] were used in conjunction with a plane-wave basis set with an cutoff energy of 280 eV to describe the electronic wave functions. The structures of γ- and β- crystalline phases were optimized within the conventional cells. The electronic structures were calculated from the optimized structures. The Brillouin zone was sampled with a *k*-mesh of $5\times6\times6$ and $3\times5\times6$ for the γ- and β-Li_3PS_4, respectively. For the DOS calculations, denser *k*-meshes of $10\times12\times13$ and $6\times10\times12$ were used. Model supercells containing 16 Li_3PS_4 and 128 atoms were used for the γ- and β-phases in MD calculations. For both crystalline phases, experimental lattice constants were appropriated for the chosen simulation temperatures [71] used.

Bulk γ-Li_3PS_4 has an ordered structure where all the atomic sites are fully occupied. The structure of β-Li_3PS_4 is more complicated, since some of the Li sites are partially occupied. The occupancies of the 4b and 4c Wyckoff sites are 0.7, and 0.3, respectively [171]. In this study, one random configuration with the correct stoichiometry was chosen as the initial structure for β-Li_3PS_4. To mimic the nanoporous β-Li_3PS_4, a cluster model with a diameter of *ca.* 9 Å was carved out from the crystalline structure of β-Li_3PS_4. The number of Li atoms on the surface was adjusted to ensure that the cluster contains the correct chemical formula of Li_3PS_4. In total, the cluster contained 160 atoms composed of 20 Li_3PS_4 units. The cluster was put in a cubic box with a cell size of 30 Å. A vacuum layer *ca.* 20 Å thick was used to prevent the interaction of the cluster with its periodic images. Due to the large supercell and the insulating nature of the system, only one *k*-point of $1\times1\times1$ was used. A timestep of 1 fs was used in the integration of the equations of motion. The model systems were first thermally equilibrated in the NVE ensemble for about 4 ps. This is followed by a NVT MD production run for additional 24-150 ps. The temperature was controlled by the Nose-Hoover thermostat [80].

The optimized lattice constants for the low-temperature phase γ-Li_3PS_4 in the orthorhombic cell (SG: *Pmn*2$_1$) were $a = 7.771$, $b = 6.623$ and $c = 6.221$ Å. These are comparable to the experimental results at 297 K of $a = 7.708$, $b = 6.535$ and $c = 6.136$ Å [171]. The volume deviation was only 3.6%. For the high temperature β-Li_3PS_4 phase (SG: *Pnma*), the optimized lattice constants of $a = 12.966$, $b = 8.115$ and $c = 6.195$ Å are in good agreement with the observed values at 673 K of $a = 12.819$, $b = 8.219$ and $c = 6.124$ Å [171] with a volume deviation of 1.0%.

4.3.3 Results and discussions

Electrochemical window

The electrochemical window of crystalline Li_3PS_4 was estimated using the approach outlined in a previous paper [174]. Briefly, this approach involved calculating the DOS of Li_3PS_4 to determine the band gap between the lowest unoccupied molecular orbital (LUMO) and the highest occupied molecular orbital (HOMO) energies. The DOS calculated at the respective optimized geometries of both crystalline phases is plotted in Figure 4. 12. We found that the band gaps E_g for both crystals were similar at 2.2 eV, but these values were lower than the estimated energy gap (>5 eV) from an electrochemical measurement [169]. These results are to be expected as it is well known that GGA functionals always underestimate the calculated energy gap. As discussed by Mo and colleagues [175], another possibility for the discrepancy may be that the experimentally reported Li_3PS_4 electrolyte might not be entirely from intrinsic material but rather affected by passivation.

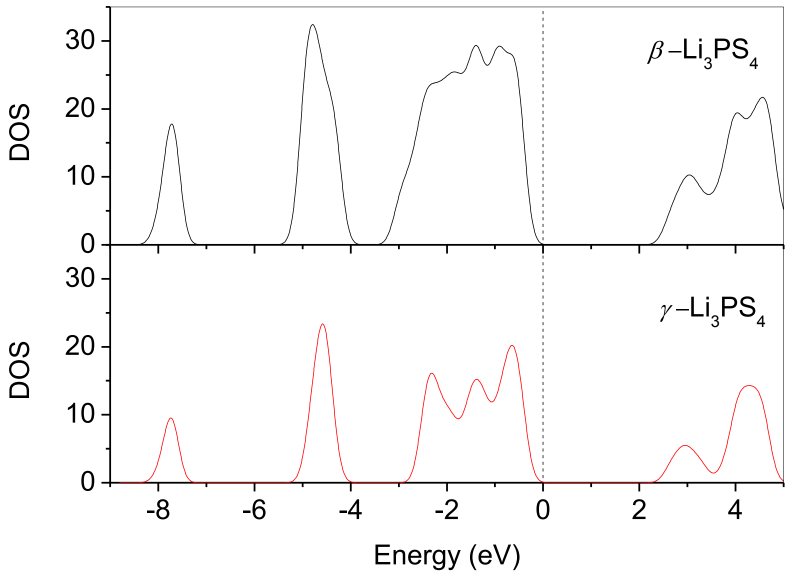

Figure 4. 12 Calculated DOS of optimized β- and γ-Li_3PS_4 crystals.

Li diffusion in crystals

The diffusion of Li ions in the two crystalline structures were examined with FPMD. The systems were overheated slightly to accelerate their dynamical processes [173, 175]. Figure 4. 13 shows the trajectories of Li ions as well as those of P and S atoms in crystalline γ-Li_3PS_4 at 500 and 800 K. At 500 K, displacements of the atoms are generally confined to vibrations around their regular crystal lattice sites, with occasional events on the migration of Li atoms. When the temperature was raised to 800 K, the PS_4 tetrahedrons continued to liberate about their equilibrium positions although the amplitudes were fairly large. In contrast, the Li atoms became diffusive. This is indicative of sub-lattice melting of the Li ions in the γ-Li_3PS_4, resulting in a superionic state.

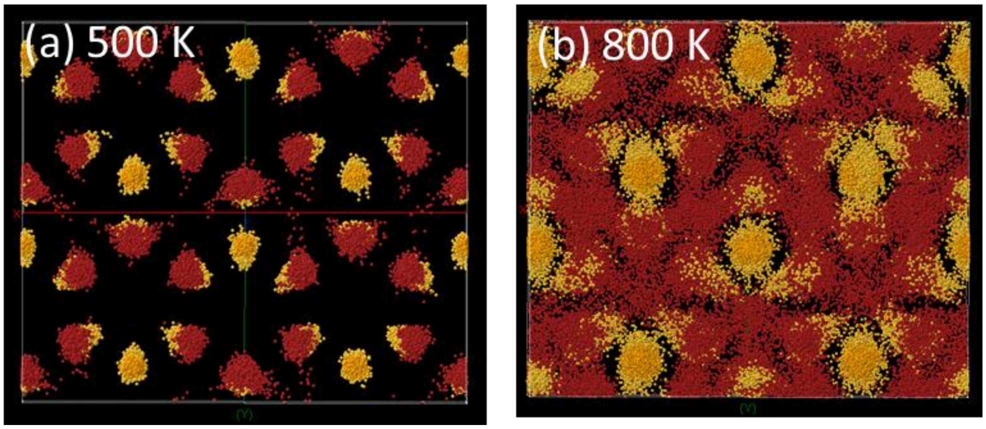

Figure 4. 13 Trajectories for Li ions in perfect crystal γ-Li_3PS_4 at (a) 500 K and (b) 800 K. The red, brown, and yellow colour dots correspond to the superposition of the Li, P, and S atomic positions along the simulation 50-90ps, respectively.

A similar MD calculation was performed on β-Li_3PS_4. Specifically, we wished to examine if the presence of intrinsic Li defects would enhance the migration process. In comparison to γ-Li_3PS_4, even at 500 K Li ions were found to diffuse in the β-Li_3PS_4 crystal lattice. The Li ion motions were not continuous. The ions spent most of their time vibrating around the crystal lattice sites. Occasionally there was a jump from an occupied to an unoccupied site. For clarity, Figure 4. 14 displays the trajectory of only a single, randomly chosen Li ion in the β-Li_3PS_4 crystal within a time segment of 85 ps. The hopping mechanism is clearly identifiable. When the temperature was raised to 800 K, the hopping mechanism became more frequent with the distribution of Li and was more diffusive along the interstitial channels. The Li^+ ion trajectory is now quite similar to that of the γ-phase shown in Figure 4. 13(b).

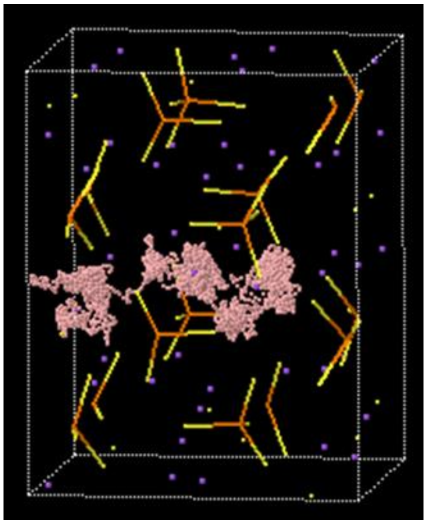

Figure 4. 14 The trajectory of a particular Li atom (rose colour dots) in the β-Li_3PS_4 crystal within a simulation of 85 ps at 500 K. PS_4 framework is shown by sticks, and purple dots are the initial positions for all Li atoms.

It is convenient to quantify the Li motion from the calculation of the atomic mean square displacement (MSD):

$$\left\langle [\mathbf{r}(t)]^2 \right\rangle = \frac{1}{N}\sum_{i=1}^{N}\left\langle [\mathbf{r}_i(t+t_0)-\mathbf{r}_i(t_0)]^2 \right\rangle \ . \qquad (4.3)$$

The average in Eq. (4.3) is over all Li atoms, where $\mathbf{r}_i(t)$ is the displacement of the i-th Li atom at time t and N is the total number of Li atoms taken into account. For a normal Brownian diffusion, the MSD plot has a linear behaviour with time and the slope is proportional to the diffusion coefficient (*D*).

Figure 4. 15 shows the time dependence of calculated MSD for γ- and β-phases of Li_3PS_4 at different temperatures. A linear behaviour was observed in both phases. In γ- Li_3PS_4 (Figure 4. 15(a)), the slope of the MSD is almost zero, showing the Li does not diffuse at 500 K. The diffusion rate, however, increased rapidly at 800 K. In comparison, as shown in Figure 4. 15(b), at 500 K Li the β-Li_3PS_4 has already started diffusing, although the rate is slow. At 800 K the diffusion rate for both crystalline phases was comparable.

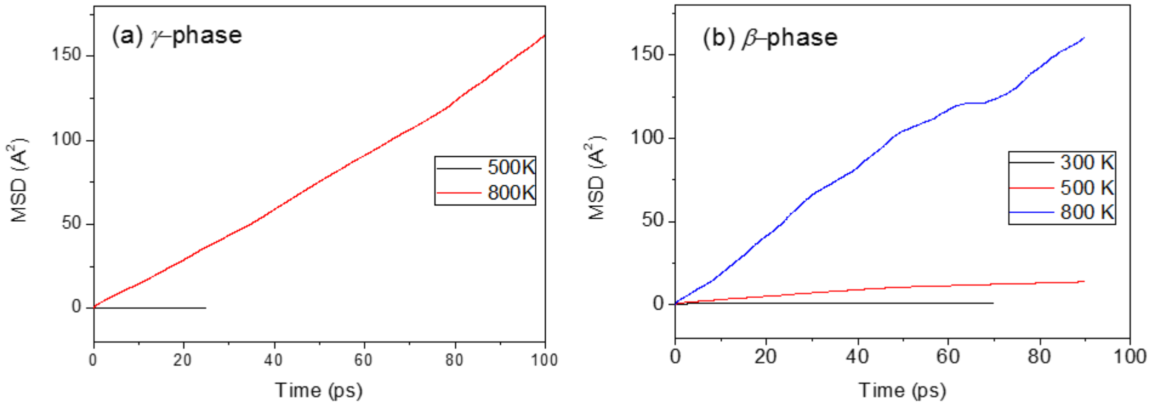

Figure 4. 15 The MSD as a function of time *t* for (a) γ- and (b) β-phases of Li_3PS_4 at different simulation temperatures.

As explained in Chapter 2, the diffusion rate *D* can be calculated from either the slope of the MSD according to Eq.**(2.36)** or from the velocity autocorrelation function using Eq.**(2.33)**. At infinite time, results from both methods should be identical. Using Eq.**(2.33)** at 800 K, the diffusion coefficient of γ-Li_3PS_4 was calculated to be 3.45×10^{-5} cm^2/s. This value is typical of superionic conductors. For β-Li_3PS_4 at 50 K the calculated *D* was quite low (0.13×10^{-5} cm^2/s). The diffusion rate increased 30 times at 800 K to 3.55×10^{-5} cm^2/s and was slightly higher than the *γ*-phase. At present, there is no experimental data for the self-diffusion constant of Li in Li_3PS_4. However, the diffusion rate can be estimated from ionic conductivity measurements. To make a direct comparison, we used the Nernst-Einstein relationship [176]

$$\sigma = n(ze)^2 D / k_B T \tag{4.4}$$

to link the conductivity σ to the diffusion coefficient *D*. In Eq.(4.4), *n* represents ionic concentration (*i.e.*, the number of ions per unit volume), *z* represents the valence of the charge carrier (in this case $z=1$), *e* represents the elementary charge of an electron, k_B represents the Boltzmann constant and *T* represents temperature. Using Eq.(4.4), the calculated bulk conductivities for *γ*- and *β*-Li_3PS_4 at 800 K were 1.39 and 1.51 S/cm, respectively. The experimental values extrapolated to 800 K were 0.025 and 0.068 S/cm, respectively [169]. The theoretical results are larger than the experimental values by one order of magnitude,, but the general trend (*i.e.*, that the diffusion rate in the *β*-phase is faster than in the *γ*-phase) is consistent with the experimental observations [169]. Equation (4.4) is applicable to a special case of single ions and random jumps in the system. In the above discussion, we have shown that the Li transport in Li_3PS_4 is through a series of hops and is a collaborative process. Therefore, the motions of the Li ions are correlated. In this case, the estimated conductivity from Eq.(4.4) will be an upper limit. The calculated value should be weighed by a correlation factor (< 1) governing the probability for Li site-to-site hopping which is expected to be higher in the *β*-phase, due to the intrinsic Li vacant sites, than the pristine *γ*-phase.

Li diffusion in nanoporous Li_3PS_4

Nanoporous Li_3PS_4 synthesized from *β*-Li_3PS_4 has been reported recently to have a much higher ionic conductivity than the parent crystalline forms [169]. This suggestion was examined through a MD simulation on the cluster model. Since FPMD simulation on a cluster model using periodic boundary conditions is very costly, simulation was performed only at 500 K for 24 ps. Due to different chemical environments, the dynamics of the Li atoms inside the cluster (core) and on the surface were very different. The calculated diffusion coefficients D for the core and surface Li were 1.37×10^{-5} and 3.32×10^{-5} cm^2/s, respectively. As expected, the surface atoms diffused much faster than the interior atoms. Therefore, a large surface area in the nanoparticle can greatly promote Li transport ability [169, 177]. It is noteworthy that the diffusion rate of the cluster surface at 500 K was much faster than in bulk β- and γ-phases at the same temperature.

Detailed analysis of the atom trajectories showed an exchange of surface and interior Li ions. Figure 4. 16 depicts a concerted Li migration pathway within a time slice of 7 ps. Two sites on or near the surface are labelled A and B. Sites C, D and E are situated in the interior of the cluster. Initially, all sites were occupied by a Li ion (denoted as Li 4@D, 3@C, 2@B and 1@A) and the surface site E was vacant. The ions oscillated within their atomic site and then at some instant Li 4@D jumped into the empty E surface site. Concomitantly, the other Li atoms hopped consecutively, from Li 3@C →@E, Li 2@B →@C, Li 1@A →@B and a concerted diffusion process occurred. This event showed that surface Li ions (*e.g.*, Li 1) can migrate into the interior and vice versa (*e.g.*, Li 4). This type of Li transport process, however, was rare within the time scale of the simulation. Therefore, experimentally measured Li ionic conductivity was mainly due to surface diffusion.

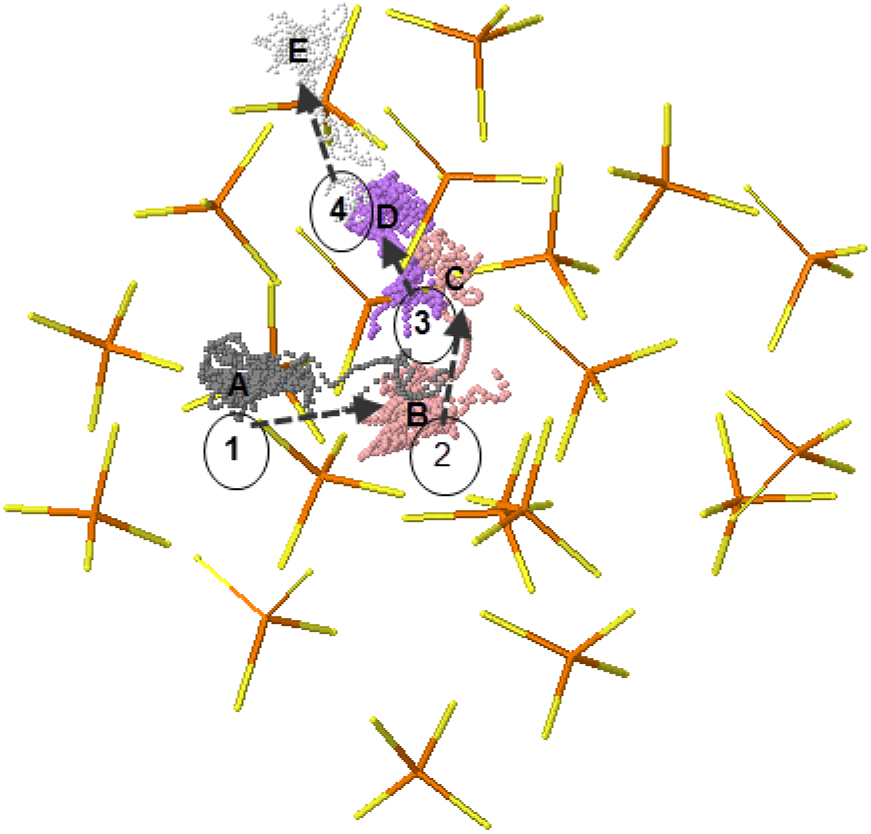

Figure 4. 16 The route for a selected concerted diffusion process in the cluster model of β-Li_3PS_4 within a simulation of 7ps, involving five crystal sites indicated by A, B, C, and D, and four Li atoms represented by 1, 2, 3, and 4 which are coloured differently. Arrows indicates the diffusion directions for the Li atoms.

4.3.4 Conclusions

First-principles calculations have been performed to investigate the diffusion processes in crystalline and nanoporous Li_3PS_4. The calculated band gap was smaller than that estimated in an electrochemical experiment. This may suggest that the stability of the electrochemical process might not originate from the pure electrolyte but may involve other possible factors. The calculated Li ionic conductivities for all three models of γ-, β-Li_3PS_4 and nanoporous systems were higher than the measured values, yet the calculated trends are consistent with previous experiments. The theoretical results showed that Li_3PS_4 crystalline polymorphs and nanoclusters are indeed good superionic conductors and suitable for solid electrolytes. The faster ionic conductivity in the β-phase was due to the presence of intrinsic Li site defects. The mobility of Li ions was much higher in the nanocluster due to available defect sites and large surface area. Although the experimental trends were reproduced, the calculated ionic conductivities were higher than the observed values. In future work, convergence of the diffusion coefficient with respect to the system size of the model system needs to be verified.

Table 4. 5 Summary of the MD simulations on three different Li_3PS_4 phases at given temperatures.Simulation length, diffusion coefficient from velocity autocorrelation function (*D*_C*vv*), calculated conductivity (σ_cal) as well as the extrapolated experimental conductivity are listed.

Model	Temperature (K)		*D*_Cvv (×10^{-5} cm^2/s)	σ_cal (S/cm)	σ_exp (S/cm)	Simulation length (ps)
γ-Li_3PS_4	500		-	-		50
γ-Li_3PS_4	800		3.449	1.48	0.02	149
β-Li_3PS_4	300		-	-		100
β-Li_3PS_4	500		0.694	0.47	0.0015	150
β-Li_3PS_4	800		4.028	1.71		110
Cluster	500	bulk	2.009	1.37	0.05	24
		surface	4.855	3.32		

CHAPTER 5

SUMMARY AND PERSPECTIVES

In Chapter 1, the need for applying first-principles calculations to understand the structural and dynamical properties of condensed matter in general and the atomic dynamics in particular was explained. In Chapter 2, the methodology used throughout the thesis work was introduced. In Chapters 3 and 4, those methods were applied to two clearly different subjects: the atomic dynamics in liquid gallium and in solid hydrogen under pressure, as well as Li transports in the cathode, anode, and solid electrolyte materials of Lithium-ion batteries (LIBs). The work presented in this thesis has helped to address key issues in these systems. However, there are still ample opportunities for future work. In this chapter, the major results and contributions are briefly summarized and perspectives for future work are presented.

5.1 Summary

One objective of the research was to characterize the structure and atomic dynamics for materials under compression by applying first-principles molecular dynamics (FPMD) methods. Two systems, liquid (*l*-) Ga and solid hydrogen, were studied in Chapter 3. Neutron and x-ray scattering experiments on *l*-Ga found a shoulder on the high-q side of the first peak of the static structure factor $S(q)$. This feature is unusual for a simple liquid and consequently has stimulated debates about its origin. Our calculations successfully reproduced the features found in the measured *S(q)*. Furthermore, there is no evidence of substantial structural changes observed within the pressure range studied. We found short-lived instantaneous Ga-Ga contacts and no characteristic Ga_2 dimer vibrational mode in the calculated VDOS spectra. In fact, because of the close proximity to the melting point, both the electronic and local structures of the liquid are similar to those of the underlying high pressure crystalline Ga-II and/or Ga-III.

The newly proposed insulating phase-IV of solid hydrogen above 250 GPa at room temperature was investigated through FPMD simulations. In agreement with the predicted static structures, phase-IV was found to consist of alternating Br_2-like molecular layers and “atomic” graphene-like layers. However, MD simulations have provided surprising insight into the dynamical structure. Phase-IV was revealed to be a partially-disordered structure with orientationally disordered H_2 in the Br_2-like layers. In comparison, the graphene-like layers were found to have an ordered lattice but there were fast H transfers between the lattice sites, leading to “pseudo”-rotations of the hexagon rings. More strikingly, even at a pressure of 300 GPa, the structures of the two distinct layers were found to exchange concomitantly and continually. However, at any instant the structure still possesses two distinct layers as in the static *Pc* structure. This fluxional structural behaviour under extreme pressure is unprecedented. Finally, a metallic, but still molecular, *Cmca*-4 phase appeared when phase-IV was compressed to 370 GPa.

LIBs are important power sources for electrical vehicles and portable electronics. However, the current performance of LIBs is not sufficient to meet increasing demands. Consequently, a search for new electrode and electrolyte materials with better performance assumes great importance. These materials must be low-cost, safe at high operating voltages, and have high energy capacity and fast rechargeable rates. An objective of the thesis research was to investigate the Li transport mechanisms at the atomic level in order to develop materials with better charge/discharge rates. In Chapter 4, the mechanism of Li transport in three sample components − cathode, anode, and electrolyte − of a LIB were studied.

$LiFePO_4$ is currently touted as the best cathode material. Our FPMD calculations have revealed two Li transport mechanisms. Apart from the accepted 1D diffusion through the Li channels of the structure, a second but less intuitive multistep Li migration through the formation of Li-Fe antisites was found. These results lend support to the 2D dimensionality model of Li diffusion based on Li conductivity measurements [113] wherein the presence of Li-Fe antisites as intrinsic defects in the sample can contribute to the Li transport process.

We studied the possibility of using type-II Si-clathrates as anode material. The calculations show that clathrates exhibit various desirable properties as an anode (*e.g.*, structural rigidity and a low and almost constant voltage upon lithiation). Most significantly, we revealed a complex sequence of events involved in the migration of Li ions through cavities of the clathrates. In the end, the calculated theoretical energy capacity was not found to be competitive for practical applications.

To understand the fast ionic conductivity behaviour in the recently reported Li_3PS_4 systems, the Li self-diffusion processes in two crystalline phases and one nanoporous form were studied using FPMD. The calculated Li ionic conductivities for all three models of γ-, β-Li_3PS_4, and nanoporous systems have the same trend as that found in available experiments. The theoretical results show that Li_3PS_4 crystalline polymorphs and nanoclusters are indeed good superionic conductors and are suitable for solid electrolytes. The relatively faster ionic conductivity in the β-phase is caused by the presence of intrinsic Li site defects. Both the defect sites and the large surface area in the nanocluster contribute to the high mobility of Li ions in the nanocluster.

5.2 Perspectives

The results obtained in Chapter 3 demonstrate the advantages of FPMD simulations for the investigation of the dynamical behaviour of condensed matters. However, DFT-based first-principles methods have several drawbacks evident when dealing with hydrogen systems. A well-known shortcoming of the current density functionals (*e.g.*, PBE) is an underestimation of the electronic band gap. One of the more serious problems with the Kohn-Sham equation is the separation of the Coulomb repulsion and the exchange interaction. This situation is known as self-energy correction, and it manifests more prominently in a one-electron system such as hydrogen. Such a deficiency may affect both the predicted relative stabilities of the different phases as well as the transition pressures [178]. In addition, the nuclear motions are neglected in the Born-Oppenheimer approximation; this is especially important in hydrogen due to the light mass of the proton. The quantum behaviour of hydrogen at the limit of very high pressure remains an open question [18]. For example, the fast H transfers in the graphene-like layers of phase-IV might be closely related to large atomic tunneling quantum effects. In future simulation research, it will be important to extend the investigation of solid hydrogen while incorporating the quantum effect. Since the proton zero-point energy (ZPE) in pressurized solid hydrogen is comparable to the binding energy and the relative energy differences between various candidate structures [178], a better estimate of ZPE is needed. Often the treatment of ZPE is accomplished by adding the vibrational entropy corrections to the ground-state DFT results; however, it is not sufficient for hydrogen systems. Both electrons and ions should be treated with rigorous quantum mechanics. That goal can be achieved by quantum Monte Carlo (QMC) calculations [179, 180] or by path-integral methods [181-184]. Within the path-integral MD (PIMD), the ionic quantum problem at a finite temperature is mapped onto a classical problem where each ion is represented by a polymer ring of fictitious particles. This PIMD technique has been used recently by Li *et al*. [185] to explore the classical and quantum ordering of protons in cold, high-pressure solid hydrogen. This approach was also applied in the study of low temperature, metallic liquid hydrogen at extremely high pressures [186]. The quantum motions of the protons were found to critical for determining melting temperatures. It was illustrated that the quantum simulations predicted the melting point of a pressurized solid hydrogen nearly 100 K lower than that obtained from the classical simulations. PIMD, however, is very computationally demanding and further development of an efficient and accurate way for numerical simulation such as reported in [7] is needed.

In a realistic battery device, the transport of Li ions during charge and discharge will be influenced by the bias voltage. The nanoscale mapping of ion diffusion under an electric field in the electrode of LIBs has been studied recently [9]. The characterization of the behaviour of electrically-driven Li-ion motions in LIB materials is critically important and relevant to the understanding of the Li ion transport mechanism during battery operations. In the present study, only the self-diffusion of Li was considered. Further studies should take into account the bias voltage. In principle, a theoretical model including an external electrical field represented by a sawtooth potential [187] in a supercell with periodic boundary conditions can be employed. In such circumstances, the dynamics of the Li ions can then be studied under the bias with existing software such as Quantum-ESPRESSO [62].

REFERENCES

1. David, L.P., S. Marie-Louise, and F.J. Bermejo, *Dynamical aspects of disorder in condensed matter.* Reports on Progress in Physics, 2003. **66**(4): p. 407.
2. Waseda, Y., *The Structure of Non-Crystalline Materials*. 1980, New York: McGraw-Hill.
3. Sherwood, J.N., *The Plastically Crystalline State*, 1979: New York: Wiley.
4. Nield, V.M. and D.A. Keen, *Diffusion Neutron Scattering from Crystalline Materials*. Vol. Chapter 9. 2001, Oxford, UK: Oxford Science Publications.
5. McMahon, J.M., et al., *The properties of hydrogen and helium under extreme conditions.* Reviews of Modern Physics, 2012. **84**(4): p. 1607-1653.
6. Schoen, D.T., C. Xie, and Y. Cui, *Electrical Switching and Phase Transformation in Silver Selenide Nanowires.* Journal of the American Chemical Society, 2007. **129**(14): p. 4116-4117.
7. Stephen, H., *Superionics: crystal structures and conduction processes.* Reports on Progress in Physics, 2004. **67**(7): p. 1233.
8. Yoshinori, K. and T. Kazuhiko, *X-ray structural studies on elemental liquids under high pressures.* Journal of Physics: Condensed Matter, 2003. **15**(36): p. 6085.
9. Kazuhiko, T., et al., *Pressure dependence of the structure of liquid group 14 elements.* Journal of Physics: Condensed Matter, 2004. **16**(14): p. S989.
10. Bellissent-Funel, M.C., et al., *Structure factor and effective two-body potential for liquid gallium.* Physical Review A, 1989. **39**(12): p. 6310-6318.
11. Narten, A.H., *Liquid Gallium: Comparison of X-Ray and Neutron-Diffraction Data.* The Journal of Chemical Physics, 1972. **56**(3): p. 1185.
12. Di Cicco, A. and A. Filipponi, *Three-body distribution function in liquids: the case of liquid gallium.* Journal of Non-Crystalline Solids, 1993. **156–158, Part 1**(0): p. 102-106.
13. Inui, M., S.i. Takeda, and T. Uechi, *Ultrasonic Velocity and Density Measurement of Liquid Bi-Ga Alloys with Miscibility Gap Region.* Journal of the Physical Society of Japan. **61**(9): p. 3203.
14. Bermejo, F.J., et al., *Microscopic dynamics of liquid gallium.* Physical Review E, 1994. **49**(4): p. 3133-3142.
15. Poloni, R., et al., *Liquid gallium in confined droplets under high-temperature and high-pressure conditions.* Physical Review B, 2005. **71**(18): p. 184111.
16. Comez, L., et al., *High-pressure and high-temperature x-ray absorption study of liquid and solid gallium.* Physical Review B, 2001. **65**(1): p. 014114.
17. Edwards, B., N.W. Ashcroft, and T. Lenosky, *Layering transitions and the structure of dense hydrogen.* EPL (Europhysics Letters), 1996. **34**(7): p. 519.
18. Goncharov, A.F., R.T. Howie, and E. Gregoryanz, *Hydrogen at extreme pressures (Review Article).* Low Temperature Physics, 2013. **39**(5): p. 402-408.
19. Hazen, R.M., et al., *Single-crystal x-ray diffraction of n-*H_2 *at high pressure.* Physical Review B, 1987. **36**(7): p. 3944-3947.
20. Mao, H.-K. and R.J. Hemley, *Ultrahigh-pressure transitions in solid hydrogen.* Reviews of Modern Physics, 1994. **66**(2): p. 671-692.

21. Akahama, Y., et al., *Evidence from x-ray diffraction of orientational ordering in phase III of solid hydrogen at pressures up to 183 GPa.* Physical Review B, 2010. **82**(6): p. 060101.
22. Hemley, R.J. and H.K. Mao, *Phase Transition in Solid Molecular Hydrogen at Ultrahigh Pressures.* Physical Review Letters, 1988. **61**(7): p. 857-860.
23. Pickard, C.J. and R.J. Needs, *Structure of phase III of solid hydrogen.* Nat Phys, 2007. **3**(7): p. 473-476.
24. Eremets, M.I. and I.A. Troyan, *Conductive dense hydrogen.* Nat Mater, 2011. **10**(12): p. 927-931.
25. Howie, R.T., et al., *Mixed Molecular and Atomic Phase of Dense Hydrogen.* Physical Review Letters, 2012. **108**(12): p. 125501.
26. Wigner, E. and H.B. Huntington, *On the Possibility of a Metallic Modification of Hydrogen.* The Journal of Chemical Physics, 1935. **3**(12): p. 764-770.
27. McMahon, J.M. and D.M. Ceperley, *High-temperature superconductivity in atomic metallic hydrogen.* Physical Review B, 2011. **84**(14): p. 144515.
28. Liu, H., et al., *Room-temperature structures of solid hydrogen at high pressures.* The Journal of Chemical Physics, 2012. **137**(7): p. 074501-7.
29. Goodenough, J.B. and Y. Kim, *Challenges for Rechargeable Li Batteries†.* Chemistry of Materials, 2009. **22**(3): p. 587-603.
30. Spontnitz, R., *Lithium-ion Batteries: The Basics.* CEP, 2013. **October**: p. 39-43.
31. Kraytsberg, A. and Y. Ein-Eli, *Higher, Stronger, Better… A Review of 5 Volt Cathode Materials for Advanced Lithium-Ion Batteries.* Advanced Energy Materials, 2012. **2**(8): p. 922-939.
32. Born, M. and R. Oppenheimer, Ann. Phys. (NY), 1927. **84**.
33. Slater, J.C., *The Theory of Complex Spectra.* Physical Review, 1929. **34**(10): p. 1293-1322.
34. Hohenberg, P. and W. Kohn, *Inhomogeneous Electron Gas.* Physical Review, 1964. **136**(3B): p. B864-B871.
35. Kohn, W. and L.J. Sham, *Self-Consistent Equations Including Exchange and Correlation Effects.* Physical Review, 1965. **140**(4A): p. A1133-A1138.
36. Ceperley, D.M. and B.J. Alder, *Ground State of the Electron Gas by a Stochastic Method.* Physical Review Letters, 1980. **45**(7): p. 566-569.
37. Becke, A.D., *Density-functional exchange-energy approximation with correct asymptotic behavior.* Physical Review A, 1988. **38**(6): p. 3098-3100.
38. Lee, C., W. Yang, and R.G. Parr, *Development of the Colle-Salvetti correlation-energy formula into a functional of the electron density.* Physical Review B, 1988. **37**(2): p. 785-789.
39. Perdew, J.P., et al., *Atoms, molecules, solids, and surfaces: Applications of the generalized gradient approximation for exchange and correlation.* Physical Review B, 1992. **46**(11): p. 6671-6687.
40. Perdew, J.P., K. Burke, and M. Ernzerhof, *Generalized Gradient Approximation Made Simple.* Physical Review Letters, 1996. **77**(18): p. 3865-3868.
41. Slater, J.C., *Quamtum Theory of Molecules and Solids*. Vol. 4. 1974, New York: McGraw-Hill.
42. Anisimov, V.I., J. Zaanen, and O.K. Andersen, *Band theory and Mott insulators: Hubbard U instead of Stoner I.* Physical Review B, 1991. **44**(3): p. 943-954.

43. Cococcioni, M. and S. de Gironcoli, *Linear response approach to the calculation of the effective interaction parameters in the LDA+U method.* Physical Review B, 2005. **71**(3): p. 035105.
44. Zhou, F., et al., *First-principles prediction of redox potentials in transition-metal compounds with LDA+U.* Physical Review B, 2004. **70**(23): p. 235121.
45. Wang, L., T. Maxisch, and G. Ceder, *Oxidation energies of transition metal oxides within the GGA+U framework.* Physical Review B, 2006. **73**(19): p. 195107.
46. Monkhorst, H.J. and J.D. Pack, *Special points for Brillouin-zone integrations.* Physical Review B, 1976. **13**(12): p. 5188-5192.
47. Pickett, W.E., *Pseudopotential methods in condensed matter applications.* Computer Physics Reports, 1989. **9**(3): p. 115-197.
48. Pickard, C.J., PhD. Thesis, 1997.
49. Payne, M.C., et al., *Iterative minimization techniques for ab initio total-energy calculations: molecular dynamics and conjugate gradients.* Reviews of Modern Physics, 1992. **64**(4): p. 1045-1097.
50. Meyer, B., *The Pseudopotential Plane Wave Approach*, in *Computational Nanoscience: Do it yourself!*, J. Grotendorst, S. Blugel, and D. Marx, Editors. 2006, NIC Series: John von Neumann Institute for Computing. p. 71.
51. Mills, G. and H. Jónsson, *Quantum and thermal effects in H_2 dissociative adsorption: Evaluation of free energy barriers in multidimensional quantum systems.* Physical Review Letters, 1994. **72**(7): p. 1124-1127.
52. Mills, G., H. Jónsson, and G.K. Schenter, *Reversible work transition state theory: application to dissociative adsorption of hydrogen.* Surface Science, 1995. **324**(2–3): p. 305-337.
53. Henkelman, G. and H. Jónsson, *Improved tangent estimate in the nudged elastic band method for finding minimum energy paths and saddle points.* The Journal of Chemical Physics, 2000. **113**(22): p. 9978-9985.
54. Henkelman, G., B.P. Uberuaga, and H. Jónsson, *A climbing image nudged elastic band method for finding saddle points and minimum energy paths.* The Journal of Chemical Physics, 2000. **113**(22): p. 9901-9904.
55. Feynman, R.P., *Forces in Molecules.* Physical Review, 1939. **56**(4): p. 340-343.
56. Swope, W.C., et al., *A computer simulation method for the calculation of equilibrium constants for the formation of physical clusters of molecules: Application to small water clusters.* The Journal of Chemical Physics, 1982. **76**(1): p. 637-649.
57. Marzari, N. and D. Vanderbilt, *Maximally localized generalized Wannier functions for composite energy bands.* Physical Review B, 1997. **56**(20): p. 12847-12865.
58. Marzari, N., et al., *Maximally localized Wannier functions: Theory and applications.* Reviews of Modern Physics, 2012. **84**(4): p. 1419-1475.
59. Thomas, M., et al., *Computing vibrational spectra from ab initio molecular dynamics.* Physical Chemistry Chemical Physics, 2013. **15**(18): p. 6608-6622.
60. Kresse, G. and J. Hafner, *Ab initio molecular dynamics for liquid metals.* Physical Review B, 1993. **47**(1): p. 558-561.
61. Kresse, G. and D. Joubert, *From ultrasoft pseudopotentials to the projector augmented-wave method.* Physical Review B, 1999. **59**(3): p. 1758-1775.

62. Paolo, G., et al., *QUANTUM ESPRESSO: a modular and open-source software project for quantum simulations of materials.* Journal of Physics: Condensed Matter, 2009. **21**(39): p. 395502.
63. CP2K, *http://www.cp2k.org/.*
64. Van de Walle, C.G. and P.E. Blöchl, *First-principles calculations of hyperfine parameters.* Physical Review B, 1993. **47**(8): p. 4244-4255.
65. Blöchl, P.E., *Projector augmented-wave method.* Physical Review B, 1994. **50**(24): p. 17953-17979.
66. Gong, X.G., et al., *α-gallium: A metallic molecular crystal.* Physical Review B, 1991. **43**(17): p. 14277-14280.
67. Hafner, J. and W. Jank, *Structural and electronic properties of the liquid polyvalent elements. III. The trivalent elements.* Physical Review B, 1990. **42**(18): p. 11530-11539.
68. Tsay, S.-F. and S. Wang, *Anomalies in the liquid structure of Ga metal.* Physical Review B, 1994. **50**(1): p. 108-112.
69. Gong, X.G., et al., *Coexistence of Monatomic and Diatomic Molecular Fluid Character in Liquid Gallium.* EPL (Europhysics Letters), 1993. **21**(4): p. 469.
70. Tsuji, K., *Structure of liquid metals under high pressure.* Journal of Non-Crystalline Solids, 1990. **117–118, Part 1**(0): p. 27-34.
71. Comez, L., et al., *EXAFS study on liquid gallium under high pressure and high temperature.* Journal of Synchrotron Radiation, 2001. **8**(2): p. 776-778.
72. Ehm, L., et al., *Studies of local and intermediate range structure in crystalline and amorphous materials at high pressure using high-energy X-rays.* Powder Diffraction, 2012. **22**(02): p. 108-112.
73. Holender, J.M., et al., *Static, dynamic, and electronic properties of liquid gallium studied by first-principles simulation.* Physical Review B, 1995. **52**(2): p. 967-975.
74. González, L.E. and D.J. González, *Structure and dynamics of bulk liquid Ga and the liquid-vapor interface: An ab initio study.* Physical Review B, 2008. **77**(6): p. 064202.
75. Hosokawa, S., et al., *Transverse Acoustic Excitations in Liquid Ga.* Physical Review Letters, 2009. **102**(10): p. 105502.
76. Tsai, K.H., T.-M. Wu, and S.-F. Tsay, *Revisiting anomalous structures in liquid Ga.* The Journal of Chemical Physics, 2010. **132**(3): p. 034502-6.
77. Tse, J.S., *Ab initio molecular dynamics with density functional theory.* Annual Review of Physical Chemistry, 2002. **53**(1): p. 249-290.
78. Furthmüller, J., J. Hafner, and G. Kresse, *Dimer reconstruction and electronic surface states on clean and hydrogenated diamond (100) surfaces.* Physical Review B, 1996. **53**(11): p. 7334-7351.
79. Wang, Y. and J.P. Perdew, *Correlation hole of the spin-polarized electron gas, with exact small-wave-vector and high-density scaling.* Physical Review B, 1991. **44**(24): p. 13298-13307.
80. Nose, S., *A unified formulation of the constant temperature molecular dynamics methods.* The Journal of Chemical Physics, 1984. **81**(1): p. 511-519.
81. Hoover, W.G., *Canonical dynamics: Equilibrium phase-space distributions.* Physical Review A, 1985. **31**(3): p. 1695-1697.
82. Donohue, J., *The Structure of the Elements*. 1974, Wiley: New York.
83. Degtyareva, O., et al., *Structural Complexity in Gallium under High Pressure: Relation to Alkali Elements.* Physical Review Letters, 2004. **93**(20): p. 205502.

84. Bosio, L., *Crystal structures of Ga(II) and Ga(III).* The Journal of Chemical Physics, 1978. **68**(3): p. 1221-1223.
85. Bove, L.E., et al., *Vibrational dynamics of liquid gallium at 320 and 970K.* Physical Review B, 2005. **71**(1): p. 014207.
86. Johnson, B.G., P.M.W. Gill, and J.A. Pople, *The performance of a family of density functional methods.* The Journal of Chemical Physics, 1993. **98**(7): p. 5612-5626.
87. Yang, J., J.S. Tse, and T. Iitaka, *First-principles studies of liquid lithium under pressure.* J Phys Condens Matter, 2010. **22**(9): p. 095503.
88. Elliott, S.R., *Origin of the first sharp diffraction peak in the structure factor of covalent glasses.* Physical Review Letters, 1991. **67**(6): p. 711-714.
89. Spagnolatti, I. and M. Bernasconi, *Ab initio phonon dispersion relations of α-Ga.* The European Physical Journal B - Condensed Matter and Complex Systems, 2003. **36**(1): p. 87-90.
90. Ankudinov, A.L., et al., *Real-space multiple-scattering calculation and interpretation of x-ray-absorption near-edge structure.* Physical Review B, 1998. **58**(12): p. 7565-7576.
91. Baskes, M.I., S.P. Chen, and F.J. Cherne, *Atomistic model of gallium.* Physical Review B, 2002. **66**(10): p. 104107.
92. Łużny, W., et al., *Inelastic neutron scattering on solid and liquid gallium.* physica status solidi (a), 1989. **116**(1): p. K25-K28.
93. Bosio, L., et al., *Phonons in metastable beta gallium: neutron scattering measurements.* Journal of Physics F: Metal Physics, 1981. **11**(11): p. 2261.
94. Ascarelli, P., *Atomic Radial Distributions and Ion-Ion Potential in Liquid Gallium.* Physical Review, 1966. **143**(1): p. 36-47.
95. Nield, V.M., R.L. McGreevy, and M.G. Tucker, *Changes in the short-range order of gallium on melting and supercooling.* Journal of Physics: Condensed Matter, 1998. **10**(15): p. 3293.
96. Babaev, E., A. Sudbo, and N.W. Ashcroft, *A superconductor to superfluid phase transition in liquid metallic hydrogen.* Nature, 2004. **431**(7009): p. 666-668.
97. Lorenzana, H.E., I.F. Silvera, and K.A. Goettel, *Orientational phase transitions in hydrogen at megabar pressures.* Physical Review Letters, 1990. **64**(16): p. 1939-1942.
98. Zha, C.-S., Z. Liu, and R.J. Hemley, *Synchrotron Infrared Measurements of Dense Hydrogen to 360 GPa.* Physical Review Letters, 2012. **108**(14): p. 146402.
99. Mazin, I.I., et al., *Quantum and Classical Orientational Ordering in Solid Hydrogen.* Physical Review Letters, 1997. **78**(6): p. 1066-1069.
100. Pickard, C.J., M. Martinez-Canales, and R.J. Needs, *Density functional theory study of phase IV of solid hydrogen.* Physical Review B, 2012. **85**(21): p. 214114.
101. Johnson, K.A. and N.W. Ashcroft, *Structure and bandgap closure in dense hydrogen.* Nature, 2000. **403**(6770): p. 632-635.
102. Pickard, C.J., M. Martinez-Canales, and R.J. Needs, *Erratum: Density functional theory study of phase IV of solid hydrogen [Phys. Rev. B 85, 214114 (2012)].* Physical Review B, 2012. **86**(5): p. 059902.
103. Zijun, Y., *General thermal wavelength and its applications.* European Journal of Physics, 2000. **21**(6): p. 625.
104. Kitamura, H., et al., *Quantum distribution of protons in solid molecular hydrogen at megabar pressures.* Nature, 2000. **404**(6775): p. 259-262.

105. Liu, H. and Y. Ma, *Proton or Deuteron Transfer in Phase IV of Solid Hydrogen and Deuterium.* Physical Review Letters, 2013. **110**(2): p. 025903.
106. Marqués, M., et al., *Crystal Structures of Dense Lithium: A Metal-Semiconductor-Metal Transition.* Physical Review Letters, 2011. **106**(9): p. 095502.
107. Goncharov, A.F., et al., *Bonding, structures, and band gap closure of hydrogen at high pressures.* Physical Review B, 2013. **87**(2): p. 024101.
108. Hanfland, M., R.J. Hemley, and H.-K. Mao, *Novel infrared vibron absorption in solid hydrogen at megabar pressures.* Physical Review Letters, 1993. **70**(24): p. 3760-3763.
109. Hanfland, M., et al., *Synchrotron infrared spectroscopy at megabar pressures: Vibrational dynamics of hydrogen to 180 GPa.* Physical Review Letters, 1992. **69**(7): p. 1129-1132.
110. Morgan, D., A. Van der Ven, and G. Ceder, *Li Conductivity in Li_xMPO_4 $(M = Mn, Fe, Co, Ni)$ Olivine Materials.* Electrochemical and Solid-State Letters, 2004. **7**(2): p. A30-A32.
111. Ouyang, C., et al., *First-principles study of Li ion diffusion in $LiFePO_4$.* Physical Review B, 2004. **69**(10): p. 104303.
112. Islam, M.S., et al., *Atomic-Scale Investigation of Defects, Dopants, and Lithium Transport in the $LiFePO_4$ Olivine-Type Battery Material.* Chemistry of Materials, 2005. **17**(20): p. 5085-5092.
113. Amin, R. and J. Maier, *Effect of annealing on transport properties of LiFePO4: Towards a defect chemical model.* Solid State Ionics, 2008. **178**(35–36): p. 1831-1836.
114. Amin, R., et al., *Ionic and electronic transport in single crystalline LiFePO4 grown by optical floating zone technique.* Solid State Ionics, 2008. **179**(27–32): p. 1683-1687.
115. Padhi, A.K., K.S. Nanjundaswamy, and J.B. Goodenough, *Phospho‐olivines as Positive‐Electrode Materials for Rechargeable Lithium Batteries.* Journal of The Electrochemical Society, 1997. **144**(4): p. 1188-1194.
116. Huang, H., S.-C. Yin, and L.F. Nazar, *Approaching Theoretical Capacity of LiFePO4 at Room Temperature at High Rates.* Electrochemical and Solid-State Letters, 2001. **4**(10): p. A170-A172.
117. Chung, S.-Y., J.T. Bloking, and Y.-M. Chiang, *Electronically conductive phospho-olivines as lithium storage electrodes.* Nat Mater, 2002. **1**(2): p. 123-128.
118. Zhou, F., et al., *The electronic structure and band gap of $LiFePO_4$ and $LiMnPO_4$.* Solid State Communications, 2004. **132**(3–4): p. 181-186.
119. Zaghib, K., et al., *Electronic, Optical, and Magnetic Properties of $LiFePO_4$: Small Magnetic Polaron Effects.* Chemistry of Materials, 2007. **19**(15): p. 3740-3747.
120. Yamada, A., S.C. Chung, and K. Hinokuma *Optimized $LiFePO_4$ for Lithium Battery Cathodes.* Journal of The Electrochemical Society, 2001. **148**(3): p. A224-A229.
121. Herle, P.S., et al., *Nano-network electronic conduction in iron and nickel olivine phosphates.* Nat Mater, 2004. **3**(3): p. 147-152.
122. Kang, B. and G. Ceder, *Battery materials for ultrafast charging and discharging.* Nature, 2009. **458**(7235): p. 190-193.
123. Zaghib, K., et al., *Unsupported claims of ultrafast charging of $LiFePO_4$ Li-ion batteries.* Journal of Power Sources, 2009. **194**(2): p. 1021-1023.
124. Li, J., et al., *Lithium ion conductivity in single crystal $LiFePO_4$.* Solid State Ionics, 2008. **179**(35–36): p. 2016-2019.

125. Nishimura, S.-I., et al., *Experimental visualization of lithium diffusion in Li_xFePO_4.* Nat Mater, 2008. **7**(9): p. 707-711.
126. Maier, J. and R. Amin, *Defect Chemistry of $LiFePO_4$.* Journal of The Electrochemical Society, 2008. **155**(4): p. A339-A344.
127. Chen, J., et al., *The hydrothermal synthesis and characterization of olivines and related compounds for electrochemical applications.* Solid State Ionics, 2008. **178**(31–32): p. 1676-1693.
128. Adams, S., *Lithium ion pathways in $LiFePO_4$ and related olivines.* Journal of Solid State Electrochemistry, 2010. **14**(10): p. 1787-1792.
129. Fisher, C.A.J., V.M. Hart Prieto, and M.S. Islam, *Lithium Battery Materials $LiMPO_4$ (M = Mn, Fe, Co, and Ni): Insights into Defect Association, Transport Mechanisms, and Doping Behavior.* Chemistry of Materials, 2008. **20**(18): p. 5907-5915.
130. Jónsson, H., G. Mills, and K.W. Jacobsen, *Nudged elastic band method for finding minimum energy paths of transitions*, in *Classical and Quantum Dynamics in Condensed Phase Simulations*. p. 385-404.
131. Blöchl, P.E., O. Jepsen, and O.K. Andersen, *Improved tetrahedron method for Brillouin-zone integrations.* Physical Review B, 1994. **49**(23): p. 16223-16233.
132. Perdew, J.P., et al., *Restoring the Density-Gradient Expansion for Exchange in Solids and Surfaces.* Physical Review Letters, 2008. **100**(13): p. 136406.
133. Dudarev, S.L., et al., *Electron-energy-loss spectra and the structural stability of nickel oxide:An LSDA+U study.* Physical Review B, 1998. **57**(3): p. 1505-1509.
134. Kresse, G. and J. Furthmüller, *Efficient iterative schemes for ab initio total-energy calculations using a plane-wave basis set.* Physical Review B, 1996. **54**(16): p. 11169-11186.
135. Rousse, G., et al., *Magnetic Structures of the Triphylite $LiFePO_4$ and of Its Delithiated Form $FePO_4$.* Chemistry of Materials, 2003. **15**(21): p. 4082-4090.
136. Malik, R., et al., *Particle Size Dependence of the Ionic Diffusivity.* Nano Letters, 2010. **10**(10): p. 4123-4127.
137. Hoang, K. and M. Johannes, *Tailoring Native Defects in $LiFePO_4$: Insights from First-Principles Calculations.* Chemistry of Materials, 2011. **23**(11): p. 3003-3013.
138. Chung, S.-Y., et al., *Atomic-Scale Visualization of Antisite Defects in $LiFePO_4$.* Physical Review Letters, 2008. **100**(12): p. 125502.
139. Hamelet, S., et al., *The effects of moderate thermal treatments under air on $LiFePO_4$-based nano powders.* Journal of Materials Chemistry, 2009. **19**(23): p. 3979-3991.
140. Chan, C.K., et al., *High-performance lithium battery anodes using silicon nanowires.* Nat Nano, 2008. **3**(1): p. 31-35.
141. Larcher, D., et al., *Recent findings and prospects in the field of pure metals as negative electrodes for Li-ion batteries.* Journal of Materials Chemistry, 2007. **17**(36): p. 3759-3772.
142. Park, M.-H., et al., *Silicon Nanotube Battery Anodes.* Nano Letters, 2009. **9**(11): p. 3844-3847.
143. Kawaji, H., et al., *Superconductivity in the Silicon Clathrate Compound $(Na,Ba)_xSi_{46}$.* Physical Review Letters, 1995. **74**(8): p. 1427-1429.
144. Yamanaka, S., et al., *High-Pressure Synthesis of a New Silicon Clathrate Superconductor, Ba_8Si_{46}.* Inorganic Chemistry, 1999. **39**(1): p. 56-58.

145. Nolas, G.S., et al., *Semiconducting Ge clathrates: Promising candidates for thermoelectric applications.* Applied Physics Letters, 1998. **73**(2): p. 178-180.
146. San-Miguel, A., et al., *High Pressure Behavior of Silicon Clathrates: A New Class of Low Compressibility Materials.* Physical Review Letters, 1999. **83**(25): p. 5290-5293.
147. Chan, K.S., Chan, C. K., and Liang, W., *Silicon Clathrate Anodes for Lithium-Ion Batteries*, in *US Patent* 2012.
148. Davidson, D.W., et al., *The ability of small molecules to form clathrate hydrates of structure II.* Nature, 1984. **311**(5982): p. 142-143.
149. Horie, H.-O., et al., *Controlled thermal decomposition of NaSi to derive silicon clathrate compounds.* Journal of Solid State Chemistry, 2009. **182**(1): p. 129-135.
150. Langer, T., et al., *Electrochemical Lithiation of Silicon Clathrate-II.* Journal of The Electrochemical Society, 2012. **159**(8): p. A1318-A1322.
151. Kasper, J.S., et al., *Clathrate Structure of Silicon* Na_8Si_{46} *and* Na_xSi_{136} $(x < 11)$. Science, 1965. **150**(3704): p. 1713-1714.
152. Ker, A., et al., *Structure and Phase Stability of Binary Zintl-Phase Compounds: Lithium–Group 13 Intermetallics and Metal-Doped Group 14 Clathrate Compounds.* Chemistry – A European Journal, 2002. **8**(12): p. 2787-2798.
153. Rachi, T., et al., *Preparation and electronic states of* $Na_{16}Ba_8Si_{136}$ *clathrate.* Chemical Physics Letters, 2005. **409**(1–3): p. 48-51.
154. Ohzuku, T., Y. Iwakoshi, and K. Sawai, *Formation of Lithium‐Graphite Intercalation Compounds in Nonaqueous Electrolytes and Their Application as a Negative Electrode for a Lithium Ion (Shuttlecock) Cell.* Journal of The Electrochemical Society, 1993. **140**(9): p. 2490-2498.
155. Kasavajjula, U., C. Wang, and A.J. Appleby, *Nano- and bulk-silicon-based insertion anodes for lithium-ion secondary cells.* Journal of Power Sources, 2007. **163**(2): p. 1003-1039.
156. Gryko, J., et al., *Low-density framework form of crystalline silicon with a wide optical band gap.* Physical Review B, 2000. **62**(12): p. R7707-R7710.
157. Adams, G.B., et al., *Wide-band-gap Si in open fourfold-coordinated clathrate structures.* Physical Review B, 1994. **49**(12): p. 8048-8053.
158. Blase, X., *Quasiparticle band structure and screening in silicon and carbon clathrates.* Physical Review B, 2003. **67**(3): p. 035211.
159. Courtney, I.A., et al., *Ab initio calculation of the lithium-tin voltage profile.* Physical Review B, 1998. **58**(23): p. 15583-15588.
160. Ceder, G., Hautier, G., Jain, and A., Ong, S.P., *Recharging lithium battery research with first-principles methods.* MRS Bulletin, 2011. **36**(03): p. 185-191.
161. Ma, C., X. Shao, and D. Cao, *Nitrogen-doped graphene nanosheets as anode materials for lithium ion batteries: a first-principles study.* Journal of Materials Chemistry, 2012. **22**(18): p. 8911-8915.
162. Beekman, M. and G.S. Nolas, *Inorganic clathrate-II materials of group 14: synthetic routes and physical properties.* Journal of Materials Chemistry, 2008. **18**(8): p. 842-851.
163. Zhang, Q., et al., *Lithium Insertion In Silicon Nanowires: An ab Initio Study.* Nano Letters, 2010. **10**(9): p. 3243-3249.
164. Zhao, K., et al., *Lithium-Assisted Plastic Deformation of Silicon Electrodes in Lithium-Ion Batteries: A First-Principles Theoretical Study.* Nano Letters, 2011. **11**(7): p. 2962-2967.

165. Xia, H., et al., *Phase Transitions and High-Voltage Electrochemical Behavior of $LiCoO_2$ Thin Films Grown by Pulsed Laser Deposition.* Journal of The Electrochemical Society, 2007. **154**(4): p. A337-A342.
166. Simon, P., et al., *Synthesis and Electron Holography Studies of Single Crystalline Nanostructures of Clathrate-II Phases K_xGe_{136} and Na_xSi_{136}.* Journal of the American Chemical Society, 2011. **133**(19): p. 7596-7601.
167. Yamanaka, S. and S. Maekawa, *Structural evolution of the binary system Ba-Si under high-pressure and high-temperature conditions.* Z. Naturforsch., B: Chemical Sciences, 2006. **61**(12): p. 1493-1499.
168. Kamaya, N., et al., *A lithium superionic conductor.* Nat Mater, 2011. **10**(9): p. 682-686.
169. Liu, Z., et al., *Anomalous High Ionic Conductivity of Nanoporous β-Li_3PS_4.* Journal of the American Chemical Society, 2013. **135**(3): p. 975-978.
170. Tachez, M., et al., *Ionic conductivity of and phase transition in lithium thiophosphate Li_3PS_4.* Solid State Ionics, 1984. **14**(3): p. 181-185.
171. Homma, K., et al., *Crystal structure and phase transitions of the lithium ionic conductor Li_3PS_4.* Solid State Ionics, 2011. **182**(1): p. 53-58.
172. Lepley, N.D., N.A.W. Holzwarth, and Y.A. Du, *Structures, Li^+ mobilities, and interfacial properties of solid electrolytes Li_3PS_4 and Li_3PO_4 from first principles.* Physical Review B, 2013. **88**(10): p. 104103.
173. Yang, J. and J.S. Tse, *Li Ion Diffusion Mechanisms in $LiFePO_4$: An ab Initio Molecular Dynamics Study.* The Journal of Physical Chemistry A, 2011. **115**(45): p. 13045-13049.
174. Ong, S.P., et al., *Electrochemical Windows of Room-Temperature Ionic Liquids from Molecular Dynamics and Density Functional Theory Calculations.* Chemistry of Materials, 2011. **23**(11): p. 2979-2986.
175. Mo, Y., S.P. Ong, and G. Ceder, *First Principles Study of the $Li_{10}GeP_2S_{12}$ Lithium Super Ionic Conductor Material.* Chemistry of Materials, 2011. **24**(1): p. 15-17.
176. Kumar, P.P. and S. Yashonath, *Ionic conduction in the solid state.* Journal of Chemical Sciences, 2006. **118**(1): p. 135-154.
177. Ge, M., et al., *Scalable preparation of porous silicon nanoparticles and their application for lithium-ion battery anodes.* Nano Research, 2013. **6**(3): p. 174-181.
178. Azadi, S. and W.M.C. Foulkes, *Fate of density functional theory in the study of high-pressure solid hydrogen.* Physical Review B, 2013. **88**(1): p. 014115.
179. Ceperley, D.M. and B.J. Alder, *Ground state of solid hydrogen at high pressures.* Physical Review B, 1987. **36**(4): p. 2092-2106.
180. Natoli, V., R.M. Martin, and D.M. Ceperley, *Crystal structure of atomic hydrogen.* Physical Review Letters, 1993. **70**(13): p. 1952-1955.
181. Tuckerman, M.E., et al., *Efficient molecular dynamics and hybrid Monte Carlo algorithms for path integrals.* The Journal of Chemical Physics, 1993. **99**(4): p. 2796-2808.
182. Marx, D. and M. Parrinello, *Ab initio path integral molecular dynamics: Basic ideas.* The Journal of Chemical Physics, 1996. **104**(11): p. 4077-4082.
183. Ceriotti, M., et al., *Efficient stochastic thermostatting of path integral molecular dynamics.* The Journal of Chemical Physics, 2010. **133**(12): p. 124104.
184. Ceriotti, M., D.E. Manolopoulos, and M. Parrinello, *Accelerating the convergence of path integral dynamics with a generalized Langevin equation.* The Journal of Chemical Physics, 2011. **134**(8): p. 084104.

185. Xin-Zheng, L., et al., *Classical and quantum ordering of protons in cold solid hydrogen under megabar pressures.* Journal of Physics: Condensed Matter, 2013. **25**(8): p. 085402.
186. Chen, J., et al., *Quantum simulation of low-temperature metallic liquid hydrogen.* Nat Commun, 2013. **4**: p. 2064.
187. Kirtman, B., et al., *Polarization of one-dimensional periodic systems in a static electric field: Sawtooth potential treatment revisited.* The Journal of Chemical Physics, 2009. **131**(4): p. 044109.